THIN FILM FUEL CELL/BATTERY POWER GENERATING SYSTEM

C-1197-13

Annual Report
Covering the Period
April 1, 1978 to March 31, 1979

W. Feduska, Project Manager
A. O. Isenberg, Technical Coordinator
J. E. Bauerle, Y. Ichikawa, R. J. Ruka
S. A. Zeitman, G. E. Zymboly, Contributors

Prepared for the United States Department of Energy
Under Continuation Contract No. ~~DE-AC-0379ET11305~~
(Formerly Contract EY-76-C-03-1197) AC02-76ET11305

by

Research and Development Center
WESTINGHOUSE ELECTRIC CORPORATION
Pittsburgh, Pennsylvania 15235

April 30, 1979

Westinghouse R&D Center
1310 Beulah Road
Pittsburgh, Pennsylvania 15235

DISCLAIMER

THIN FILM FUEL CELL/BATTERY POWER GENERATING SYSTEM

C-1197-13

Annual Report
Covering the Period
April 1, 1978 to March 31, 1979

W. Feduska, Project Manager
A. O. Isenberg, Technical Coordinator
J. E. Bauerle, Y. Ichikawa, R. J. Ruka
S. A. Zeitman, G. E. Zymboly, Contributors

Prepared for the United States Department of Energy
Under Continuation Contract No. DE-AC-0379ET11305
(Formerly Contract EY-76-C-03-1197)

by

Research and Development Center
WESTINGHOUSE ELECTRIC CORPORATION
Pittsburgh, Pennsylvania 15235

April 30, 1979

Westinghouse R&D Center
1310 Beulah Road
Pittsburgh, Pennsylvania 15235

FOREWORD

For the first year of the present two year continuation program (contract DE-AC-0379ET11305) the Department of Energy Program Manager was Mr. R. F. Dudley, Jr. His assistance and guidance in both program planning and in direct contract-related matters is gratefully acknowledged.

PREFACE

For those who desire to learn about the objectives and results obtained during the first two-year contract period of this program, a Past Program Summary is given in Appendix A.

For purposes of providing background information to those readers who may be unfamiliar with the operation, design concept and some possible applications of the high-temperature, solid oxide electrolyte (HTSOE) fuel cell, Appendix B has been included in this report.

In Appendix C an analysis has been made of the tolerance level to sulfur or sulfur species of the HTSOE fuel cell.

TABLE OF CONTENTS

TABLE OF CONTENTS (Cont'd)

TABLE OF CONTENTS (Cont'd)

TABLE OF CONTENTS (Cont'd)

LIST OF ILLUSTRATIONS

LIST OF ILLUSTRATIONS (Cont'd)

LIST OF ILLUSTRATIONS (Cont'd)

LIST OF ILLUSTRATIONS (Cont'd)

List of Illustrations (Cont'd)

List of Illustrations (Cont'd)

LIST OF TABLES

ABSTRACT

Work on the modified lanthanum chromite interconnection (IC) proceeded in a number of areas. Toward determining the stability of the IC, oxygen ion transport mechanisms were evaluated, as well as IC stability under low oxygen partial pressures (10^{-6}t 10^{-18}atm.). To produce long, continuous, 40 μm thick IC films on 0.3 m long porous support tubes, improvements were made in both the EVD apparatus and process.

Porous support tubes of calcia-stabilized zirconia were produced, up to 0.3 m long, for fuel cell stack fabrication. Here, also, improved equipment and processes were used to enhance the final tube quality.

Work on the air electrode current collector covered several areas. The high-temperature resistivity of doped indium oxide was studied at various doping levels, as a function of oxygen partial pressure. Also, other possible current collector formulations were investigated. Doped lanthanum manganites appear promising, as a possible replacement for doped indium oxide, based on initial fuel cell stack performance data.

By incorporating materials and process improvements, as well as improved porous support tubes, in the fabrication of 20 cell stacks, stack quality and performance at 400 mA/cm^2 and 1000°C have steadily improved. However, a 20 cell stack, delivering 10W of power, must yet be demonstrated.

Measurement techniques have been refined on the fuel cell and its components. Realistic combination specimens, as fuel electrode-interconnection layers on a porous support tube, have been used to determine interconnection apparent resistivity at 1000°C. From polarization tests on fabricated fuel cell stacks, major electrical resistance contributors to the total cell resistance are the air electrode and the interconnection, with the latter being the largest contributor.

1.0 GENERAL CONCLUSIONS

1. The electrochemical vapor deposition (EVD) process has been improved, with regard to both equipment and process procedures, and has produced uniform 40 μm layers of modified lanthanum chromite interconnection and yttria-stabilized zirconia solid electrolyte on long, 20 cell fuel cell stacks.
2. Considerable effort has been directed toward understanding the air electrode-interconnection interface behavior, through studies of $O^{=}$ transport and loss in the interconnection, as a function of temperature and oxygen partial pressure, with no adverse effects found with respect to property or compositional changes, at oxygen partial pressures from 10^{-7} to 10^{-17} atm at 1000°C. The interconnection film is stable, dense and of suitable electrical conductivity.
3. A search for a more stable air electrode material has been undertaken. Doped-lanthanum manganites appear promising.
4. The interface and air accessibility to the air electrode-interconnection interface has been improved by modified processing procedures.
5. In-house porous, calcia-stabilized zirconia support tubes, about 0.3 m long, are being fabricated in improved equipment and with improved processes toward desired dimensional and physical properties.
6. Large stacks are being fabricated. However, performance is only at ~82% of voltage target, but stable at 1000°C, based on a 14 cell stack that was tested for ~100 hours.

7. Procedures have been developed to obtain component and interfacial electrical resistance measurements. Data correlate well with polarization data obtained by the current interruption technique, in a tested 5 cell stack.
8. The ten-watt stack milestone has not been attained, but should be reached in the next quarter of the program, now that processes and component materials have been modified, toward attaining that objective.

2.0 PROGRAM SUMMARY

Highlights of progress during the past year of the present 2-year continuation program are described for the various tasks and subtasks, as outlined in the Contract Management Plan of the program.

TASK 1. DEVELOPMENT AND REFINEMENT OF FABRICATION PROCESSES

The goal of this task is to develop reliable techniques of component fabrication that will lead to reproducible stack performance.

Subtask 1A. Interconnection* Fabrication by Electrochemical Vapor Deposition

Work in this area was aimed at producing uniform layers of modified lanthanum chromite onto 20 cell stacks. This entailed a modification of the equipment and halide delivery systems, so that such layers could be uniformly deposited onto the 0.3 m long tube section, which had been precoated with the nickel-cermet fuel electrode bands and in some cases, the solid electrolyte bands.

Successful techniques have been developed for depositing modified lanthanum chromite layers of ~40 μm thickness over the length of a 20 cell stack. The details of this process are presented in Section 5.1.1.3 of the report. The nature and occurrence of magnesium in the IC material was also examined and is reported in Section 5.1.1.1. Work continued on the RF sputtering apparatus and procedures for coating $La_{.95}Mg_{.05}Cr_{.75}Al_{.25}O_3$ bands onto fuel cell tube sections, to obtain precise IC compositions for performance evaluation (Section 5.1.1.2).

Subtask 1B. Fuel Electrode - Stack Process

A new, slurry dipping procedure was devised and proven successful for coating porous support tubes with porous, nickel-cermet fuel electrode bands of ~40 μm thickness. This fast coating method, described

*For convenience the interconnection is abbreviated as IC throughout the report.

in Section 5.1.2, protects the inside of the tube from being coated and facilitates handling of the longer 0.3 m tube sections. The fuel electrode composition was also extended to a 60 v/o Ni - 40 v/o ZrO_2 composition, in addition to the prior 40 v/o Ni - 60 v/o ZrO_2 mixture, to enhance its electrical conductivity.

Subtask 1C. Air Electrode - Stack Process

Considerable effort was expended in this area of the fuel cell stack fabrication, both toward understanding and eliminating the air electrode flaking problem, observed in testing the 3 cell stack of the prior 2-year program. A new reactor with a 40 cm long deposition zone was designed and constructed, to obtain coatings of tin-doped indium oxide current collector on 20 cell fuel cell stacks. To obtain air permeable current collector layers, seeding and microporous, oxidized-metallic coatings and undercoatings have been explored. The latter techniques shows promise as a means of obtaining stable mechanical and electrical contacts between the interconnection and the air electrode (See Section 5.1.3).

In other air electrode work, different current collector compositions have been developed. In particular, lanthanum manganite appears promising as a replacement for tin-doped indium oxide, which is unstable and can flake or vaporize at 1000°C under stack operating conditions. Section 5.2.4.5 describes the application of the lanthanum manganite.

Subtask 1D. Porous Support Tube Refinement

In-house extrusion and firing of long, 0.3 m tube lengths of calcia-stabilized zirconia continues. To prepare strong, uniform tubes in the lengths required, the starting batch material for extrusion has been refined and the furnace has been modified to enhance uniformity of temperature during sintering. Recently prepared tubes are showing improved strength and quality (porosity and surface texture) toward that needed in processing fuel cell stacks (Section 5.1.5 details the porous tube process and relates tube property data).

Subtask 1E. Cell Stack

Cell stacks that were fabricated were the result of improvements in equipment and processing (particularly IC EVD fabrication) and in porous support tube preparation. These variations are detailed in Section 5.1.6. Of the stacks cited in that section, stack #4 consisted of 14 cells, having a strontium-doped lanthanum manganite air electrode current collector. Stack performance data are related in Task 3.

Electrolyte EVD Process

Although not a specific subtask, the electrolyte EVD process was scaled-up to permit deposition of 40 μm thickness layers of yttria-stabilized zirconia onto the 0.3 m long tube sections. The technique was modified to enable a duplex layer to be produced -- a dense electrolyte layer was first deposited, followed by application of a porous zirconia layer in a short time (1/2h) run. The procedure (Section 5.1.4) permits better control and quality of the subsequently deposited air electrode current collector (tin-doped indium oxide).

TASK 2. LIFE TESTING OF CELL COMPONENTS AND STACK

The purpose of this task is to evaluate the nature and extent of long-term stack deterioration, due to mechanical and/or chemical component interaction. The goal is life prediction of cell stacks, using the state-of-the-art component materials and fabrication techniques.

To enable the life testing of cell components, unit cells and cell stacks, a five station, fuel cell life test facility was designed, built and made operational. The facility has a 150 channel data logger for continuous monitoring and data collection and can measure, by the current interruption technique, ohmic and slow polarization losses in cells. The detailed nature of this facility is described in Section 5.2.1.

Subtask 2A. Interconnection Testing in a Dual Atmosphere

A resistance measuring technique has been developed that defines the electrical resistance of the interconnection, under a dual atmosphere condition. This technique is the multi-surface technique and is described in detail in Section 5.2.2.

Subtask 2B. Fuel Electrode-Interconnection Interaction

A fuel electrode combination specimen was prepared on a porous support tube and tested at 600 to 1000°C in a $H_2/3\% H_2O$ environment. Interconnection apparent resistivity at 1000°C was about 30Ω cm -- about 10 x higher than expected on the bulk material but, possibly, mostly reflecting the interfacial resistance between the IC and the fuel electrode (Section 5.2.3.1).

Subtask 2C. Air Electrode-Interconnection Interaction

The lanthanum chromite interconnection exhibits some solid state permeability to oxygen (via vacant oxygen sites in the crystal lattice). At the low oxygen partial pressures that exist at their interface, the interconnection can scavenge oxygen from the air electrode (indium oxide and/or tin oxide). Reducing these oxides to less stable species can cause a breakdown at the interface and even spalling-off of the air electrode as flakes. To circumvent this problem, considerable effort was expended in various areas:

1) enhancing the availability of $O^=$ to the air electrode-interconnection interface
2) understanding the behavior of lanthanum chromite in either air or hydrogen/water atmospheres at 1000°C
3) determining the electrical resistivity properties of tin-doped indium oxide as a function of oxygen partial pressure
4) exploring alternate, more stable air electrode materials
5) improving the interface bond between the air electrode and the interconnection
6) improving the mechanical porosity of the air electrode.

These investigations determined the following.

1) Increased tin-doping (0.04 to 0.16 w/o) increases, non-linearly, the oxygen loss in tin-doped indium oxide at 1000°C.
2) Alternate substitution, with tantalum or zirconium in place of tin, also resulted in oxygen loss from the resultant doped indium oxide at 1000°C.
3) Material losses in tin-doped indium oxide at 1000°C were irreversible below 10^{-14} atm and oxygen loss was reversible in atmospheres containing 1%, or more, oxygen.
4) At 1000°C oxygen loss in modified lanthanum chromite, (pressed and treated powder samples) occurs from its surface at about 10^{-6} atm, or greater. Loss from the interior of the crystal occurs at pressures below 10^{-6} atm of oxygen.
5) Oxygen loss in modified lanthanum chromite EVD films is at sufficiently-low levels to be acceptable at the low O_2 partial pressures anticipated at the air electrode-interconnection interface and should not be a problem, providing that sufficient air access to the interconnection can be maintained.
6) The oxygen diffusion coefficient in a bulk sample of modified lanthanum chromite was determined at $\sim 2 \times 10^{-13}$ cm^2/sec for times up to 65 h at 1000°C. Oxygen diffusion in sputtered 3 μm films of modified lanthanum chromite is greater, based on O_2 equilibration time with air at 1000°C, probably due to grain boundary diffusion in this fine grain size film.
7) A pressed and sintered $In_{1.96}Sn_{0.04}O_{3\pm x}$ sample was measured for elevated temperature electrical resistivity, as a function of oxygen partial pressure, to simulate its behavior at the interface with the interconnection material.

Resistivity decreased with decreasing oxygen partial pressure, from ~10 milli Ω-cm at atmospheric, down to about 3 milli Ω-cm at 10^{-10} atm oxygen partial pressure at 1000°C. The nature of the decomposition reaction suggested by these resistance changes is not yet known.

8) Significant progress has been made in developing alternate air electrode current collector materials. $La_{0.9}Sr_{0.1}MnO_3$ and $Ca_{0.5}La_{0.5}MnO_3$ are promising candidates, having excellent thermal expansion matching with the interconnection and electrolyte as well as adequate electrical conductivity.

Subtask 2D. Single Cell Life Test and Subtask 2E. Small Stack Life Test

A number of stack fabrications have been tried, using in-house porous support tubing, scaled-up fabrication techniques (as required to fabricate 20 cell stacks onto 0.3 m long tubes) and modified air electrode materials. Some initial performance data has been obtained on small stacks. One stack of 14 series-connected cells (stack #4) has demonstrated stable, but low, output at elevated temperature over a period of ~100 h at 400 mA/cm^2, 1000°C, H_2/3% H_2O fuel inlet, at ~82% of the desired cell voltage goal of 0.66 v. The high resistance of the air electrode current collector in this stack caused most of this voltage loss.

TASK 3. STACK PERFORMANCE EVALUATION

In this task stacks are to be tested with respect to power output at varying cell efficiencies and with varying fuel and air conditions. Nature and causes of cell polarization are also to be determined. Also the effect of fuel and air conditions on performance are to be determined. Work on this task is awaiting fabrication of suitable 10 W stacks.

5.3.3 Subtask A. Power Output

Power output evaluation is awaiting the construction of fuel cell stacks with suitable electrical resistances, which should be achieved by reducing the interconnection and air electrode interfacial resistance.

3.0 INTRODUCTION

This report constitutes the annual report, under DOE Continuation Contract No. DE-AC-0379ET11305. Presenting progress on work from April 1, 1978 through March 31, 1979, this report actually builds on and continues from the level of technology attained on the HTSOE fuel cell, during the initial two-year program for DOE, that ended on March 31, 1978.

4.0 THE PRESENT PROGRAM

The present two-year research program (DOE Continuation Contract DE-AC-0379ET11305, formerly DOE EY-76-C-03-1197), relating to the development of the high-temperature solid oxide electrolyte (HTSOE) fuel cell, is building upon the findings of the first two-year contract effort at Westinghouse.[1] It will demonstrate extended performance and life stability of thin film, HTSOE fuel cell stacks. The fuel cell stack, a multiplicity of series-connected cells, constitutes the basic building block of this fuel cell system. These stacks are being constructed, using the component materials and their fabrication processes developed in the past program, and those materials and processes that were further optimized during the first year of this program. Extended life will be demonstrated in single cells and small cell stacks, under conditions anticipated in the operation of stacks in a total fuel cell system. Other stacks will be tested to determine power output capability and the effect of fuel/air conditions on performance. Also, the reproducibility of stacks, with respect to cell-to-cell and overall performance, will be demonstrated, with at least 10 stacks constructed and evaluated for that purpose.

During the proposed program, four milestones will have been attained. For Milestone ▽1 all the five fuel cell components -- porous support tube, fuel electrode, solid electrolyte, air electrode and the interconnection -- will have been specified and the fabrication sequencing and fabrication techniques will have been established in a "bench mark" stack, delivering 10W of power. To attain Milestone ▽2

at least a single cell, including an interconnection, will have demonstrated a minimum of 1000 hours of life at 1000°C, under the following conditions:

- Current density of 400 mA/cm^2
- Voltage stability - No more than 10 percent degradation from the initial operating cell voltage of 0.66V in a H_2 +3% H_2O inlet fuel mixture.

Attainment of Milestone ⑵ will show that the thin film, high-temperature fuel cell concept and design is viable and should show promise of further life improvement toward that required for applications as cited in Appendix B. Achieving Milestone ⑶ will require that a small fuel cell stack, having at least 20 series-connected cells, demonstrate a minimum of 1000 hours of operation, under the same conditions as for Milestone ⑵. Milestone ⑷ will be attained when 10 stacks will have been fabricated and tested, for a short time, to demonstrate reproducibility in materials fabrication and uniformity in cell and stack performance. The same test conditions as described for the other milestones will be used to operate the 10W stacks.

Therefore, the program will evaluate the components and verify the fabrication techniques developed to produce them. It will establish the ability of these components to operate properly in contact with each other in the thin film design under simulated service conditions. Also it will determine the long-time stability characteristics both of the components and their interfaces and of cell and cell stacks under simulated service conditions. Finally, sufficient cell stacks will be fabricated to verify their reproducibility, performance and life. With these objectives attained, the basic building block of the HTSOE fuel cell generator will have been firmly established.

Upon achievement of the milestones of this proposed program, the high-temperature, solid oxide fuel cell development program will then be advanced to the stage of system selection, design, prototype construction and testing.

5.0 OVERALL TECHNICAL EFFORT

The overall technical effort is aimed at achieving four milestones in the two-year period of the contract. These include:

(1) Specifying all five fuel cell components, their fabrication sequencing and their fabrication techniques in a "bench mark" stack, delivering 10 watts of power;

(2) Demonstrating, at least in a single cell with an interconnection, a minimum of 1000 hours of life at 1000°C, under the conditions of 400 mA/cm^2, no more than 10 percent voltage degradation from initial loaded voltage, using H_2/3% H_2O inlet fuel mixture;

(3) Demonstrating (2) in a fuel cell stack of at least 20 series connected cells;

(4) Fabricating and testing, for a sufficient time, 10 stacks to demonstrate reproducibility in materials fabrication and uniformity in cell and stack performance.

5.1 TASK 1. DEVELOPMENT AND REFINEMENT OF FABRICATION PROCESSES

Work in this task includes:

1) Fabrication of the cell interconnection by the EVD process
2) Definition of the fuel electrode stack process
3) Definition of the air electrode stack process
4) Porous support tube refinement
5) Cell stack preparation

5.1.1 Subtask A. Interconnection Fabrication

Work on this subtask dealt with the incorporation of magnesium into the lanthanum chromite interconnection composition and on the electrochemical vapor deposition of interconnection film in 20 cell stack lengths of tubing.

Also, radio frequency (RF) sputtering of interconnection films of modified lanthanum chromite onto fuel electrodes, which had been previously deposited onto a porous support tube, was also investigated.

5.1.1.1 Magnesium Incorporation in Lanthanum Chromite Interconnection

Lanthanum chromite, with magnesium and aluminum substitutions for part of the chromium in the ABO_3 perovskite crystal structure, has been demonstrated[2] to be a suitable material for use as the cell interconnection material for the thin-layer high-temperature fuel cell. In this crystal structure the lanthanum ions reside in the large A sites, coordinated to twelve oxygen ions, while the chromium ions reside in the much smaller B sites, coordinated to six oxygen ions. Magnesium or aluminum can replace an appreciable atom fraction of chromium on the small B sites, while larger ions, such as strontium or barium, can be substituted for large fractions of the lanthanum on the much larger A sites. These oxides are often made with an atomic ratio

$$\frac{Cr + Al + Mg}{La} > 1.$$

This is a ploy to decrease the possibility of free lanthanum oxide which can react with water vapor in the air and cause the sample to disintegrate by hydrolysis. It has been suggested by Anderson [3] and in our experiments that all, or nearly all, of the magnesium in solid solution in the lanthanum chromite resides at the normal chromium sites

(coordinated to six oxygen ions). The remainder of the magnesium, such as in the normal composition, $La_{.95}Mg_{.05}Cr_{.75}Al_{.25}O_3$, is in a second phase, perhaps the spinel $MgCr_2O_4$, or MgO. Although the small quantity of second phase is difficult to detect by X-ray diffraction, measurement of the total dissolved magnesium, based on maximum oxygen loss measurements at low oxygen pressures, by ourselves and Anderson, for the above composition, indicate that part of the magnesium exists as a second phase. To further explore this possibility, we examined a variety of magnesium-doped lanthanum chromite samples (prepared by mixing the pure oxides and sintering at 1600-1700°C) using the Direct Imaging Mass Analyzer (DIMA). These all showed a second phase with magnesium, usually associated with chromium, except for compositions with $\frac{Cr + Al + Mg}{La} = 1$. Fig. 5.1a shows the lanthanum, chromium, and magnesium ion images from the DIMA apparatus, illustrating this behavior for a bulk sample of nominal composition $La_{.95}Mg_{.05}CrO_3$.

Our data suggest that we can attain an (essentially) one-phase interconnection layer of lanthanum chromite with magnesium, using the EVD technique, as illustrated in Fig. 5.1a. However, second phase magnesium has been detected in some instances, such as illustrated in Fig. 5.1b. In this instance the second phase contains Mg but not Cr. The experimental parameters of the EVD process associated with the presence or absence of such second phase magnesium are still under investigation.

5.1.1.2 Radio Frequency (RF) Sputtering of Interconnection Material

RF sputtering is used to produce films of interconnection material of controlled composition for bulk property evaluations and for standard stack properties. In the past, films were made by spreading a layer of either of the following powders:

a) $La_{.84}Sr_{.16}CrO_3$

b) $La_{0.95}Mg_{0.05}Cr_{0.75}Al_{0.25}O_3$

Lanthanum Ion Images	Chromium Ion Images	Aluminum Ion Images	Magnesium Ion Images

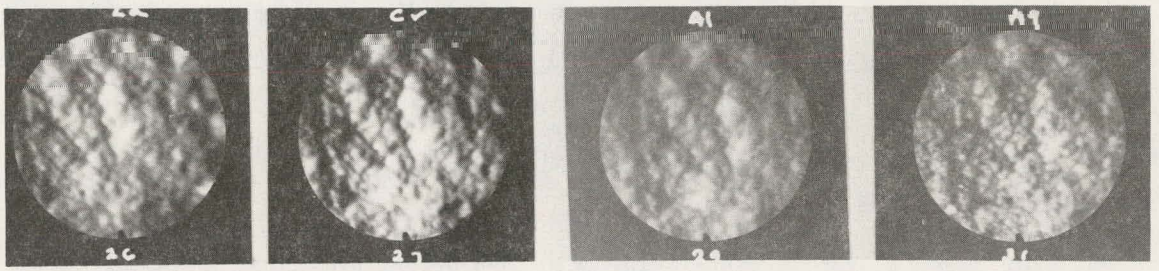

a. Normal $LaCr_{1-xy}Mg_xAl_yO_3$ Layer made by EVD

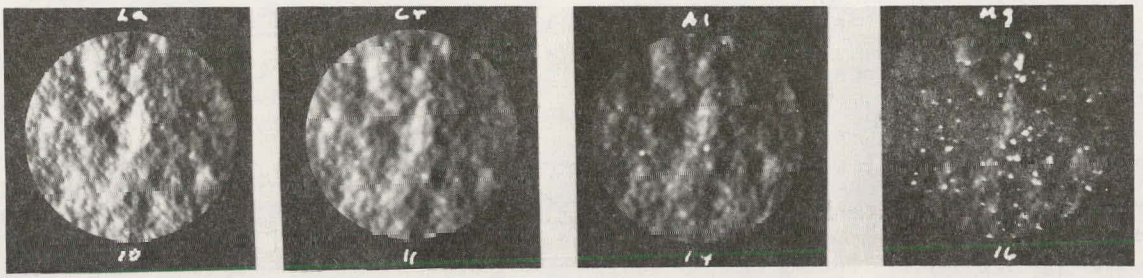

b. $LaCr_{1-x-y}Mg_xAl_yO_3$ Layer made by EVD But with a Second Phase Containing Mg Ion

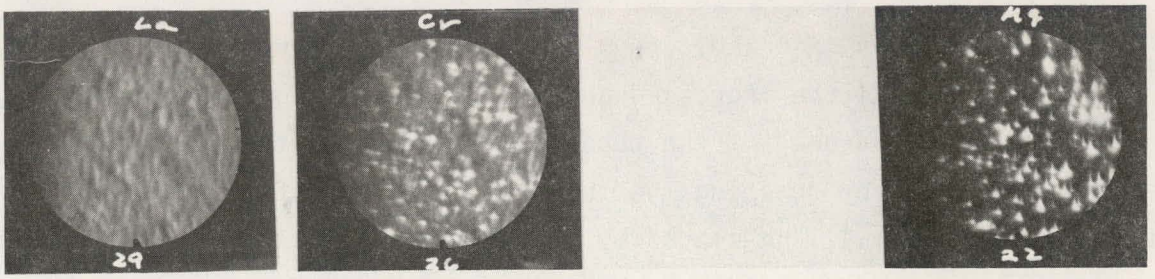

c. $La_{.95}Mg_{.05}CrO_3$ made by Mixing the Individual Oxides and Sintering at 1700°C

Fig. 5.1 Lanthanum Chromite Materials Prepared by Two Methods -- Patterns from Direct Imaging Mass Analyzer

onto the RF sputtering electrode. This method of sputtering the powders gave very erratic films which were not reproducible[1].

The present films are sputtered from a 10 cm diameter x 0.6 cm thick "hot pressed target" of the desired composition. Runs 1, 2 and 3 used the $La_{.84}Sr_{.16}CrO_3$ target sputtered onto prefired alumina squares (see Table 5.1). These films were used to determine the sputtering rate at a fixed target to substrate distance.

For the following runs, the sputtering target was changed to $La_{0.95}Mg_{0.05}Cr_{0.75}Al_{0.25}O_3$. On Runs 4, 5, 6 and 7 the films were placed on prefired alumina squares and split tubes of zirconia, coated with the nickel cermet fuel electrode coating. The substrates were attached to a heated graphite block. The produced films were porous so the power level and temperature were varied to overcome this porosity. The films on the zirconia tubes varied with thickness, depending on their distance to the target. It was noted that the films had cracks and these cracks followed the planar direction, that is, perpendicular to the target. Run #8 was a whole tube which was heated by a cartridge heater. The heater was placed inside the tube, which was rotated during the deposition. Fig. 5.2 shows such a substrate arrangement.

The film was thin and porous but, otherwise, very uniform. The film thickness will be increased and the porosity reduced by changing the rotating speed of the tube and reducing the target-to-substrate distance. By rotating the tube slower, the surface cavities in the zirconia tube will be closed by the $La_{0.95}Mg_{0.05}Cr_{0.75}Al_{0.75}O_3$ sputtered film.

The Ni-Cermet coated, porous support tubes were heated and rotated during the deposition of $La_{.95}Mg_{.05}Cr_{.75}Al_{.25}O_3$ films. To rotate the tubes during deposition a 0.05 mm support sleeve of molybdenum

TABLE 5.1 RF SPUTTERED INTERCONNECTION FILMS

Run# Tube#	Sub-strate	Material Sputtered	Sputter Time, Hours	Power, Watts	Substrate Temp., °C	Film Thickness, Microns	Remarks
1	A	$La_{.84}Sr_{.16}CrO_3$	2.7	100	---	---	Film uniform.
2	A	$La_{.85}Sr_{.16}CrO_3$	18.0	100	500	4.40	Film had good adhesion.
3	A	$La_{.84}Sr_{.16}CrO_3$	72.0	200	470	65.0	Film flake off.
4	A-B	$La_{0.95}Mg_{0.05}Cr_{.75}Al_{.25}O_3$	98.0	200	520	70.0	Film on tube was pitted and porous.
5	A-B	$La_{0.95}Mg_{0.05}Cr_{.75}Al_{0.25}O_3$	30.4	200	460	31.16	Tube heated-not-pitted, more dense still porous.
6	A-B	$La_{0.95}Mg_{0.05}Cr_{.75}Al_{0.25}O_3$	100	100	440	47.44	Decreased power level and increased sputter time.
7	A-B	$La_{0.95}Mg_{0.05}Cr_{.75}Al_{0.25}O_3$	78	100	515	53.5	Increased film density - film conductive.
Z8	A-B	$La_{.95}Mg_{.05}Cr_{.75}Al_{.25}O_3$	70	100	400	16	Tube heated and rotated. The film had uniform thickness; was conductive when wet.
Z9-77	A-C	$La_{.95}Mg_{.05}Cr_{.75}Al_{.25}O_3$	216	100	450	64	Flexible cable broke. Rotated by hand. Diffusion pump burned out.

TABLE 5.1 RF SPUTTERED INTERCONNECTION FILMS (Cont'd)

Run# Tube#	Sub-strate	Material Sputtered	Sputter Time, Hours	Power, Watts	Substrate Temp., °C	Film Thickness, Microns	Remarks
Z10-87	A-C	$La_{.95}Mg_{.05}Cr_{.75}Al_{.25}O_3$	235	100	370	52.17	Pores filled with zirconia slurry. Heated, rotated 100° every hour.
Z11-87	A-C	$La_{.95}Mg_{.05}Cr_{.75}Al_{.25}O_3$	168	100	350	38.33	New target, Westinghouse hot pressed. This run to clean the target.
Z12-70	A-C	$La_{.95}Mg_{.05}Cr_{.75}Al_{.25}O_3$	286	100	350	78.74	Certain areas of tube masked with aluminum foil.
Z13-70	A-C	$La_{.95}Mg_{.05}Cr_{.75}Al_{.25}O_3$	173	100	400	25.4	Tube masked. Hole burnt in electrode water cooling - flooded pump.
Z14-41	C	$La_{.95}Mg_{.05}Cr_{.75}Al_{.25}O_3$	100	100	425	18.8	1st run after vacuum system repaired.
Z15-40	A-C	$La_{.95}Mg_{.05}Cr_{.75}Al_{.25}O_3$	24	100	384		"Acro Dag G" used instead of aluminum foil as masking.

A = = Prefired alumina square.

B = = Split cermet fuel electrode coating.

C = = Zirconia tube with nickel-cermet fuel electrode coating.

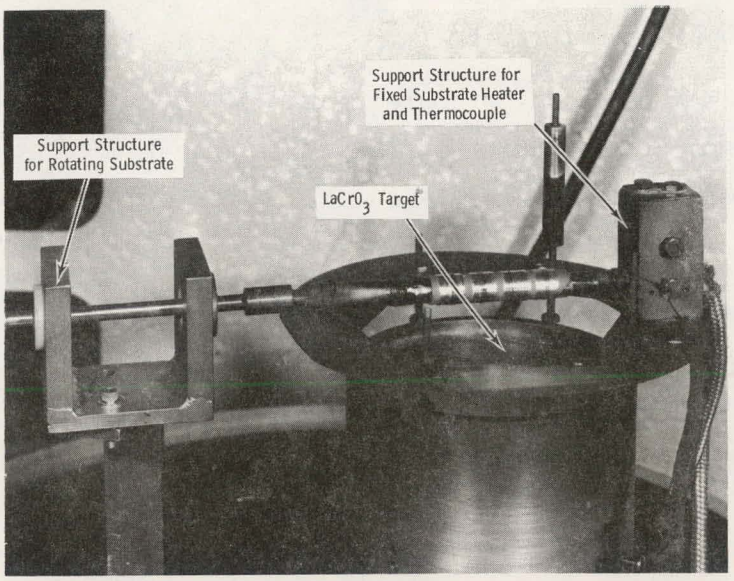

Fig. 5.2 Arrangement of Substrate and Heater Over Target in RF Sputtering System

metal was placed inside the tube. This sleeve was attached to a drive shaft connected to flexible cable and feed-through the base plate to a speed-controllable motor. Inside the molybdenum sleeve was a stationary cartridge heater with a thermocouple attached to monitor the heating.

After 43 hours of sputtering (Run #Z9-77), the outside flexible cable broke, due to excessive stress, from which time on, the tube was rotated by hand 180° and 90° and then repeated for a total time of 216 hours. Also the diffusion pump failed after 168 hours so that Run Z9-77 was considered inferior.

Cross-sections of the coated sample of Run Z9-77 are shown in Fig. 5.3. Note the irregularity of the film. The thickness of the $La_{.95}Mg_{.05}Cr_{.75}Al_{.25}O_3$ sputtered layer was measured microscopically and the porosity of the film was studied.

The zirconia tube, when covered with the fired Ni-Cermet electrode, is very porous. It is difficult to close this porosity with a dense interconnection layer. To overcome this obstacle for dense films, a slurry of yttria-stabilized zirconia powder was rubbed into the tube's surface irregularities and then the interconnection material was sputtered onto the preconditioned tube (Run Z10-87).

The potted and polished cross sections of this run are shown in Fig. 5.4. One observes some crack-like features in the film and one observes the rings, created by the intermittent rotation of the tube, during sputtering. During this run, an automatic timer activated the motor for rotating the substrate tube. The tube was turned about 100 degrees every hour. The interconnection film appeared to be smooth and had good coverage over the filled holes of the fuel electrode. To test gas tightness, the ends of the tube were closed and vacuum was applied. The film showed (for the first time), that considerable improvement in film density was achieved by RF sputtering.

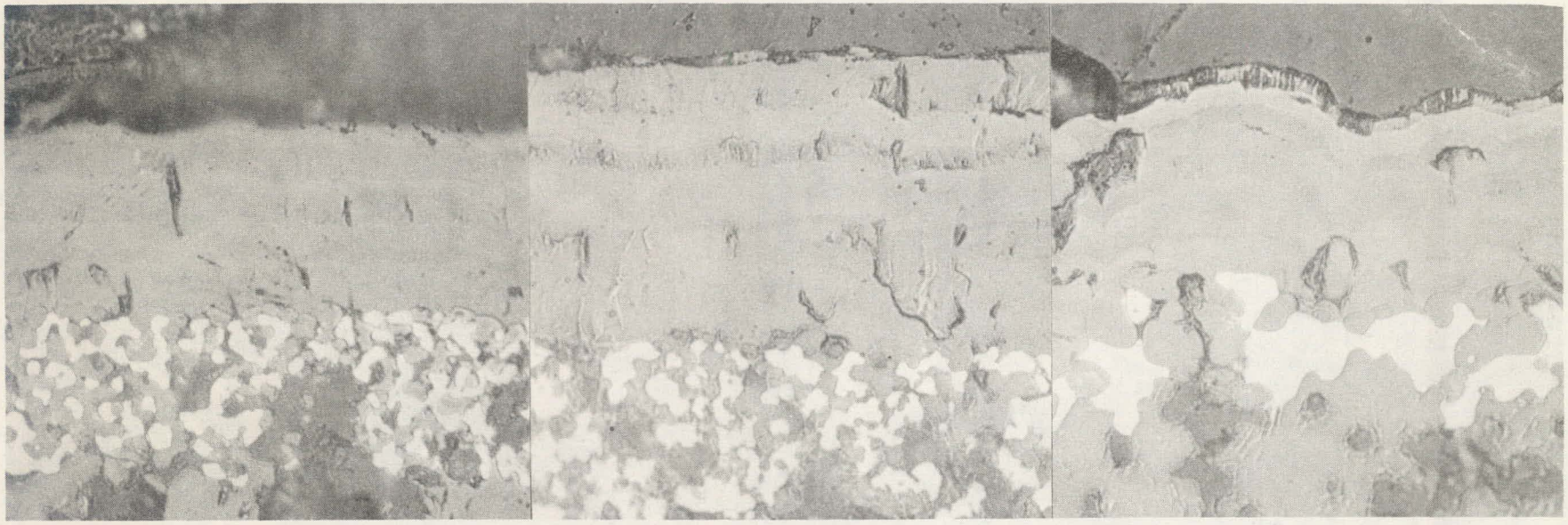

Left Center Right

Fig. 5.3 Cross Sections of Run Z9-77, Showing the Sputtered $La_{.95}Mg_{.05}Cr_{.75}Al_{.25}O_3$ Layer on the Nickel-Cermet Fuel Electrode

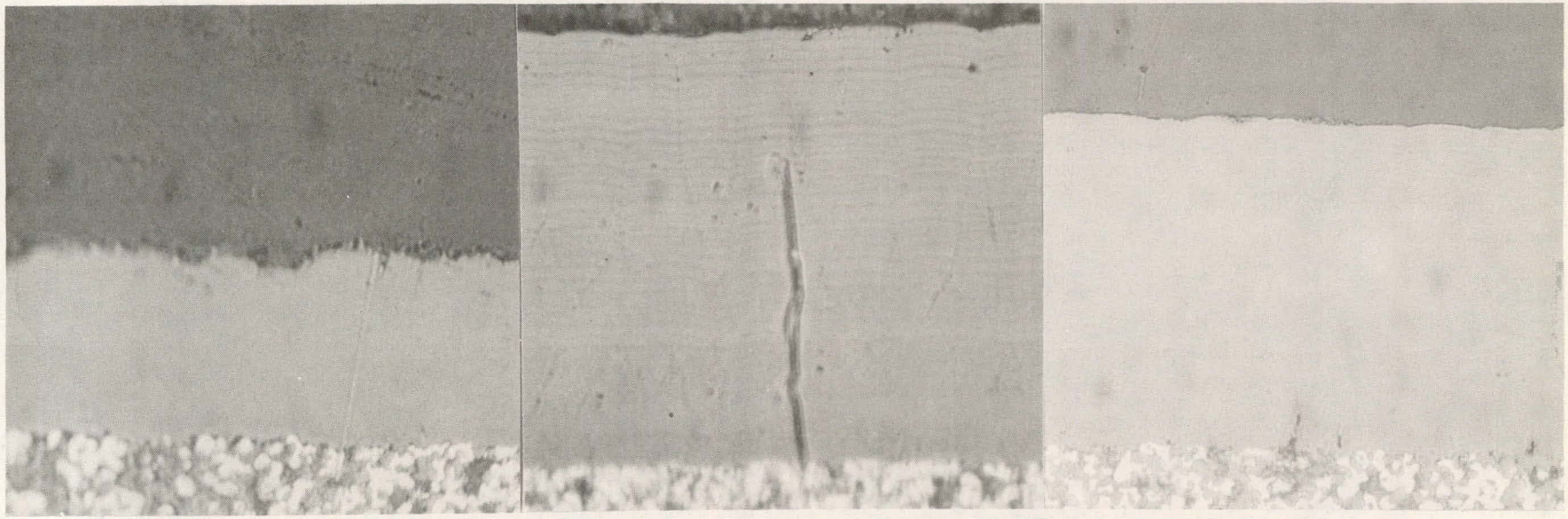

Left
54.4 μ thick

Center
89.1 μ thick

Right
107.0 μ thick

Fig. 5.4 Cross Sections of Run 10-87 Nickel-Cermet Coated Fuel Electrode (with Surface Pores Prefilled with a Slurry of Yttria-Stabilized Zirconia and then $La_{.98}Mg_{.05}Cr_{.75}Al_{.25}O_3$ Sputtered on Sections Along Tube Length)

RM-77437

During previous experiments, all $LaCrO_3$ targets were bonded to the RF electrode. Through heating and cooling the target cracked. These targets had been made by an outside vendor and the target density was low so that its mechanical strength was insufficient. Therefore, a graphite die was built and a new target was hot pressed, in house, from purchased powder. The set-up shown in Fig. 5.5 was used in the hot pressing of the 10 cm diameter x 0.6 cm thick target to a density of nearly 97%. An RF heater was used to heat the die and powder in a nitrogen atmosphere. Only graphite was used to hold the powder charge. A 6.4 cm diameter hydraulic press was used to apply the necessary pressure which was applied at room temperature, then the temperature was raised. The optimum pressure and temperature for fabricating the $La_{.95}Mg_{.05}Cr_{.75}Al_{.25}O_3$ target is 3000 psi and 1650°C. Pressing time at maximum temperature was 2-3 hours*. After hot pressing, the target was ground to remove any undesirable surface materials, due to the contact with graphite at elevated temperatures.

The sputtering system was cleaned and reassembled with the in-house hot pressed $La_{.95}Mg_{.05}Cr_{.75}Al_{.25}O_3$ target. A 5 mil indium foil disc was placed between the target and RF electrode to enhance the electrical contact.

Run Z11-79 went for 168 hours, to clean up the new target. A thermocouple was wrapped around the cartridge heater to monitor the temperature. After this run the $LaCrO_3$ target looked very smooth and clean.

Run Z12-70 was used to experiment with methods of band masking. First the Ni-Cermet fuel electrode was coated with aluminum foil, exposing the area on the tube to be coated with the interconnection material. These foil bands were spaced as shown in Fig. 5.6. The $La_{.95}Mg_{.05}Cr_{.75}Al_{.25}O_3$ films have a smooth and dense appearance.

---

*This work was done by C. A. Anderson, J. A. Kuszyk and W. J. Carmen of the Westinghouse Research Laboratories.

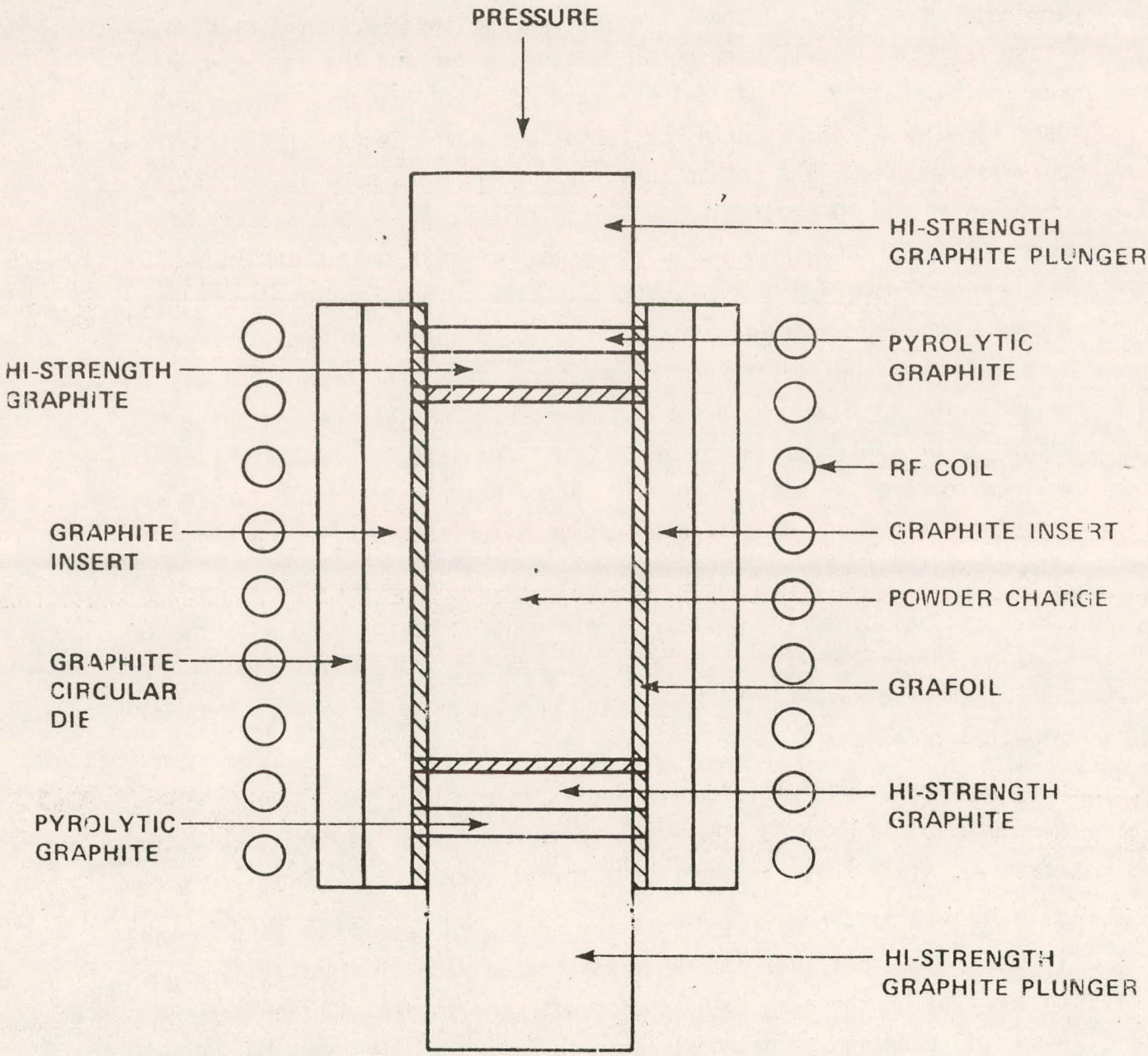

Figure 5.5. Hot-Pressing Apparatus for Fabricating Interconnection Materials (N_2 Atmosphere, Target: 4" diameter x 1/4" Thick)

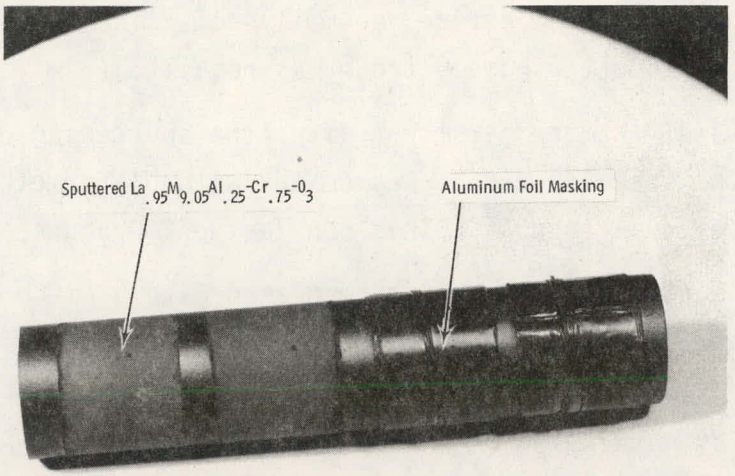

Fig. 5.6 Sputtered interconnection layer over Ni-cermet fuel electrode

Run Z13-70 was the other half of the Ni-cermet fuel electrode used in Run Z12-70. In this run the pores of the tube were filled with a slurry of yttria-stabilized zirconia in water, dried and 1 cm wide aluminum foil bands, spaced 3 mm apart, wired onto the tube. This 3 mm gap is to be the location of the interconnection layer of the fuel cell. The prefired alumina squares to be coated with La CrO_3 in this run were sprayed with "Aero Dag G" to aid in releasing the sputtered film. After 173 hours the system was shut down because of water leak in the sputtering electrode, which flooded the entire vacuum system. The vacuum system was cleaned and the sputtering electrode was rebuilt.

Run Z14-41 was the first run after the sputtering electrode was repaired. The stabilized tube was coated with Ni-Cermet and had aluminum foil sleeves around it. This run lasted 100 hours.

Run Z15-40 was a Zirconia tube coated with a Ni-Cermet electrode. The tube was masked before the interconnection layer was applied by coating with a graphite layer. This should allow the removal of the sputtered film over areas that are to be free of IC coatings. The deposits have yet to be analyzed.

5.1.1.3 Interconnection Fabrication by Electrochemical Vapor Deposition (EVD)

Both, electrolyte and interconnection (IC) material are deposited as thin layers by EVD. Since both must be deposited in succession, it is important to choose deposition conditions that will not harm the precursor layer material. Of special importance is the minimization of, or elimination of, interaction in the overlap region in the IC area, which must provide a durable, gastight bond between the two materials. Fig. 5.7 depicts two possible IC configurations, where the left one was produced by overlapping the electrolyte over the IC film (electrolyte

Dwg. 7690A93

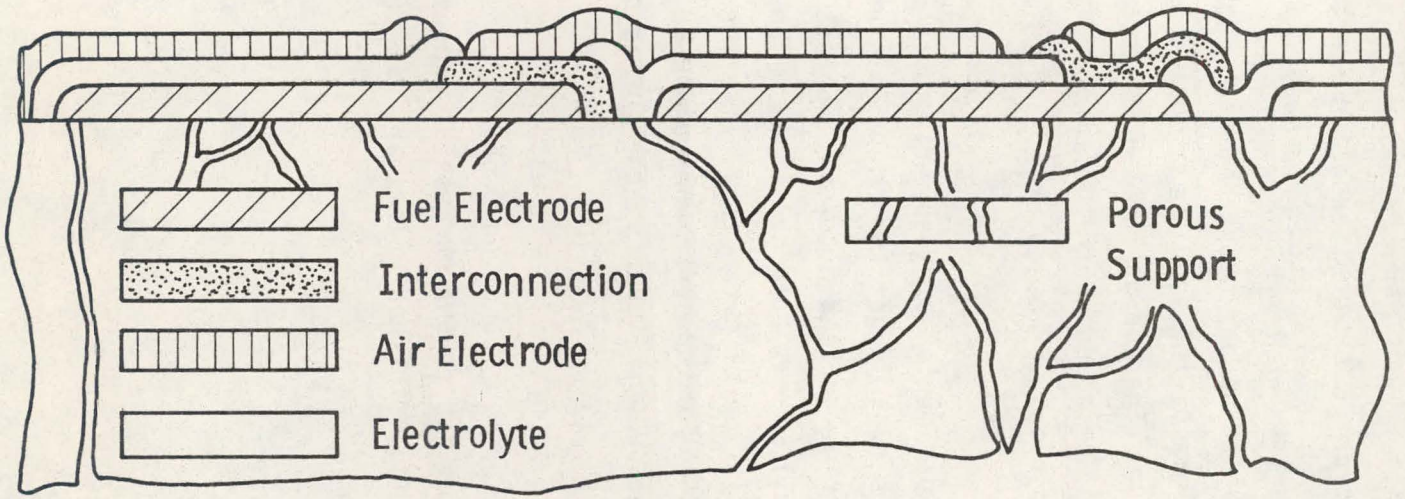

Fig. 5.7 – Schematic cross section of adjacent cells, showing two methods of sealing in the interconnection region

deposition after IC layer deposition) and where the right configuration was produced in the reversed order (IC deposited after electrolyte deposition).

Both IC configurations are under investigation. Each can be modified to a certain degree. Some of the problems associated with the deposition sequence lies in the masking and/or removal of deposits in undesirable stack areas. Liquid honing and sand blasting are the two prime processes that are used to clean up masked areas and to remove solid deposits.

A difficulty in our experimental program was experienced during the deposition of gastight layers over longer (30 cm long) stack tubes. During these scale-up experiments we noticed excessive support tube fracturing when the length of cell stacks exceeded 15 cm. The reason for this lies in a complex association of parameters, like thermal expantion mismatch, tube strength, attack on support tubes under reducing conditions and chemical attack of support tubes by the formation of corrosive reaction products during the EVD deposition. Tube strength, however, seems to be of paramount importance. The recognition of all these problems (particularly, reduction attack on support tubes, investigated during the last quarter) has led to the successful processing of long stack tubes, and tests of long, finished stacks are expected in the next few months.

The vapor deposition apparatus has been modified, so as to allow accurate measurement of oxygen activity in the H_2/H_2O mixture that passes through the inside of the cell stack tube, during the deposition of interconnection and electrolyte films. Hydrogen and oxygen are mixed at reduced pressure ($\sim$10 mm Hg) in the cold zone; then this mixture is passed through an alumina wool plug, that is positioned inside a quartz tube, and heated to 800°C. The resulting H_2/H_2O mixture flows over a closed-end zirconia tube, serving as an oxygen sensor, and finally enters the EVD reactor. The oxygen sensor measures the oxygen activity and activates safety valves when the oxygen activity increases over a set point (excess oxygen). This feature introduces increased reliability to the deposition process and eliminates the possibility of nickel electrode oxidation, due to improper flow meter adjustment or line pressure fluctuations. Fuel electrode oxidation had been experienced on several occasions in past EVD runs, before the use of the oxygen gage.

Also, a new and improved cartridge for halide delivery has been designed and fabricated. The new system reduces undesirable contamination of film material from structural components of the cartridges, stemming from their attack by chlorine at elevated temperatures.

In addition, an all new gas valving system has been installed on the EVD apparatus that reduces the possibilities of leaks and increases reproducibility in deposited films. The new system, made entirely of glass and teflon tubing, minimized the chances of leaks associated with corrosion as can occur when standard fittings are used. The majority of connections are now ground glass joints. All carrier gases and non-corrosive gases have been "hard" plumbed and pressure tested for leaks.

The graphite delivery cartridges used in the deposition of interconnection material have been re-designed with emphasis placed on symmetry and purity of deposited films. Fig. 5.8 shows two of the new cartridges. The upper one is an assembled cartridge that has been used in several deposition experiments. It is a three chambered design and permits deposition of a three component system. The lower cartridge is four chambered and shows (in exploded form) the internal design and

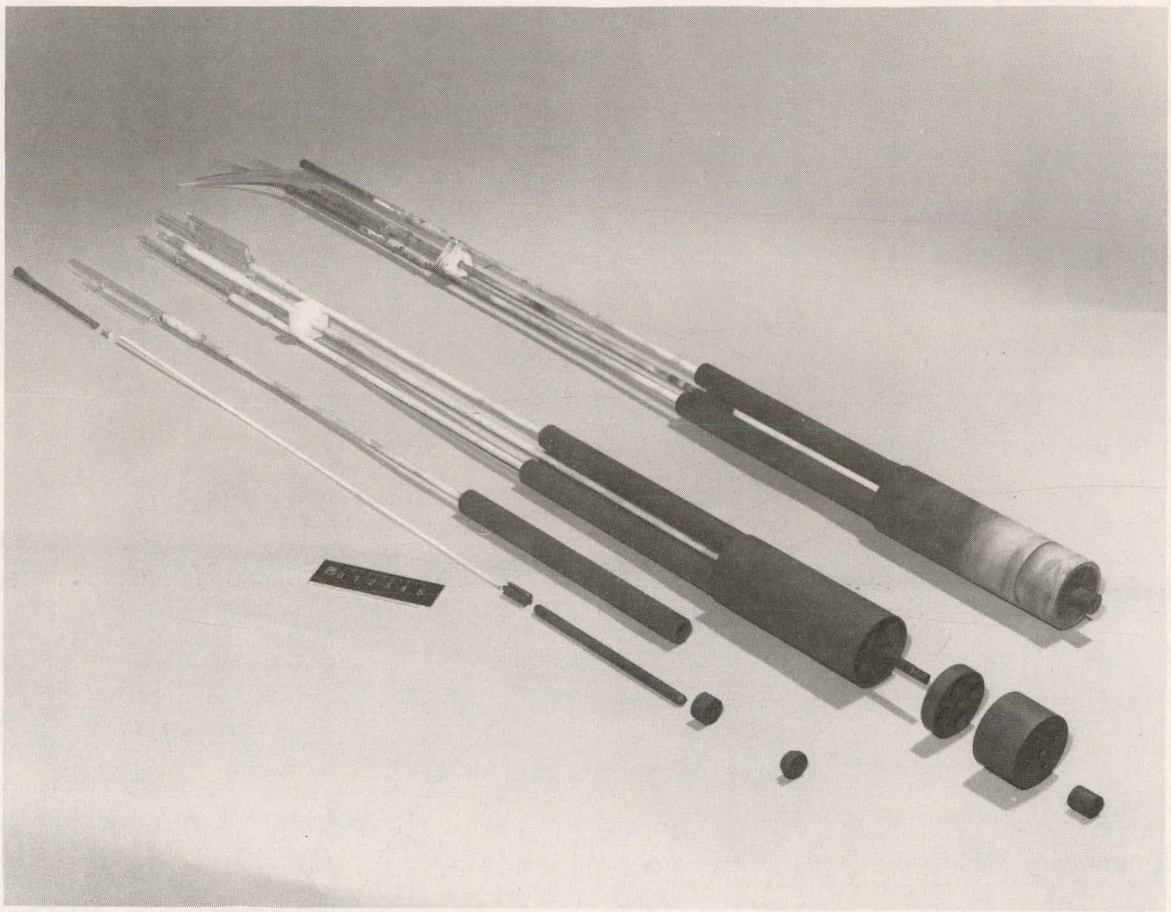

Fig. 5.8 Graphite Delivery Cartridges Used in the Deposition of Interconnection Material

associated pieces. Spring-loaded pistons in each chamber help to maintain uniformly packed beds of reactants throughout the duration of the deposition process. Replacement parts are available for all cartridges.

5.1.1.3.1 Interconnection (IC) Deposition Experiments

Initially, attempts were made in doping the modified lanthanum chromite with 25 mol-% of alumina. These experiments were carried out on 0.3 m long extruded tubes (manufactured by LECO Corp.) in order to gain expertise in fabricating long coatings. Non-uniform coatings were obtained, which had both high alumina contents at the front end of the tube and exhibited a flaky appearance. Elimination of alumina did not eliminate the film cracking on long tubes. The films flaked severely at 15 cm down the tube length, they became more adherent further downstream and upstream. Attempts at film growth on slip cast tubes (from ZIRCOA Corp.) resulted in similar deposits and the occurrence of porous support tube cracking posed an additional problem to that of producing uniform, IC film deposits.

At this time, alumina doping efforts were postponed, so that other problems could be resolved. The ensuing experiments were continued with LECO extruded tubes. Short time depositions (15 minutes) were conducted, to save halide source materials and time. Long uniform coatings were finally obtained, and an attempt was made to produce a thick coating over a 0.3 m long tube. The run was successful, however, tube bending by sagging at temperature (1350°C) was observed during a one hour deposition time. The tube is shown in Fig. 5.9. Here some of the IC film has been removed, in bands, to expose the fuel electrode. At the maximum stress point of the tube, some IC flaking is observed and it was concluded that the cause was shearing stress, which prevailed when the tube bent, during the 1350°C deposition. It was also concluded that the cracking of slip-cast zirconia tubes, which also occurred, could be caused by mechanical bending stresses during deposition.

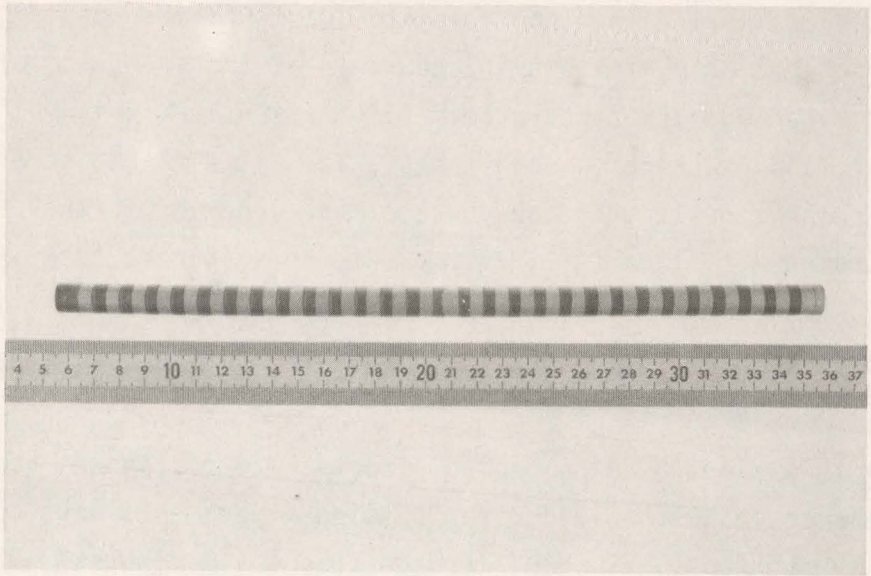

Fig. 5.9 28-Cell Stack Before Electrolyte Deposition (Note Flaking at Interconnection in Center and Tube Bending, due to Sagging While at 1350°C)

To investigate the cracking problem, we constructed a new tube support, that allows tube rotation during deposition. The first experiment with rotation was done with a slip cast tube (that was known to always crack in prior EVD runs). A uniform and more tenacious coating was obtained but the tube still cracked in the longitudinal direction. However, this ruled out bending forces as the culprit for cracking. The slip cast tubes were previously analyzed and were found to be both strong and of correct composition. Therefore chemical attach was considered to be the reason for tube deterioration.

Further EVD coating experiments revealed that with higher porosity in the tubes, film adherence was reduced and tubes became more brittle during processing. The problem of film adherence was correlated to the phenomenon of fast nucleation during the CVD phase (pore closure) of the EVD process. This problem was eliminated by reducing the oxygen activity in the internal purge gas by CO_2/H_2 admixtures, during the initial phase of deposition (that influences film adherence most). While the adherence problem was resolved, yet another problem was introduced, namely, by decreasing the oxygen activity in the gases, pore closure took place more slowly, allowing the nickel of the fuel electrode to alloy at elevated temperature with lanthanum, magnesium and chromium (stemming from the chlorides). The result was the formation of low melting eutectic alloys, that fused during deposition, thereby destroying the fuel electrode.

Another set of EVD experiments eliminated this problem, in which the oxygen activity was increased to an acceptable level that both eliminated flaking and fuel electrode deterioration. The weakening of the porous support tubes, however, was still a persistent problem and no porous support tube stack could be processed to the state of testing without cracking or crumbling.

Further investigation led to the conclusion that the HCl, formed during the initial phase of vapor deposition, interacts with the porous

calcia-stabilized zirconia and destabilizes the tube material by calcia-leaching. This becomes more evident when the porosity is high and only small "bridges" exist between sintered grains. Very little attack and crystallographic changes of these bridges will cause the tube structure to deteriorate with every further temperature cycle. Again, it must be noted, that the first successfully tested stack (under the initial two-year program) was built on a much less porous tube which would not make this problem obvious.

To investigate the "calcia-leaching" concept, we selected tubes that were most susceptible to deterioration and which were known to crack during the EVD process; namely, the ZIRCOA Corp. slip cast tubes. The tubes were equipped with fuel electrode coatings and were impregnated with a calcium nitrate solution, that was dried. The tube was then heated in forming gas to decompose the calcium nitrate to calcium oxide and contained 9 mg calcium oxide, precipitated in the pores of a 1 cm^2 surface area tube segment. This tube could be processed through all steps. A 7-cell section of this tube has been tested as a stack, see Section 5.2.5. The tube did not show obvious weakening of the structure. Therefore, it is assumed, that HCl, evolving during the CVD phase of pore closure (both during IC and electrolyte EVD) is gettered by the very active calcium oxide in the pores. This assumption is confirmed by the detection of a "salty matter" on the cold inner tube support structure after an EVD run (probably calcium chloride). The analysis of the substances and x-ray analysis on brittle tubes is not completed yet to confirm these deductions.

5.1.1.3.2 Conclusions

Stack scale-up and the use of porous long tubes introduced a host of new and largely unexpected IC fabrication problems -- as tube bending during EVD, flaking of deposits because of gas phase nucleation (powder base layer) and tube deterioration. Aluminum-doping of deposits had to be postponed under the impact of all these adverse conditions. Fortunately, none of the new problems posed insurmountable difficulties and most have been alleviated.

5.1.2 Subtask B. Fuel Electrode Stack Process

Work in this area has involved extension and improvement of the fuel electrode fabrication technique, described in the final report of the past contract, to 20, or more, series-connected fuel cell stacks.

5.1.2.1 Furnace Fabrication

Target fuel cell stacks will consist of a minimum of twenty series-connected cells that can deliver 10 watts DC electrical power. The 20 cell stack requires the fabrication of longer fuel electrodes of nearly 0.3 m (~1 ft) in length.

Existing sintering furnaces did not allow the fabrication of such fuel electrodes because of limitations in length, heating rate, vertical mounting, and temperature level. It was not possible to locate a supplier to fabricate a furnace in a reasonable time span and of an acceptable price to satisfy program requirements. Required furnace characteristics are: an average heating rate of 60°C per minute up to 1700°C; vertical mounting, to prevent sagging of stack tubes; a uniform temperature zone of nearly 0.3 m.

A tube furnace, that satisfies all requirements mentioned above has been engineered, constructed and tested in-house, and long fuel electrodes can now be sintered routinely in this furnace. The furnace is heated by a molybdenum heating element which is protected by a forming gas atmosphere. The insulation consists of an alumina fiber mat (SAFFIL) and the tube material is high purity alumina.

5.1.2.2 Fuel Electrode Sintering

Fuel electrodes are prepared by the standard technique that involves dipping of the porous support tube into a nickel oxide/zirconia

slurry, drying, sintering in an oxygen containing atmosphere, cooling below the melting point of nickel, and, finally, reducing the nickel oxide to nickel. The mechanical integrity of the fuel electrode can be enhanced by sintering at high temperatures. Long time exposure of nickel oxide to stabilized zirconia at 1600°C, however, results in nickel oxide diffusion into zirconia. The extent of nickel diffusion determines the degree of nickel loss in the final cermet structure and, possibly, has a negative effect on electrical (electronic) and mechanical (phase segregation) properties.

The new sintering furnace allows short sintering times at high temperatures, thereby reducing the nickel diffusion and increasing the mechanical properties of fuel electrode (tested by scraping it with an alumina edge), as well as increasing electrical conductance. For fuel electrode sintering, the stack support tubes are slipped over an alumina centering rod, that, in turn, is supported by alumina structures in the vertically mounted furnace. Fuel electrode resistance values of below 0.02 $\Omega(\rho/\delta)$ at room temperature for 0.25 m long tube segments have been achieved. Such electrodes will exhibit 0.1 $\Omega(\rho/\delta)$ at 1000°C

The fabrication equipment to produce long fuel electrodes for 10 watt stacks is in place and fuel electrodes of 0.25 m length each, have been sintered, which show good mechanical and electrical properties. These tubes are used for interconnection EVD experiments.

As previously mentioned, fuel electrodes are prepared by dipping the porous support tube into a $NiO\text{-}ZrO_2$ slurry. During the dipping process the tube ends are closed to prevent inside coating. It has been found impractical to use this technique for tubes much longer than 0.20 m. During dipping, slurry liquid will filter through the porous tube wall and flow to the inside tube bottom. After removal of the tube from the slurry, this inside liquid washes the coated film from the outside. The longer the tubes, the higher will be the hydrostatic

pressure during tube dipping, causing an exaggeration of this problem, and resulting in nonuniform coatings over longer tubes. Fuel electrode performance, therefore, would vary over the stack length.

Dipping, however, is a fast coating method and results in obtaining fuel electrodes of superior smoothness and strength. Therefore, other methods have been rejected to coat long tubes. The search for new dipping methods resulted in the construction of a new holder for porous tubes, that is shown in Fig. 5.10. An inflatable rubber sleeve ① is held in position by a stainless tube ② with holes, which allows the inflation of the rubber sleeve via a valve ③ . This deflated assembly is introduced into the porous support tube ④ and by inflation of the rubber sleeve, allows safe handling of tubes of any length. During dipping, liquid cannot accumulate on the inside of the tube and excellent and uniform coverage of long tubes with fuel electrode slurry is achieved. The coated tube is easily removed from the holder by pressure release of the inflated rubber sleeve. This method of handling appears to be ideal for moving a large number of tubes from processing step to processing step, without danger of tube cracking.

5.1.2.3 Conclusions

Long nickel-zirconia cermet electrodes can now be fabricated in two compositions, namely 60 v/o Ni and 40 v/o Ni with a zirconia content of 40 v/o and 60 v/o respectively. The respective electrode layer resistance is about 2×10^{-2} Ω and 4×10^{-2} Ω. The electrodes of lower nickel content have a stronger ceramic skeleton and separate less easily from the support tube and electrolyte, yet exhibit higher voltage losses in an operating stack. Both electrode types will be used in future experiments and benefits and disadvantages with respect to stack performance will be explored.

Dwg. 7684A31

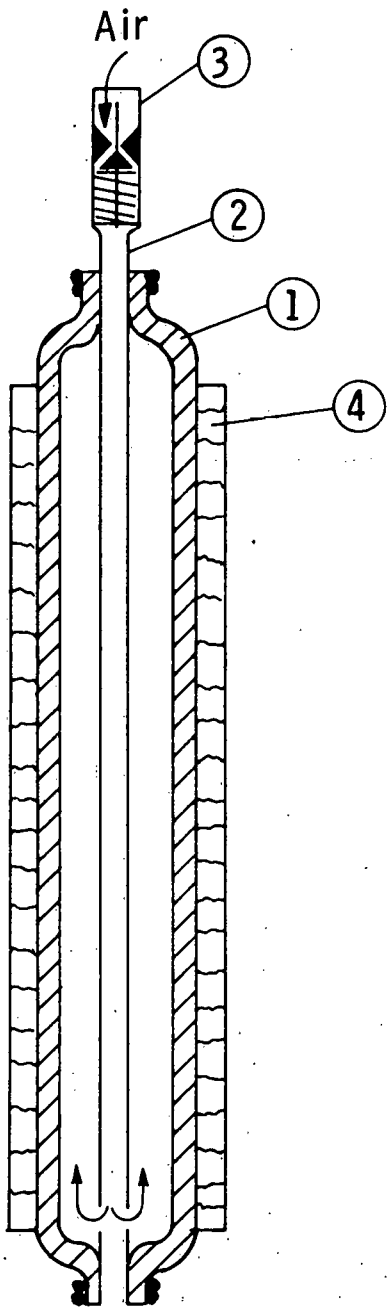

(1) Rubber Sleeve
(2) Stainless Tube
(3) Valve
(4) Porous Support Tube

Fig. 5.10 — Holder for porous tubes for applying slurry coatings

5.1.3 Subtask C. Air Electrode-Stack Process

Work in this area involved scale-up of the formulation and process to enable fabrication of 20 cell stacks.

5.1.3.1 Indium Oxide Current Collector

Past work on the air electrode involved expansion and improvement of the fabrication technique, as described in the final report of the past contract[1] to a stack of 20 series-connected fuel cells. Fig. 5.11 shows the partially completed CVD reactor for applying the doped, indium oxide current collector. This new reactor has a 40 cm long deposition zone, compared to only 25 cm in the previous reactor. It was not possible to obtain electrically uniform coatings at the ends of 25 cell stacks in the old reactor, due to reactant dilution effects at the end zones of the cross-flow reactor. However, the deposition conditions and basic constructional reactor characteristics have not been changed for the new reactor design.

Improvement of Electrical Contact In_2O_3/IC, Fig. 5.12 shows the initial phase of contact deterioration of the In_2O_3/IC interface. The lighter colored, spotty areas in the IC region represent the optical effect of layer separation (electrical contact loss). Several methods have been investigated to alleviate this problem.

1) increasing collector porosity during CVD
2) application of microporous In_2O_3 between the CVD layer and the IC

With regard to approach 1), the seeding of In_2O_3 grains onto the stack tube before the CVD process leads to nucleation centers for oxide growth during the deposition and creates porosity. The contact area of the large CVD crystals ($\sim$10 to 20 µm size) to the IC, however, is still too large and even these layers will flake and lose electrical contact.

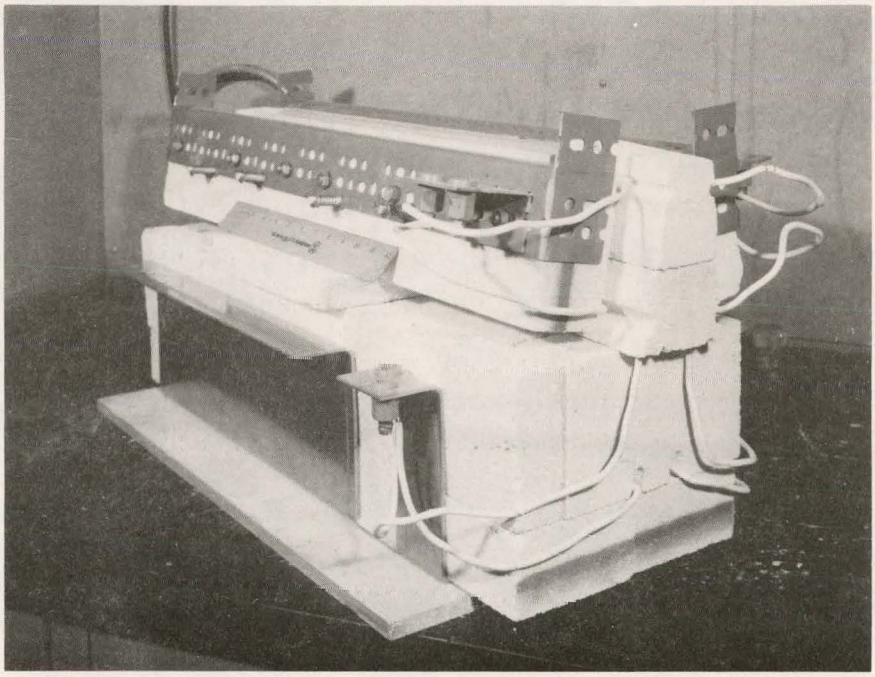

Fig. 5.11 New Cross-Flow CVD Reactor for In_2O_3 Current Collector Deposition

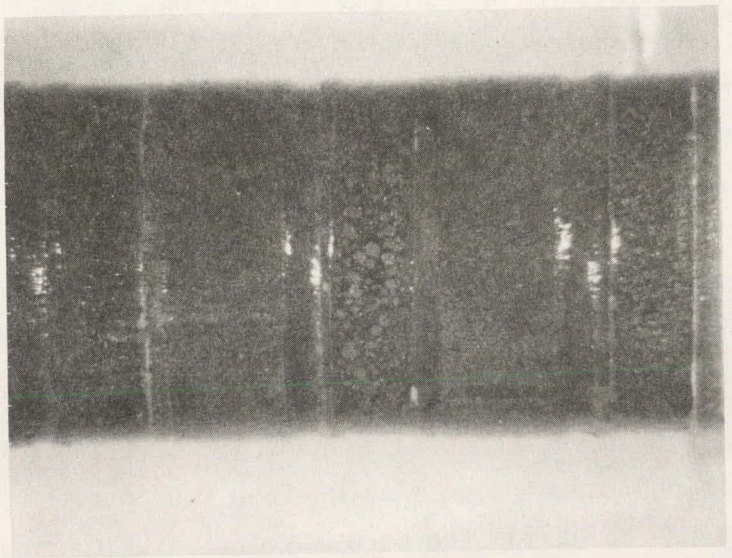

Fig. 5.12 Initial Phase of Contact Loss of In_2O_3 to Lanthanum Chromite in the IC Area

Regarding approach 2), we applied thin metallic coatings of indium-tin alloy to the surface of the IC (by painting at 200°C). This alloy was oxidized at 1000°C in air. The resulting oxide layer is microporous. The lateral resistance, however, of this coating is too high and an In_2O_3 CVD coating has to be applied over it. Due to rapid nucleation, this CVD coating will grow as a porous layer over the microporous In_2O_3 film. Some samples have been obtained that show stable electrical contact. However, severe problems were encountered in achieving uniformly painted metal layers. Variations of metal layer thickness in edge and corner areas lead to flaking during air oxidation. What proved to be possible on a flat surfaced sample did not appear to be reliable in overlap areas (surface steps in the IC region) of stacks. It could be concluded from this work, however, that the application of microporous oxide layers between the In_2O_3 collector and the IC can lead to stable mechanical and electrical contacts.

5.1.3.2 Lanthanum Manganite Air Electrode Current Collector

As described in Sections 5.1.3.1 and 5.2.4.1, we investigated methods of controlling indium oxide flaking from the interconnection material. Methods of increasing the porosity of indium oxide air electrode current collector did not result in improvements of electrical contact stability, see Section 5.1.3.1. This led us to the investigation of other oxides, that could be used as intermediate layers between the air electrode collector and the IC. The major problem arises when these layers are to be attached to the IC. The first material that becomes apparent for this porous intermediate layer is the IC material itself. The bonding, however, is a problem. Another possible material that has been used for air electrodes[4] is strontium-doped, lanthanium manganite. Therefore, we developed a sintering method, that allows the bonding of

these oxides to the solid electrolyte and the IC. The sintering is accomplished in a controlled atmosphere with the help of sintering aids. The sintering has to be accomplished below the melting point of nickel (1453°C). We found in our tests that, by using lanthanum manganite, even as a current collector, and replacing the doped indium oxide altogether, a good stack performance could be obtained, when the current collector was impregnated with praseodymium oxide and/or cobalt-praesodymium oxide. The stack performance, as shown in Section 5.2.5.4 is so stable and promising, that further investigation of this mixed oxide and other modified manganites as air electrode materials will be tried. This action (modifying the air electrode current collector composition) had to be taken, in order to solve the In_2O_3/IC connection problem. A potentially less complicated and less expensive air electrode can be obtained. As one can easily see (Section 5.2.5.4) the sensitivity to chemical reduction attack of such an air electrode is reduced. Furthermore, it is not prone to vaporization at temperature, as in the case of In_2O_3. The In_2O_3 air electrode current collector, however, will continue to be the object of further investigation, using intermediate porous oxide layers in the contact region to the IC.

5.1.3.2.1 Conclusions

Contact problems between the In_2O_3 and the IC have led to the investigation of other potential air electrode materials that could lead to better and less expensive air electrodes, as well as to less complicated fabrication techniques.

5.1.4 Electrolyte Deposition by EVD

The formation of thin layers of yttria-stabilized zirconia has been achieved with great reliability over many substrate samples of varying length, up to 30 cm, and longer. However tube cracking has been observed quite frequently in masked areas (IC area) and in inter-cell-gaps. HCL attack during EVD has been held accountable for weakening the porous structure of (especially weak) support tubes, by destabilizing the calcia-doped zirconia matrix. Also, it has been noticed, that stack tubes, coated with Ni-ZrO_2-cermet fuel electrodes containing 60 v/o Ni, are more prone to cracking than tubes having fuel electrodes with the lower nickel content (40 v/o). This indicates that the fuel electrode exerts mechanical stresses on the support tube, due to thermal expansion mismatch of nickel with the calcia-stabilized zirconia. The lower nickel content allows the zirconia skeleton in the electrode to control the thermal expansion.

However, the prevention of chemical and mechanical attack on the porous tube is the most important task that must be achieved. Recently we have been able to deposit long electrolyte films on extra-weak tubes, to prove that our preventive measures alleviate the problem of support tube cracking, during EVD runs.

In addition, a new approach has been taken for applying a porous electrolyte layer (which becomes incorporated into the air electrode) to the dense electrolyte. Before, a granular zirconia layer was applied to the fuel electrode that was incorporated by the growing electrolyte into a dense structure. By discontinuing the EVD process early enough, a consolidated, but uncovered granular zirconia layer, was left on top of the dense electrolyte. Although adequate, this porous layer had some disadvantages (missing tortuosity and fine porosity) because it was exposed to a two-hour deposition. Therefore, we investigated another method. Here, a dense electrolyte layer was deposited first, then the

porous zirconia layer was applied and fixed to the dense electrolyte layer by a short deposition run of only one-half hour. Although this approach requires an additional processing step, much better control over air electrode quality can be achieved, by optimizing the porous substructure of the air electrode. The improved porous electrolyte structure, that is a part of the composite oxide air electrode, resulted in the fabrication of an air electrode, that showed excellent performance in a five cell stack #3 (Section 5.2.5.3).

5.1.4.1 Conclusions

The deposition of long IC and electrolyte films no longer represents a problem. Support tube cracking, during EVD processing, has been recognized as a major problem that prevented the processing of long fuel cell stacks. The parameters, affecting tube deterioration and subsequent cracking, have largely been identified and longer fabricated stacks will soon undergo electrical testing.

5.1.5 Subtask D. Porous Support Tube Refinement

In-house fabrication of porous support tubes was refined and the tubes were analyzed with respect to their physical properties. Long tubes that were 0.3 m in length were fabricated for the 20 cell stacks. The success of fabricating long (>0.6 m) thin wall porous support tubes of uniform properties hinges on the processing cycle, beginning with the preparation of the proper powder particle size distribution by dry mixing and kneading. These tubes are extruded, mechanical handled, dried, and then fired.

Support tubes fabricated during this period showed flexural strengths of ∿5000 psi, tensile strengths >3000 psi and a porosity gradient of 25-50%. The porosity gradient from one end to the other of a 0.5 m long tube corresponded to the temperature gradient in the vertical firing furnace. Therefore, furnace modifications in the heat shields and mechanical support of the muffle system are in process to minimize the temperature gradient within the height of the muffle that houses the samples during the firing cycle.

5.1.5.1 Support Tube Fabrication

Porous support tube fabrication development covers the various stages of processing, from material preparation in the grinding stage to the evaluation of fired calcia-stabilized $(ZrO_2)_{.85}(CaO)_{.15}$ tubes.

Development of refinement techniques to fabricate porous support tubes of uniform physical properties requires good quality control of the starting powder particle sizes and the subsequent batching process for producing an extrudable material. The extruding batch material must be tailored for each extrusion with adequate strength to be self supporting, to prevent elongation and collapsing of the tubing during the fabrication process.

5.1.5.1.1 Support Tube Fabrication Experiments

The following process procedures were pursued in the refinement of support tube fabrication.

1) Starting powders of calcia-stabilized zirconia $(ZrO_2)_{.85}(CaO)_{.15}$, required for the porous thin wall tubing, were calcined at 1800°C and processed as reported earlier[1] for powder preparation.
2) Paste preparation started with dry blending powder fractions of 60 w/o (- 325 mesh) -40 w/o (- 400 mesh) in 450 gram batches.

The following is an example of a batch used in the preparation of an extrudable, plastic paste mixture:

Zirconia powder	86.0 w/o
Organic binder	5.0
Dispersant	0.6
Water	8.4
	100.0

The size of the laboratory kneading machine limited the batch size during the initial mixing process. Presently four 450 gram batches are successively mixed and combined into 900 gram batches for extrusion. Each 900 gram batch of material is extruded separately and produces five tubes, each (approximately) 0.6 m in length. The tailings of the two 900 gram batches are recombined in the kneading machine and extruded again, producing two more tubes, each 0.6 m in length. Therefore, a total of 12 tubes (0.6 m long) are fabricated from each extrusion operation. The length of extruded tubing was changed from 0.75 m to 0.6 m, to match the usable length of tubing required for firing. Also the 0.6 m tube length accommodated the effective "hot zone" in the verticle high temperature furnace.

The ratio of powder fractions was changed from 70/30 to 60/40 w/o ratio, to use the higher volume fraction of -400 mesh powder generated during powder processing. The change in the powder fraction ratio of the extrusion mix did not affect the processing parameters of producing support tubes of the desired apparent porosity ranges.

3) Firing

After the tubes were dried in the humidity drying oven, they were cut to length and a collar was cemented on one end, in preparation for hang-firing in the high temperature gas kiln.

Fig. 5.13 shows the modified schematic arrangement of the furnace set up with heat shields and a dense refractory base or pedestal used in supporting the muffle system.

Figs. 5.14 and 5.15 show the high temperature gas kiln in operation with a new working platform and a modified mechanical attachment to lift and move the furnace cover.

Fig. 5.16 illustrates the set of samples after firing. Presently eight tubes, as long as 0.6 m, can be charged and fired in the furnace.

Several firing experiments were run to establish a time-temperature reference schedule, by which the fired properties of porous support tubes could be compared.

Fig. 5.17 shows the results of the apparent porosity band of a 0.45 cm long tube fired at 1800°C for seven hours. It also shows the average shrinkage of the diameter of the tubes from the bottom section to the top section (7% to 5%, bottom to top).

Fig. 5.18 shows the porosity band of tubes fired at 1950°C for seven hours with the average diameter shrinkage of the porous tubes (12 to 7%, bottom to top).

Dwg. 2618C92

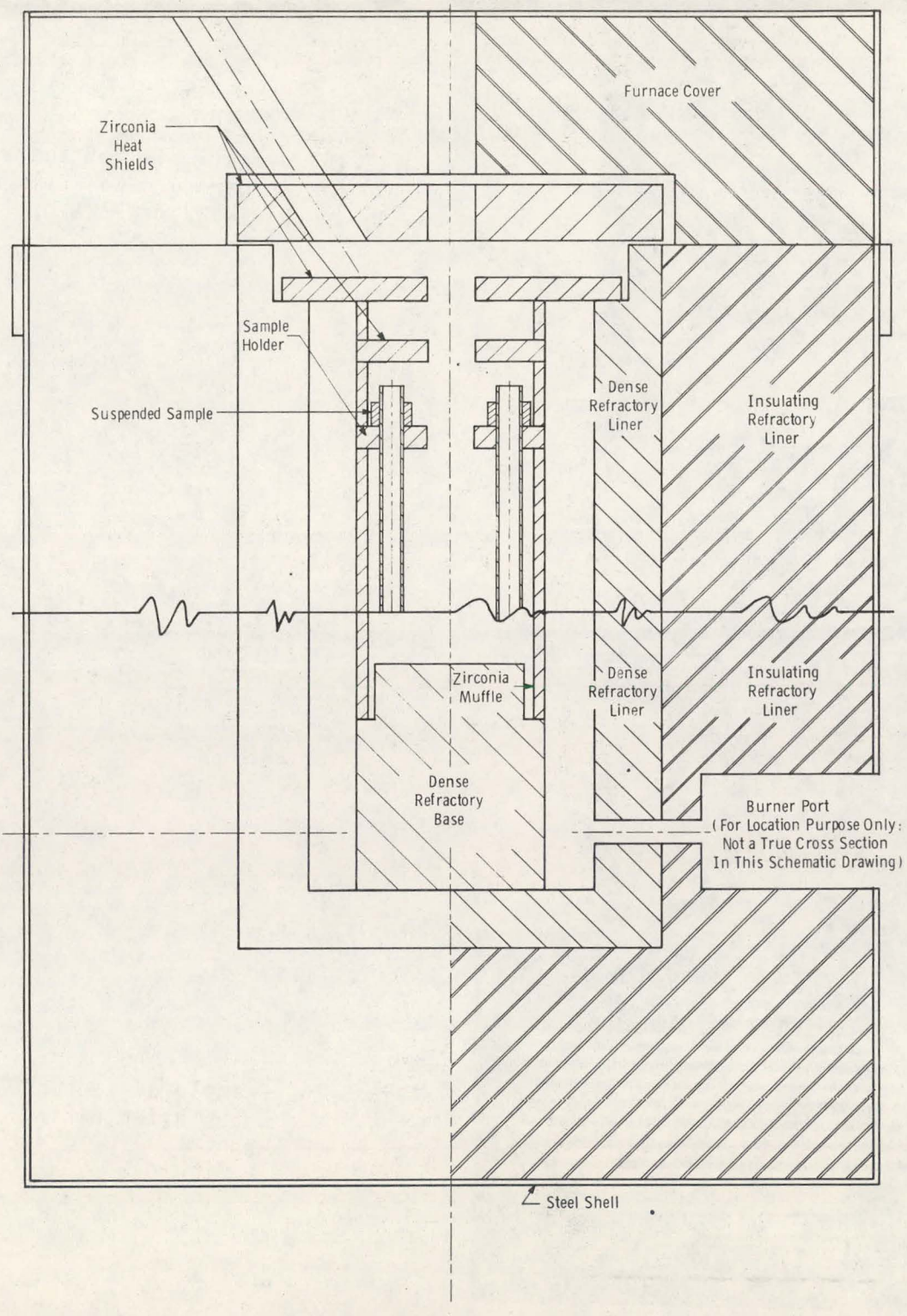

Fig. 5.13 — Schematic of samples during firing in high temperature gas kiln

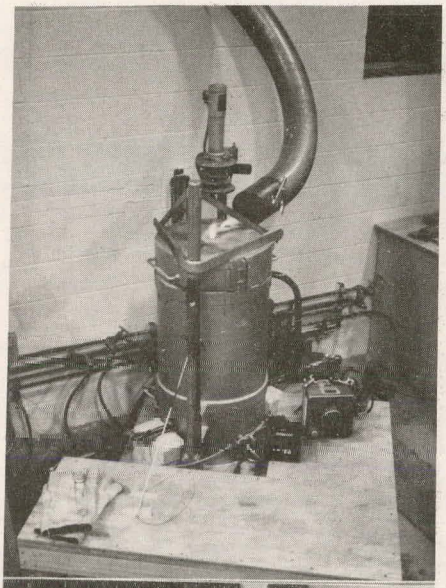

Fig. 5.14 Overall View of the High-Temperature Gas Kiln with New Working Platform

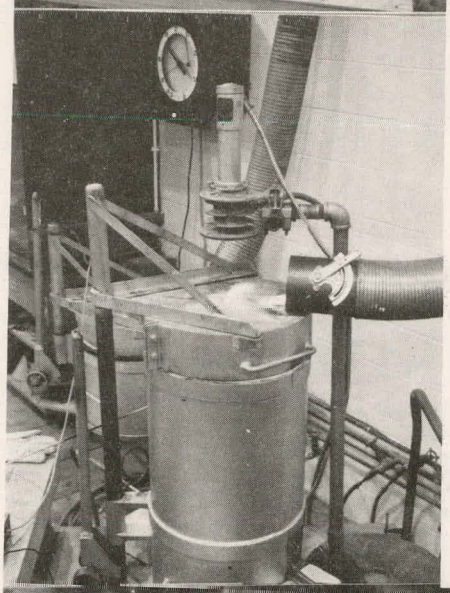

Fig. 5.15 Furnace Operating at 1950°C

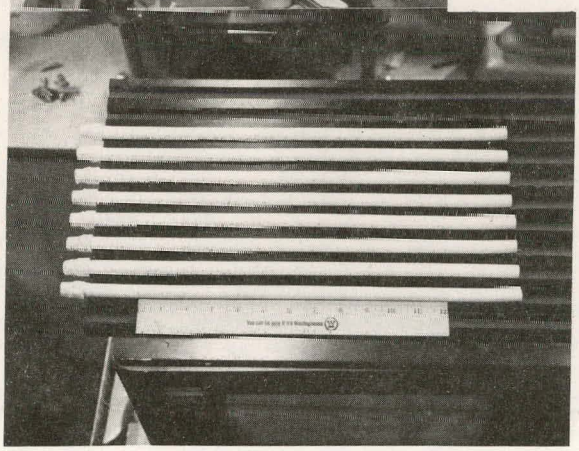

Fig. 5.16 Example of Support Tubes after Firing Run

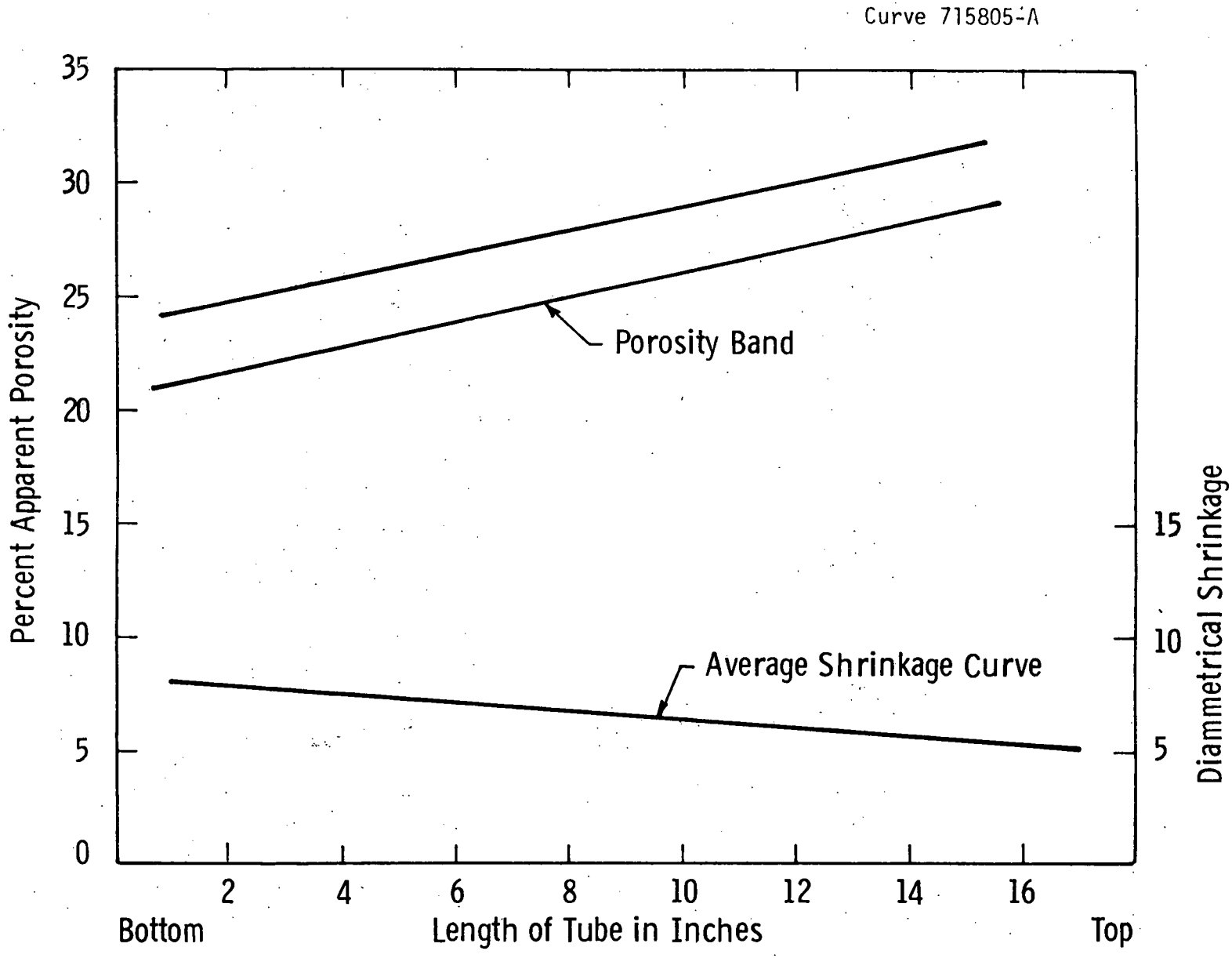

Fig. 5.17 — Apparent porosity of calcia stabilized zirconia support tubes fired (vertically) at 1800°C for 7 hours

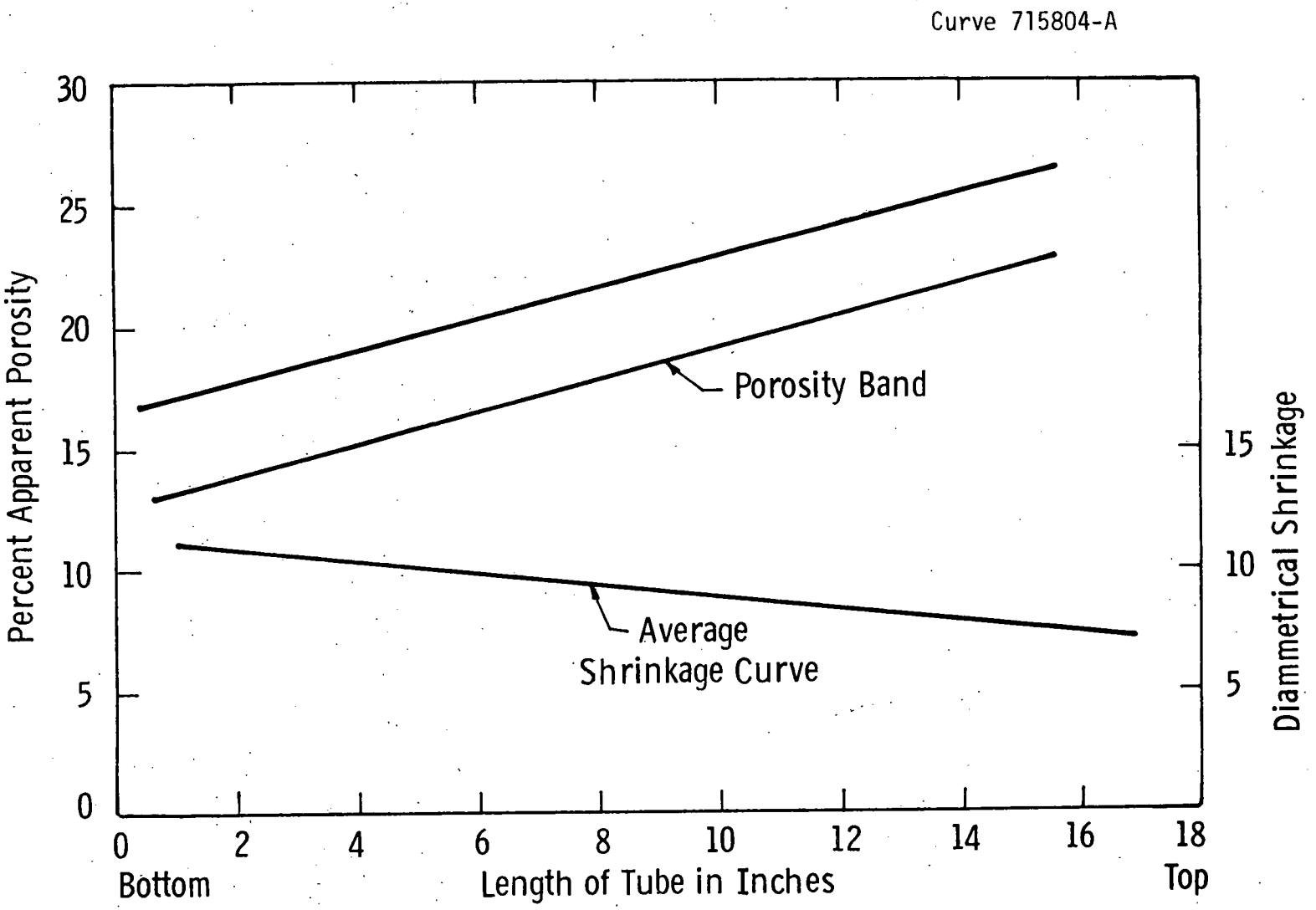

Fig. 5.18—Apparent porosity of calcia stabilized zirconia support tubes fired (vertically) at 1950°C for 7 hours.

A tabulation of the fired strengths of the porous support tubes is listed in Table 5.2. The tensile and flexural strength tests showed that the low porosity end of the tube was 1000 psi stronger than the high porosity end.

To improve the tube properties, uniformity of the temperature zone in the verticle muffle system of the high temperature gas kiln is required. Several modifications, related to geometry (concentricity) and added insulation or heat shields at the top section of the muffle system, have been implemented, to attain and maintain temperature equilibration, within the volume of the muffle system holding the support tube samples. The temperature gradient has been reduced from Δ100°C to Δ40°C by the addition of a new heat shield and a hold time of two hours at 1975°C. A longer firing schedule for a total furnace operation of 24 hours is also planned, to further refine the tube process.

TABLE 5.2 FIRED STRENGTHS OF EXTRUDED POROUS CALCIA-STABILIZED ZIRCONIA SUPPORT TUBES

Strength	Firing Condition	psi
Flexural* (3 point loading)	1950°C, ~ 7 hrs	4930
Tensile	1950°C ~ 7 hrs	3175
	1950°C ~ 4 hrs	2035
	1800°C ~ 7 hrs	1450

*Average of two samples

5.1.6 Subtask E. Fuel Cell Stack

In Section 5.1.1.3.1 we described a number of problems that were encountered during the course of stack fabrication; notably, the cracking and crumbling of the porous support tube. In this section we shall describe the fabrication of a stack that was carried through all processing steps, after all these problems had been encountered and after the problems either had been eliminated or reduced in severity.

5.1.6.1 Tube Selection

Tube deterioration was very evident in slip cast ZIRCOA tubes of 28 v/o porosity. Such a tube was selected for a stack test to demonstrate that the vapor deposition processes are now under better control.

5.1.6.2 Stack #2 Preparation

A 27 cm long porous tube was coated with a fuel electrode layer containing 60 v/o Ni and 40 v/o yttria-stabilized zirconia. The tube was rotated while intermittent sections of the fuel electrode layer were ground away with a diamond bit to create fuel electrode bands, separated by insulating bands of exposed porous support tube. Etching was not used, because our apparatus does not allow the handling of long tubes. Also, it has been found that grinding is a potentially faster and more reliable process. Furthermore, the grinding process does not depend on tube porosity, as does etching. This does not mean that etching has been abandoned as a useful method for fuel electrode band formation, but we found grinding to be an alternate that has great potential for being a practical method as well. Before the grinding, however, the tube was impregnated with calcium oxide as described in Section 5.1.1.3.1 and then exposed to the IC EVD process. The tube was rotated during the deposition, to prevent sagging in the

horizontal position. Lanthanum chromite, doped with magnesium, was deposited over the entire length as a 40 μm thick gas-tight layer. The tube was then masked with 5 mm wide tape bands, spaced 10 mm apart. The sand-blasting was used to remove the IC deposit in the unmasked areas while the tube was rotated. Following this step, grinding was employed, as mentioned above, to create insulating gaps between cells. Fig. 5.19 schematically shows the stack structure at this stage. This processing is similar to that of our first cell stack, however, the insulating gap between cells in that stack was done by sand-blasting over a denser (and, therefore, stronger) porous support tube. Applied to highly porous tubes, sand-blasting would destroy the tubes. The grinding operation creates a fuel electrode taper, as seen in Fig. 5.19, that is wider than that created by sand-blasting. This leads to an increase in short circuit currents in this area of a stack.

Electrolyte was deposited over the stack tube while the 4 mm wide IC bands were masked with 2.5 mm wide oxide masking tapes, applied in the center of the IC, so that the electrolyte overlapped the IC's and sealed the total structure. The porous layer was applied, following the electrolyte deposition, by using the new scheme described in Section (5.1.4). The stack was cut into two sections (for separate processing of both halves) and the tin doped In_2O_3-current collector was applied to one section by CVD. The air electrodes were impregnated with PrO_{2-x} and the stack was mounted for sealing and testing.

5.1.6.3 Stack #3 Preparation

A 5 cell stack (#3) was prepared, using similar techniques as described for stack #2. However, the fuel electrode was etched and the IC-layer overlapped the fuel electrode in the intercell gap as shown in Fig. 5.7 (right side). This was done to eliminate a short

Dwg. 7684A30

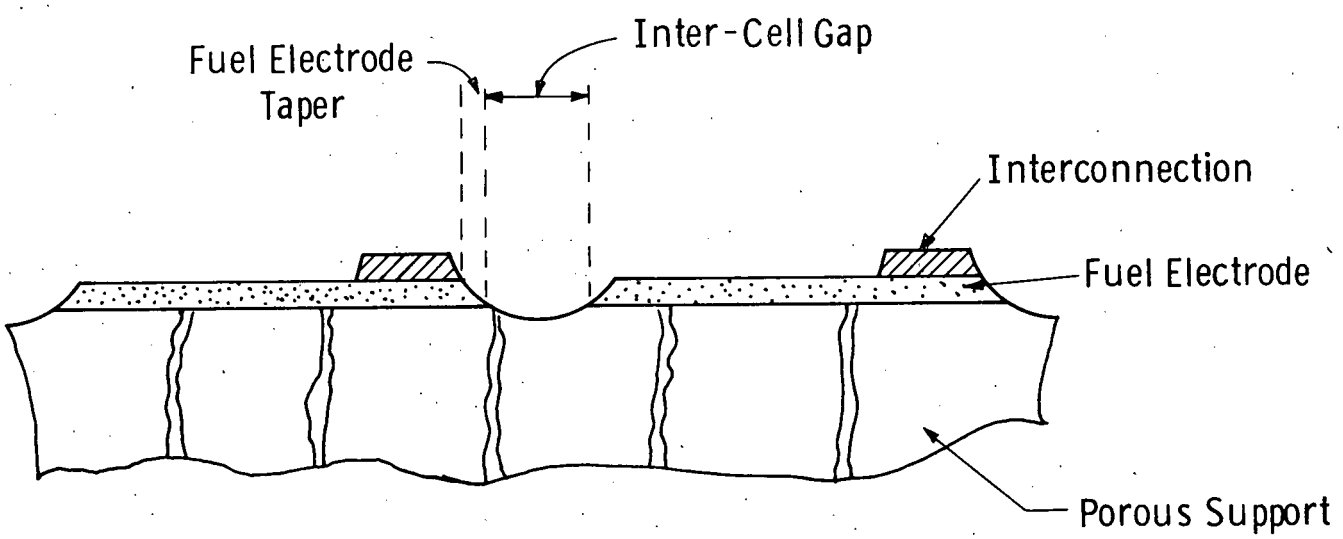

Fig. 5.19 – Stack appearance after grinding of inter-cell gap

circuit current in that particular stack section, which is caused by the exposed fuel electrode taper to the electrolyte, due to a grinding process after IC deposition.

Also the dense portion of electrolyte was applied before the IC layer and the porous electrolyte part was deposited after the removal (sand blasting) of the IC layer. Air electrode In_2O_3 current collector application and air electrode impregnation were identical to stack #2.

5.1.6.4 Stack #4 Stack Preparation

A 14 cell stack (#4) was prepared, as described for stack #3, except the porous electrolyte part of the air electrode and In_2O_3 current collector were omitted. Instead, a water slurry coating of $La_{0.9}Sr_{0.1}MnO_3$ (strontium-doped lanthanum manganite) was applied as the air electrode. This oxide contained a small amount of sintering-aid to produce a porous conducting air electrode at 1250°C. The coating thickness was nearly 100 μm thick. This oxide coating was developed as an alternate current collector material, that is not subjected to oxide reduction and will not suffer subsequent contact loss to the interconnection region. The porous air electrode was impregnated with cobalt-praesodymium oxide (active air electrode component), via the soluable mixed nitrates, which were decomposed to their oxides upon subsequent heating for stack testing.

5.2 TASK 2. LIFE TESTING OF CELL COMPONENTS AND STACKS

To enable life testing of cell components, unit cells, and cell stacks, a fuel cell life test facility was needed. The facility had to meet the following requirements:

1) be able to accept several multicell stacks
2) have a completely fail-safe gas supply system
3) have the ability to monitor several tests simultaneously and collect data automatically
4) operate reliably for extended periods with a minimum of attention.

During the first year of this continuation program, such a facility was designed and constructed in the laboratory.

5.2.1 Test Facility Design

The fuel cell test facility was designed to test up to 5 multicell stacks, simultaneously, and to provide fail-safe, dependable operation, while requiring a minimum of attention. Furnace elements were specified to operate several hundred degrees below their design temperature, to extend their life and reduce maintenance. The furnace temperature controllers are of the power proportioning type, supplying only the current necessary to maintain the set temperature. Thermocouple break protection, which prevents overheating, should a thermocouple fail, also extends furnace element life and increases reliability.

Fig. 5.20 is a schematic diagram of the gas supply system. Backup supplies have been provided to assure fail-safe operation and stack protection during power failures or loss of house-supplied gases. Under normal operation, hydrogen, nitrogen and air are obtained "in-house". Should line pressure be lost, a pressure switch activates an

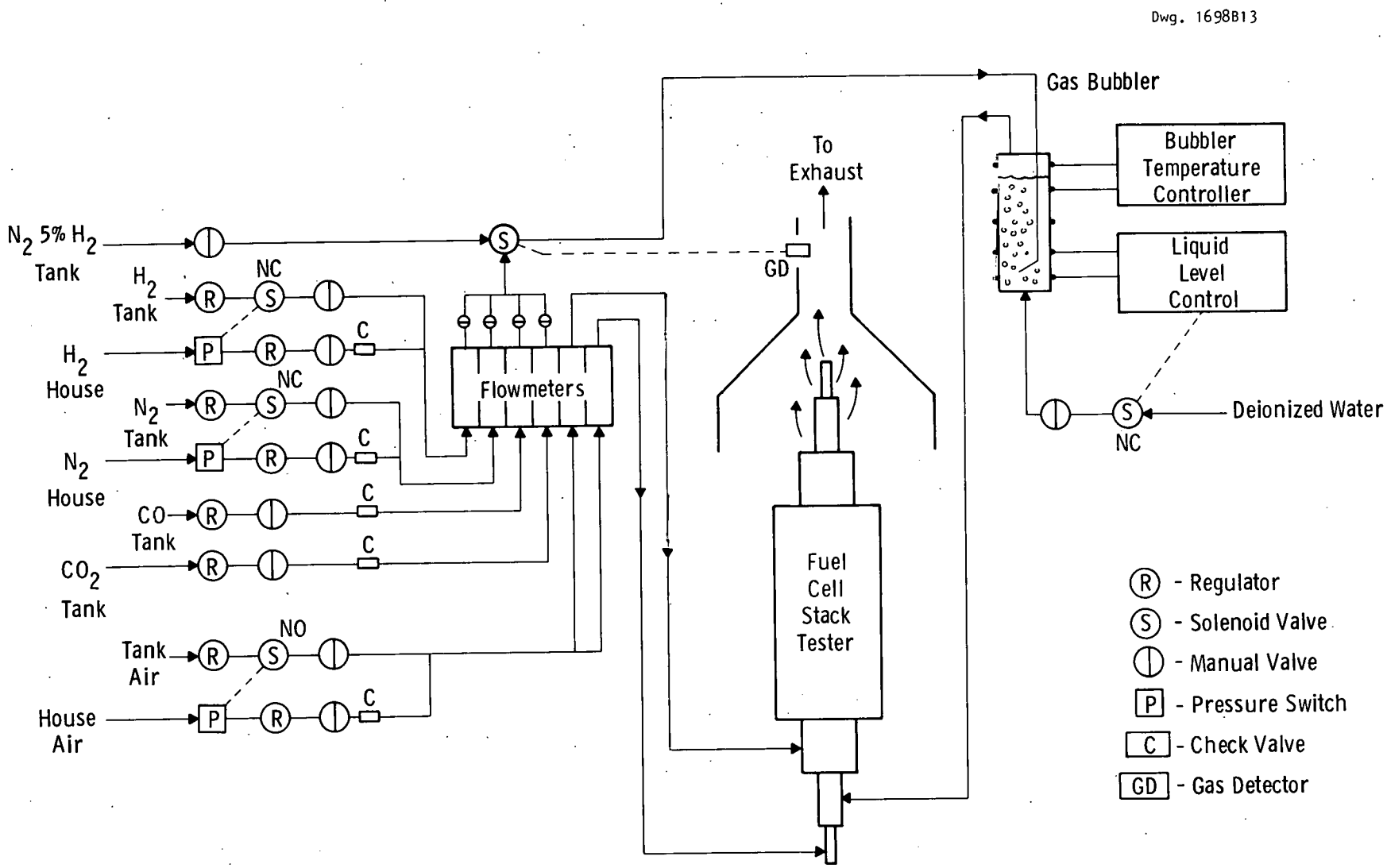

Fig. 5.20 — Schematic diagram of fail-safe gas plumbing system for test facility

electrical solenoid valve to permit backup cylinders to continue to supply the required gases. During power failures, a three-way solenoid valve fails closed, cutting off all combustible gases, and allowing a low-combustible nitrogen/5 percent hydrogen gas mixture to be supplied. This gas prevents the formation of explosive mixtures at low temperatures, until alarm systems are reset and when normal operation is restored. This same three-way valve is also wired to a combustible gas detector. The detector, mounted in the canopy hood ducting, monitors the exiting gases. As a preset percentage of the lower explosive level is approached, an audible alarm is sounded. If the situation is not corrected and gases continue to accumulate, the detector activates the three-way valve, stopping the flow of all combustible gases, and introduces the safe forming gas atmosphere, until the system is manually reset. Air, supplied by house compressors, and also lost during power failures, is protected by a fail-open solenoid valve. Again, backup air is supplied from cylinders until power is restored and normal, automatic operation is resumed.

The electrical testing of the stacks is accomplished through the use of a newly designed and constructed test device. The test panel includes the oscilloscope sync and monitor inputs, as well as a high speed, transistorized switch for increased accuracy in measuring ohmic stack losses and slow polarization losses by the current interruption technique. Also included in the panel is the stack load device. Previously the stack current density was adjusted through the use of a resistor bank. The new device accomplishes this by operating the stack as a constant current power supply. From the current density requirements, total load is calculated and set. The device will maintain this current until the stack voltage drops below a pre-set adjustable limit. At this point the instrument cuts off the load and the stack can return

to open circuit voltage. To return the stack to load conditions, the instrument must be manually reset. This feature prevents damage that would occur if, for example, a continuous load was applied to a stack that was cooling due to a furnace failure.

The actual fuel cell stack can be wired into the system in any number of ways. One possible arrangement, shown in Fig. 5.21 would have the cells wired in groups of 5. An individual cell could be left at each end of the stack and be used as an oxygen gauge to measure oxygen activity of the fuel. This would establish the maximum achievable cell stack voltage obtainable from the entering gas mixture and measure the change in the exiting fuel composition, as the fuel is depleted during stack operation. Thermocouples, placed along the length of the stack, are used for monitoring and controlling furnace temperature. Continuous monitoring and data collection is accomplished through the use of a Fluke model 2240B Data Logger. A patch panel, located at each test station, is wired into the 150 channel data logger and provides each station with 30 channels of input. Patch cords, wired to a terminal strip on the stack to be tested, can be plugged into the panel to relay the information to the data logger. Each channel on the data logger can be programmed individually to record temperatures from three types of thermocouples or voltage up to 40 volts. All information from the stack on test is scanned continuously and, at predetermined times, printed on a paper tape, and, ultimately, stored on magnetic tape. This system is also an important part of the fail-safe operation. Each channel or function monitored can have a high or low limit set point. The instrument continually scans and compares measured values to the set limits. Should either be exceeded, the time and values are recorded and an output is triggered that can be used to sound an audible alarm, open or close valves, or shut off furnaces.

Dwg. 6440A81

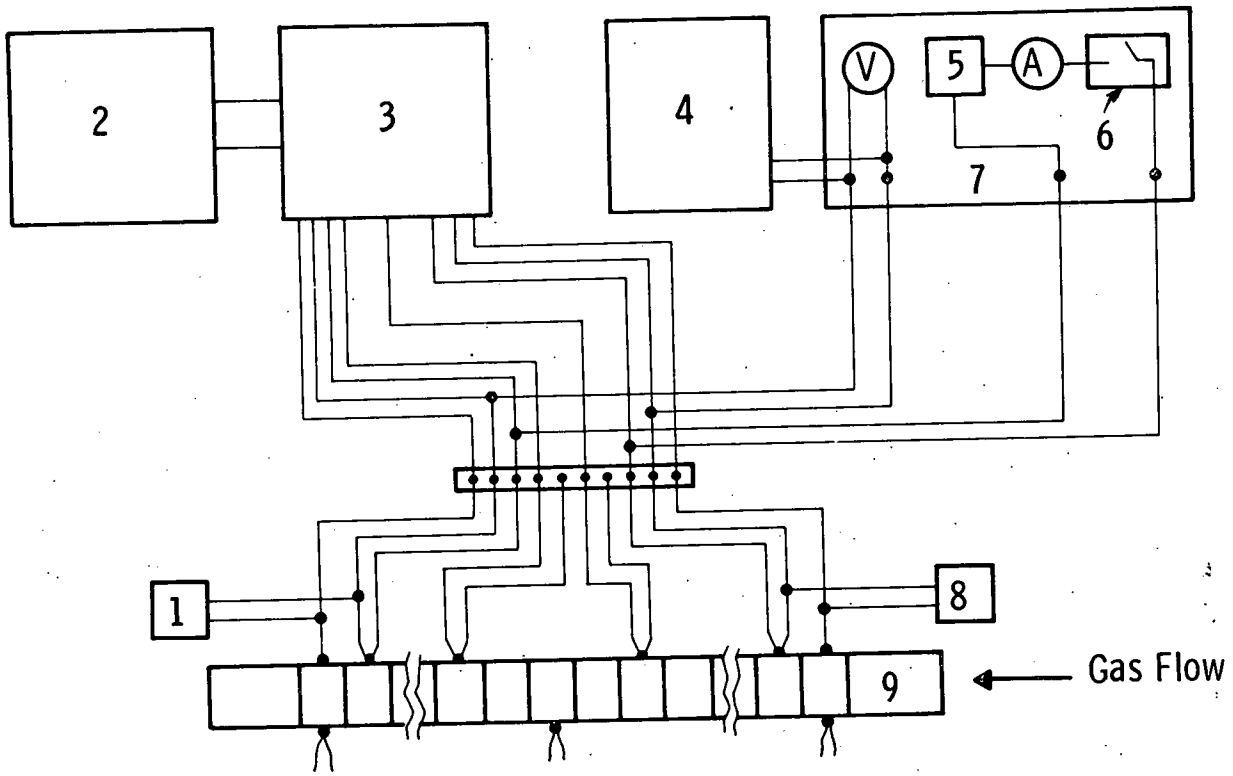

1 - Exit Gas Oxygen Gauge
2 - Magnetic Tape Recorder
3 - Data Acquisition System
4 - Oscilloscope
5 - Electronic Load Device
6 - Transistor Switch
7 - Test Station Panel
8 - Entrance Gas Oxygen Gauge
9 - Fuel Cell Stack

Fig. 5.21 —Wiring diagram for a fuel cell stack

The completed life test facility is shown in Fig. 5.22. The five test furnaces (1) can be seen on the left beneath the canopy hood (2). At the end of the bench is a white cabinet (3) which contains the combustible gas cylinders. This cabinet is ducted into the canopy hood and all exhaust is monitored by the explosive gas mixture alarm system (4). The instrument cabinets on the right contain the furnace heating controls (5), the tester panels (6), and the data acquisition system (7). All wiring is carried from the test stations to the instrument cabinets via the overhead ducting (8).

Fig. 5.23 shows, in detail, test station #1. At the bottom left are the gas flow meters (1). Directly above them are the temperature controller (2) and level controller (3) for the water bubbler (4) located to their right. At the center of the photograph can be seen the patch panel (5) that is wired to the data acquisition system. It's into these panels that all stacks must be wired.

Fig. 5.24 is a frontal view of four of the five test stations and Fig. 5.25 is a rear view. In this rear view the gas supply regulators (1) can be seen at the far left center. Gas is supplied to each set of flow meters through the seven parallel pipes (2) attached to the bottom of the support frame. Beneath the gas lines is the electrical conduit (3) that supplies power to the water bubbler temperature and level controllers, and also to all of the gas solenoid valves. All instrument wiring is carried from the patch panels (4) via conduit to the larger (5) of the two square ducts near the top of the photo. The wiring is then routed overhead to the data acquisition system. The smaller duct (6) carries power to the furnaces from the control panels and is isolated from the instrument wiring to prevent interferences. At the center of the photo, near the top of the support frame, is the deionized water supply (7) for the bubblers. A small flow of water is

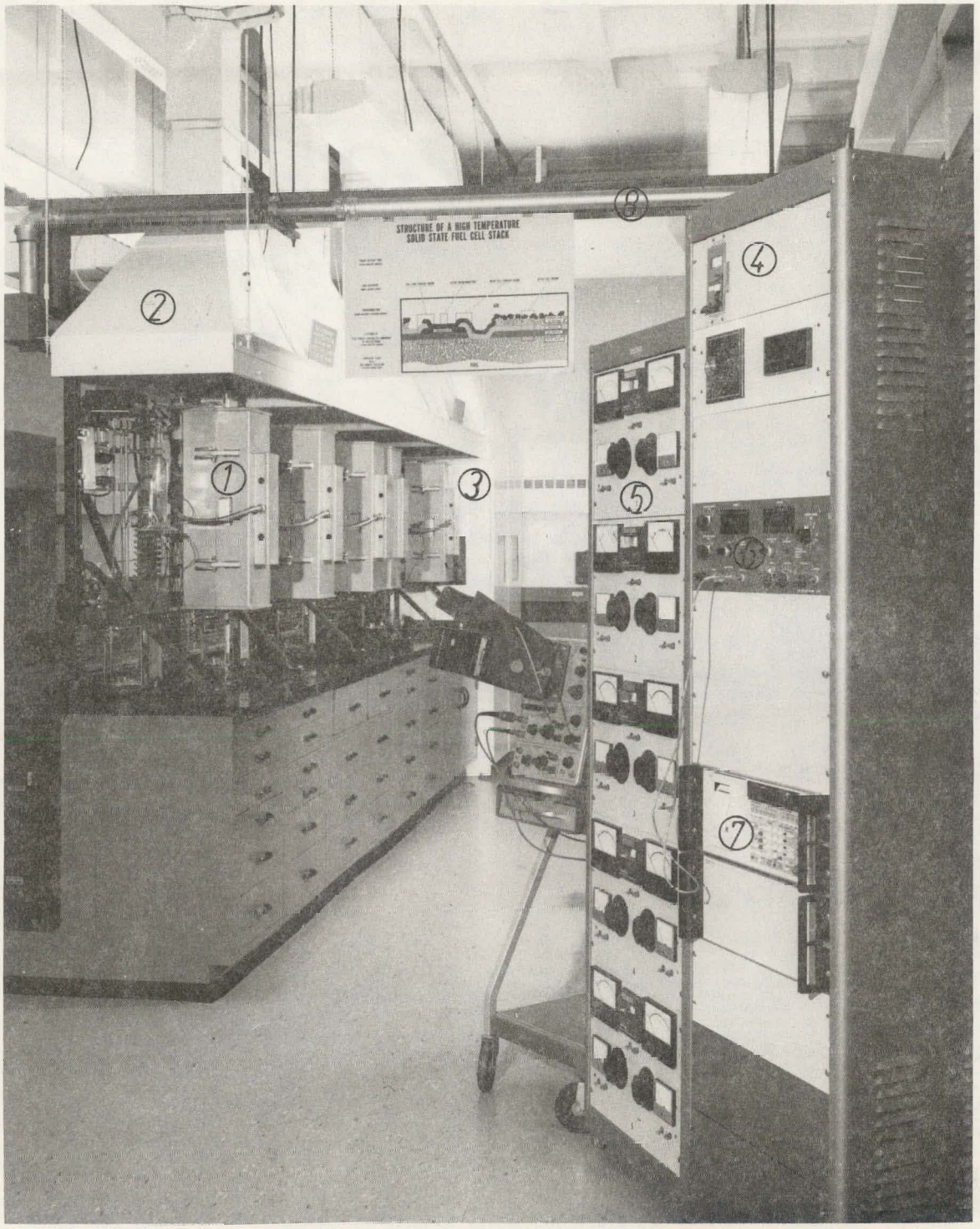

Fig. 5.22 General View of 5-Station HTSOE Fuel Cell Life Test Facility (Left) and Control and Data Acquisition System (Right)

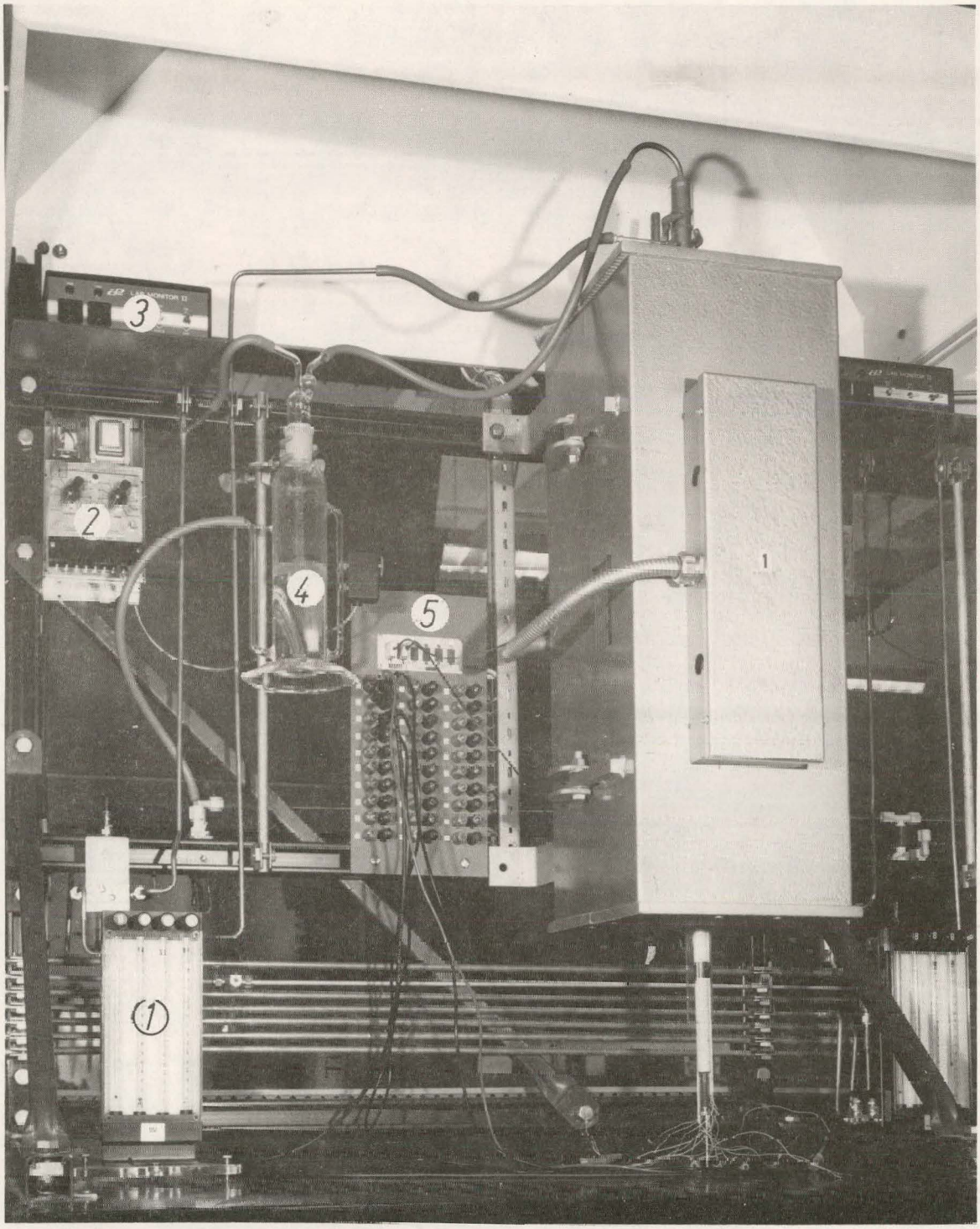

Fig. 5.23 Detailed View of HTSOE Fuel Cell Test Station #1 Showing Furnace. Flow Meters (1), Water Bubbler (4), Bubbler Temperature (3) and Level (2) Controls and Patch Panel (5)

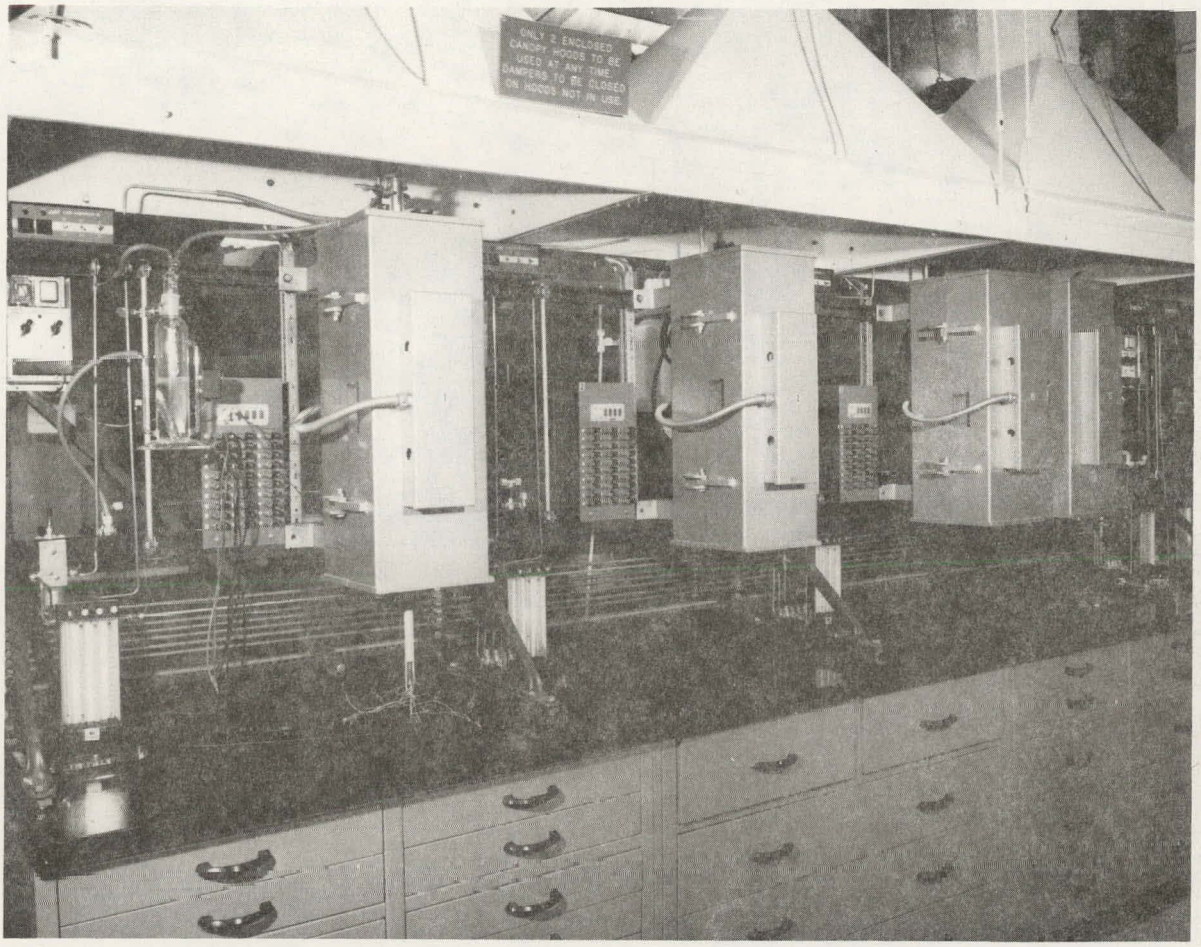

Fig. 5.24 A Front View Showing Four of the Five HTSOE Fuel Cell Test Stations

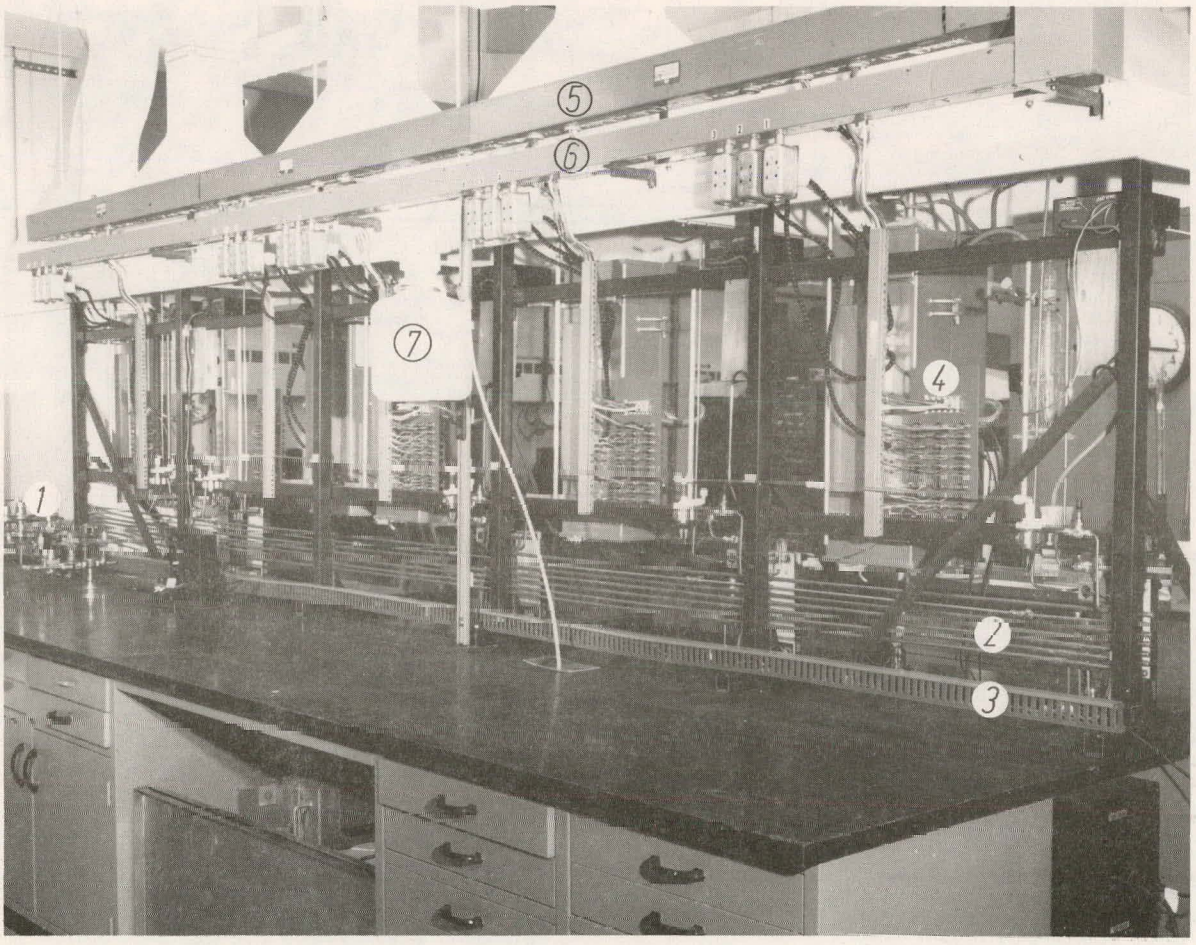

Fig. 5.25 A Rear View Showing Details of Gas Supply Lines (2), Wiring Conduits (3), and Water Supply System (7)

continually supplied and allowed to overflow to maintain a constant level. Water is carried from this reservoir via plastic tubing to each of the five stations. This water supply system is so designed that, if there is a failure in both the automatic level controller and its corresponding solenoid valve, the water bubbler would not overfill. This design prevents water from ever being injected into a hot fuel cell stack.

5.2.1.1 Summary

The five station fuel cell life test facility is complete and operational under fail-safe conditions. All gas supplies, both primary and backup, that were plumbed in, have been leaked checked, and tested for fail-safe operation. Furnace heating controls have been calibrated and tested. Installation, calibration, and testing of the explosive gas alarm system has been completed and the alarm system has been wired into the data logger for monitoring. All test station patch panels have been wired into the data acquisition system and have been programmed to record the proper values. The facility is presently being used to test fuel cell stacks.

5.2.2 Task 3, Subtask A. Interconnection Testing in a Dual Atmosphere

The goal of this task is life and life performance predictions of the interconnection, while in contact with the air and fuel electrode, as required in the fabricated fuel cell.

5.2.2.1 Resistance Measurement Technique for Interconnection Testing in a Dual Atmosphere

Some essential requirements for these measurements are as follows:

1) Interconnection (IC) film resistance should be measurable for IC resistivities as low as 0.3 ohm-cm. The current flow must be through the film; i.e., perpendicular to the film plane, as it will occur in an actual cell.
2) Measurements should be possible on two-component (fuel electrode, interconnection) or three-component (fuel electrode, interconnection, air electrode) specimens. This will permit the evaluation of individual fuel and air electrode interface resistances if they are significant.
3) Specialized fabrication of the fuel electrode, interconnection, and air electrode for the test specimens should be kept to a minimum. This will ensure that the test specimen components are typical of those in an actual fuel cell and, in addition, will reduce specimen preparation time.

The first two requirements are met quite well by the crossed-electrode technique developed earlier in this program. Unfortunately, this technique fails to meet the important third requirement.

A measurement technique that will satisfy all three requirements is the multi-surface-electrode method, used previously (see Section 5.2.3.1.2 for evaluation of IC EVD film resistances). However, three refinements are necessary. These are: (1) small area surface electrodes (1 mm diameter); (2) separate current and potential leads to the electrodes; and (3) spring-loaded contacts to the surface electrodes.

There are additional benefits from this measurement technique.

1) Many electrodes can be placed on a single, tubular specimen. This permits duplication of measurements, resistivity profiling along the tube, or two- and three-component measurements on a single specimen.
2) The sheet resistivity of the fuel electrode is easily measureable with four surface electrodes, even on two- or three-component specimens.
3) It is possible (but not recommended) to perform the IC measurements on an operating fuel cell.

5.2.3 Subtask B. Fuel Electrode-Interconnection Interaction

The purpose of this task is to study and understand occurrences at the fuel electrode-interconnection interface at high temperatures.

5.2.3.1 Electrical Resistance of Recent EVD-Deposited Interconnection (IC) Films

In early EVD-deposited interconnection films (Final Report, March 31, 1978) it was found that a high resistance interfacial layer was present adjacent to the fuel electrode. This was ascribed to a deviation from the desired composition, occurring only in the initial phase of EVD interconnection film growth.

Since then, important modifications have been made in the EVD process, so that it was possible to produce a successful, operating multi-cell stack. This was described in the above report. Nevertheless it was considered desirable to recheck the resistance characteristics of a prepared EVD interconnection film, especially with regard to interfacial resistance.

5.2.3.1.1 Specimen Preparation and Measurement

A combination specimen was prepared just as a fuel cell would be, starting with a porous calcia-stabilized zirconia support tube, covered by a nickel-cermet fuel electrode layer. On this was deposited, by EVD, a 40 μm thick layer of magnesium-doped lanthanum chromite. Three platinum electrodes (8.8 mm x 1.6 mm x 4 μm) were then added to the chromite surface by RF sputtering (electrodes A, B, C) and the chromite was removed at one end of the specimen to expose the nickel-cermet substrate (electrode N). Fig. 5.26 shows a schematic cross-section of the specimen and electrodes. After attaching suitable leads to the specimen it was placed in the resistance measurement furnace and enveloped with a flowing hydrogen-water atmosphere. Specimen resistances R_{AB}, R_{BC}, R_{AN}, R_{BN} and R_{CN}* were measured over the temperature range of 60 to 1000°C. The standard precautions of polarity reversal (for cancellation of thermal E.M.F.'s) and lead resistance corrections were employed.

5.2.3.1.2 Determination of Interfacial Resistance

In a previous report, a method was described for determining both the bulk resistivity and interfacial resistance of an interconnection film, provided that the latter resistance is sufficiently large. Briefly, it is based on the fact that in a combination IC specimen, the current flow between two surface contacts has a lateral component which is enhanced when an appreciable interfacial resistance is present. This is pictured in Figs. 5.26 and 5.27. It can be shown that when the interfacial resistance is absent or small

$$R_{AB} = R_{AN} + R_{BN} \qquad (1)$$

*Subscripts refer to the electrodes used in measuring the resistance.

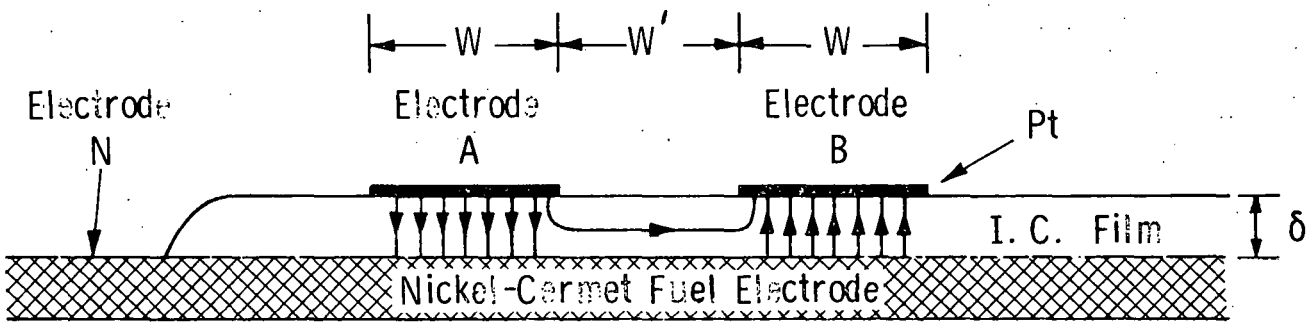

Fig. 5.26—Cross-sectional view of ideal combination specimen consisting of fuel electrodes, interconnection film, and platinum electrodes for resistance measurements. Arrows indicate the current flow pattern within the I. C. film. Electrode C, omitted for clarity, would be located to the right of electrode B

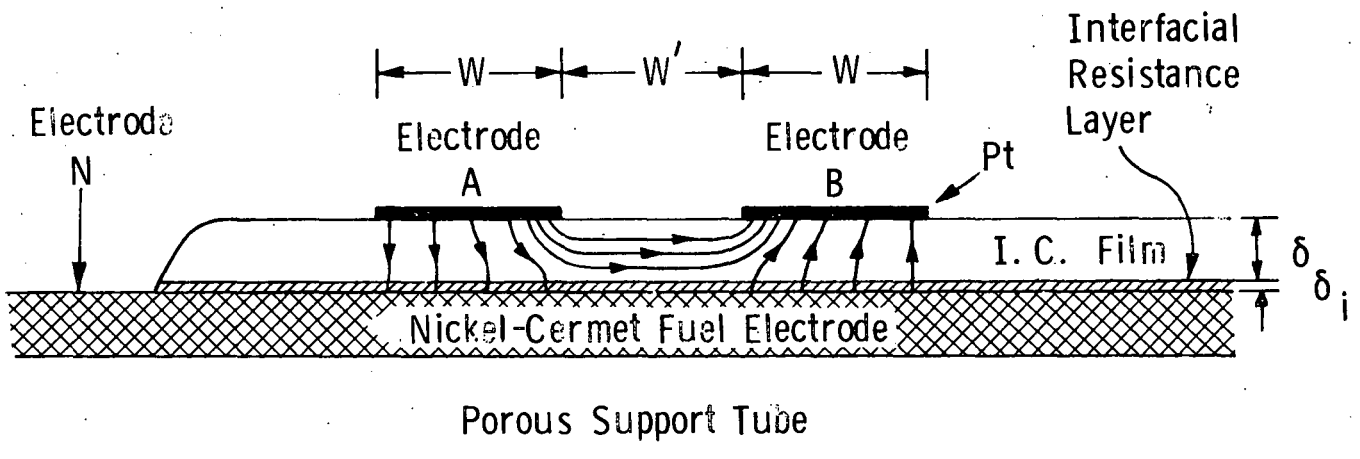

Fig. 5.27—Cross-sectional view of combination specimen having an interfacial resistance layer at the fuel electrode-interconnection film boundary. Arrows indicate the current flow pattern within the I. C. and interfacial resistance layer.

whereas, when a large interfacial resistance is present,

$$R_{AB} < R_{AN} + R_{BN} \qquad (2)$$

Similar relationships hold for R_{BC}.

From precise measurements of R_{AB}, R_{AN} and R_{BN}, the IC bulk resistance and the interfacial resistance may be calculated, using equations presented in the previously mentioned report.

5.2.3.1.3 Results and Discussions

Resistance data for the present specimen satisfied Equation (1) within the limits of experimental accuracy; from this it was estimated that the interfacial resistance (if present) was not appreciably larger than the bulk resistance of the specimen. In contrast to this, the interfacial resistance in early EVD-deposited IC films was hundreds of times larger than the bulk resistance.

Irrespective of the presence or absence of interfacial resistance, it is always possible to use the data to calculate an apparent resistivity for the IC film, This is presented in Fig. 5.28 for temperatures between 600 and 1000°C where good equilibrium with the hydrogen-water atmosphere was obtained. The apparent resistivity at 1000°C was about 30 ohm-cm, which is a factor of 10 higher than our best values obtained on sputtered films of similar IC material. This higher value may be due to non-optimum doping and, possibly, some interfacial resistance. It was observed that the sequence of electrodes A, B, and C showed improving resistivities (lower) as one proceeded away from the edge of the EVD-deposited IC film. This suggests that the resistance-profiling of an entire specimen tube might provide valuable information for further improvement of EVD-deposited interconnection films.

Curve 714513-A

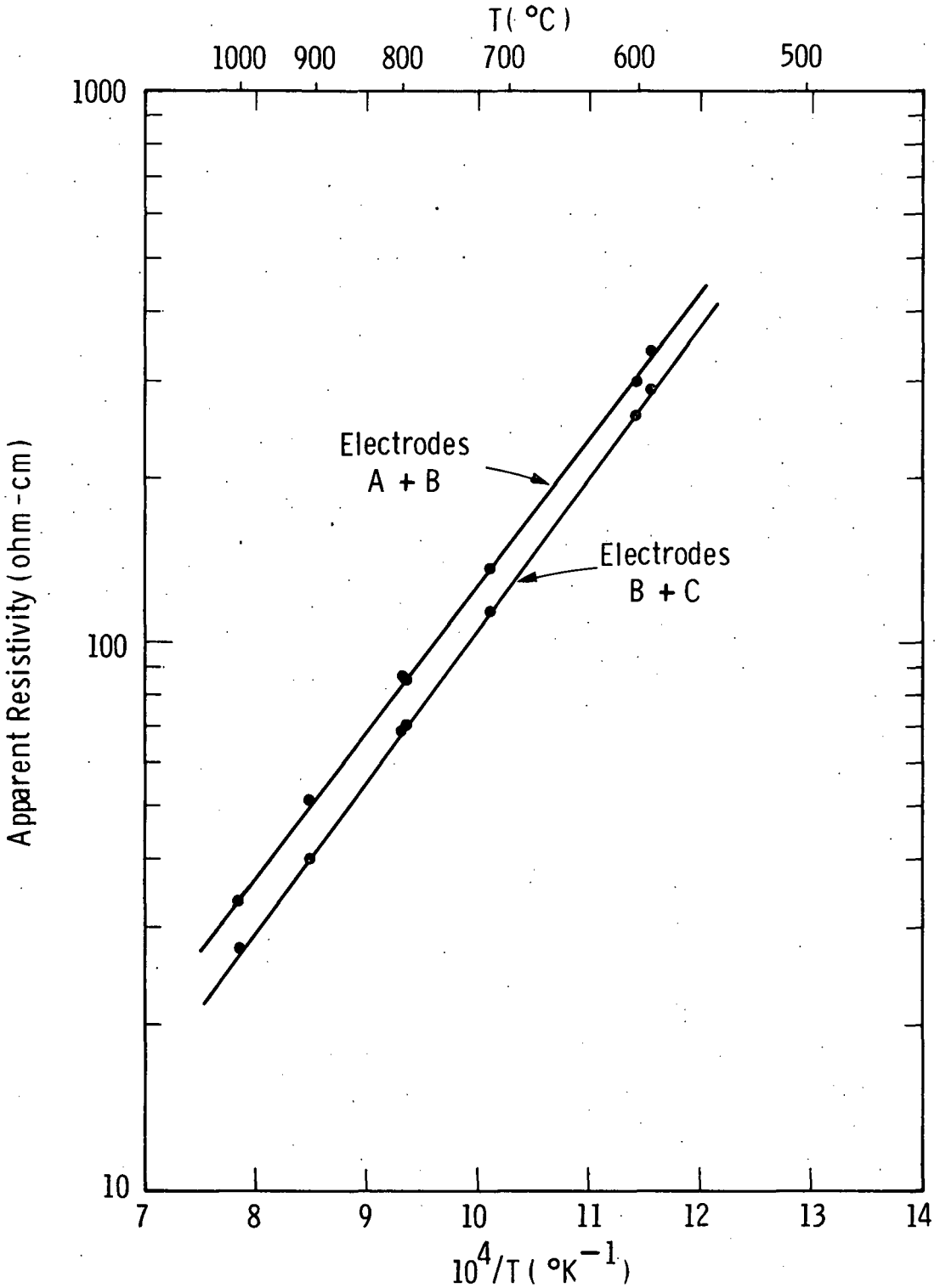

Fig.5.28—Apparent resistivity vs temperature for a recent EVD-deposited interconnection film (magnesium-doped lanthanum chromite). Values were calculated for contact pairs from R_{AB} and R_{BC} (see text)

5.2.4 Subtask C. Air Electrode-Interconnection Interaction

The previous DOE program[1] on the HTSOE fuel cell resulted in the identification, fabrication and testing of a five cell stack containing a new interconnection material, lanthanum chromite doped with magnesia and alumina. Our present continuation program sets goals of improved stack performance on twenty cell stacks using this interconnection material.

From the earlier work it was recognized that a major improvement in stack performance could be attained by reducing ohmic resistance losses in the interconnection section, particularly at the lanthanum chromite/air electrode interface, where flaking of the indium oxide air electrode collector occurred during the first 100 hours of operation.

One of the prime goals of our current investigations is to eliminate this effect, which we attribute to insufficient permeation of oxygen through the In_2O_3 layer, to its interface with the lanthanum chromite interconnection, as explained in Section 5.1.3.1.

Therefore, work on the air electrode-interconnection interaction focused on several areas:

1) enhancing the availability of $O^=$ to the air electrode interconnection interface
2) determining the effects of the exposure of lanthanum chromite to either air or hydrogen-water atmospheres at 1000°C
3) determining the high temperature electrical resistivity of tin-doped indium oxide as a function of oxygen partial pressure

In exploring these 3 major areas, 7 separate studies have been conducted; either in work on the lanthanum chromite or on the air

electrode current collector or in fabricating fuel cell stacks: (1) alternate doping agents and different amounts of doping in the indium oxide to increase oxygen permeability; (2) oxygen composition changes in lanthanum chromite (which affect the oxygen permeability) as related to the degree of doping, the oxygen partial pressure and the temperature; (3) chemical stoichiometry and stability of the EVD films, as compared with thermodynamically-stable bulk form of lanthanum chromite; (4) alternate air electrode materials to serve as interface layers or as the entire air electrode (which may improve access of oxygen to the interconnection interface and, perhaps, reduce the materials cost of the air electrode); (5) use of low melting (e.g., 1000-1350°C) second phase additives to bond air electrode powder particles to each other and to the interconnection interface (to provide an air electrode layer with improved permeability for air); (6) alternate methods for improving mechanical porosity of air electrodes formed by chemical vapor deposition and (7) studying the electrical resistivity of tin-doped indium oxide as a function of oxygen partial pressure.

5.2.4.1 Alternate Doping Agents for Indium Oxide

Indium oxide, containing two to four atomic percent tin, is the major chemical component of the air electrode of the HTSOE fuel cell. A 20 to 40 micron thick layer of magnesium-doped lanthanum chromite is sandwiched between an extension of both the indium oxide and the nickel fuel electrode layers to provide a series connection of adjacent cells of the fuel cell stack. A physical barrier, preventing direct reaction of the fuel with oxygen (from the air) at the cathode, is also maintained.

Of the three layers comprising the electrical junction, the lanthanum chromite is ideally non-permeable to oxygen while the indium oxide and nickel layers are actually physically porous.

In fact, however, a small solid state permeability to oxygen exists, via vacant oxygen sites in the crystalline lattice of the lanthanum chromite. This permeability is accentuated by low oxygen partial pressures and the presence of the magnesium-doping component that is used to enhance the electronic conductivity. Actually, this permeability by solid state diffusion is small and should present no problem, unless oxygen access to the interface through the indium oxide layer is restricted. In this restricted case indium oxide itself becomes a parasitic source of part of the oxygen that diffuses through the lanthanum chromite to the fuel side of the interconnection. In this situation it is possible, due to the oxygen depletion, to form volatile In_2O and SnO species, which may result in separation and spalling of the indium oxide layer. If some hydrogen could permeate the lanthanum chromite, a similar problem would arise with the additional formation of an H_2O species. Sufficient physical porosity of the indium oxide would obviate either difficulty. Therefore, we are examining methods to increase the physical porosity and solid state permeability to oxygen of the indium oxide.

Our data show that indium oxide, in which about two atomic percent of the indium is replaced by tin, loses a small quantity of oxygen when the oxygen partial pressure is reduced. The effect is reversible for equilibration times of a few hours and oxygen pressures of 10^{-4} atm, and higher. At low pressures (e.g., 10^{-12} atm) irreversible losses were observed in controlled atmosphere microweighing experiments. Thermodynamic data of others[2] suggest that the irreversible losses may be due to vaporization of In_2O, SnO, and In, in particular, depending on the oxygen partial pressure and temperature involved.

In our current studies we have examined the effect on the oxygen content of indium oxide of additions of other dopants, including zirconium, titanium, niobium and tantalum.

Fig. 5.29 shows a comparison of the oxygen loss from $In_{1.84}Sn_{.16}O_{3\pm x}$, $In_{1.96}Sn_{.04}O_{3\pm x}$, and pure In_2O_3. It is seen that the oxygen loss is greater at the higher doping level but not proportional to the tin content. In contrast to the doped specimens, oxygen loss from the pure indium oxide is negligible below 10^{-2} atmospheres. This behavior suggests that perhaps interstitial oxygen or metal ions are involved. The explanation is plausible from a consideration of the crystal structure, which is C-type rare earth. This can be considered as a distortion of the fluorite structure in which oxygen ions are arranged in simple cubic packing with alternate interstitial positions filled with cations. There is also an ordered removal of two of every eight oxygen ions in the simple cubic packing of the oxygen ions of the crystal. Thus one-fourth of the potential oxygen sites, and one-half of the sites coordinated to eight oxygen ions which are potential metal ion sites, are available as interstitial sites.

It is assumed that tin enters the lattice, at least partially, as a nominal Sn^{4+} species. This would suggest that other species, such as Zr^{4+}, Ti^{4+}, Nb^{5+}, Ta^{5+} may also dope indium oxide in a similar manner. Figs. 5.30 and 5.31 are plots analogous to Fig. 5.29 which show that for $In_{1.96}Zr_{.04}O_{3\pm x}$ and $In_{1.98}Ta_{.02}O_{3\pm x}$, the oxygen loss dependence on oxygen partial pressure is similar in nature and magnitude to that of the tin-doped system.

As with pure and tin-doped indium oxides, exposure to very low oxygen partial pressures, such as 10^{-14} atmospheres (provided by a water/hydrogen mixture) resulted in irreversible weight losses. No irreversible weight losses were observed in our experiments in atmospheres containing one to 100 percent oxygen. This behavior is anticipated from thermodynamic considerations. However, the oxygen loss dependence on oxygen partial pressure is not suggested by a simple mechanism, and this problem is being considered further.

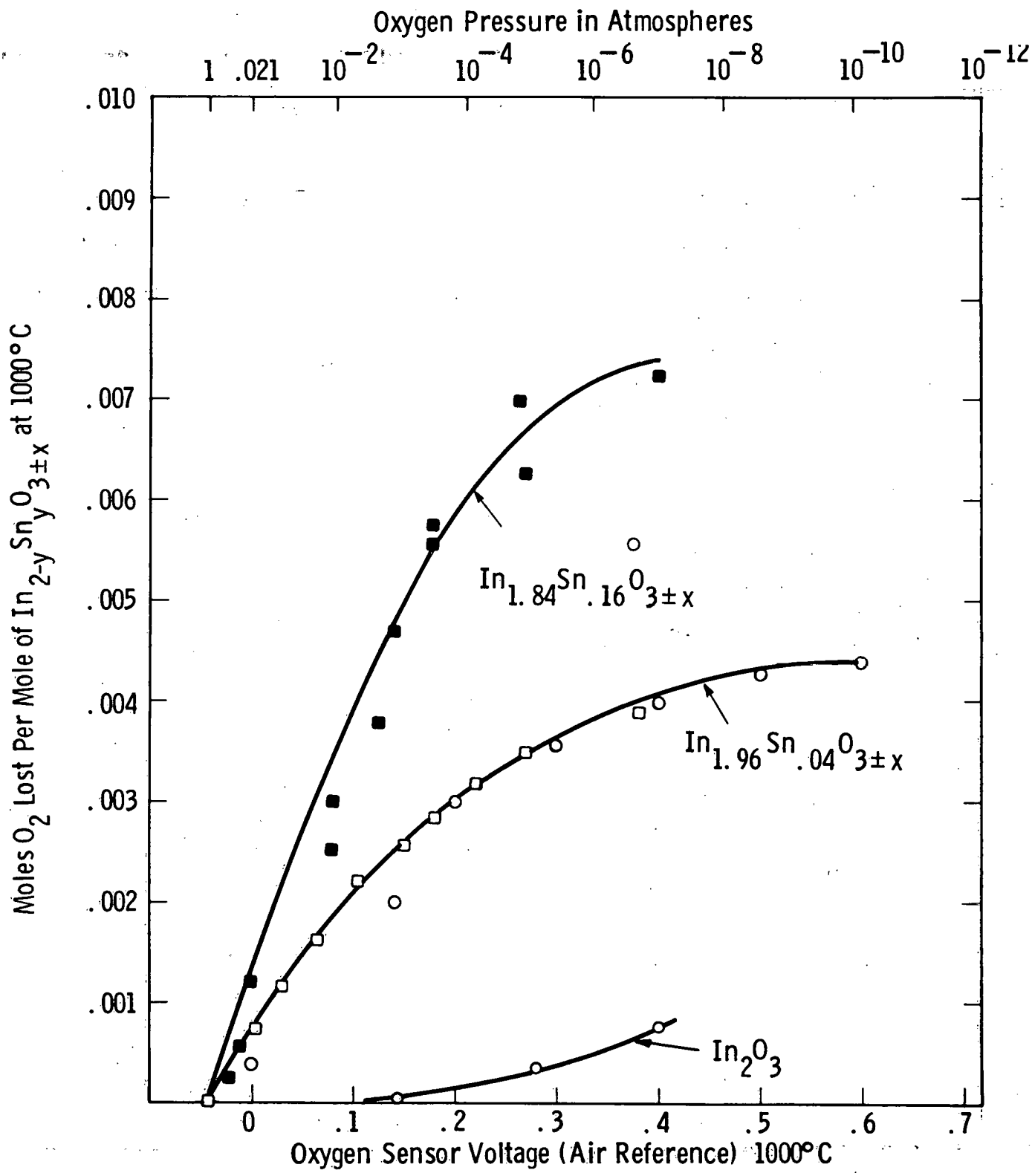

Fig. 5.29 —Oxygen loss from $In_{2-y}Sn_yO_{3\pm x}$ vs oxygen partial pressure

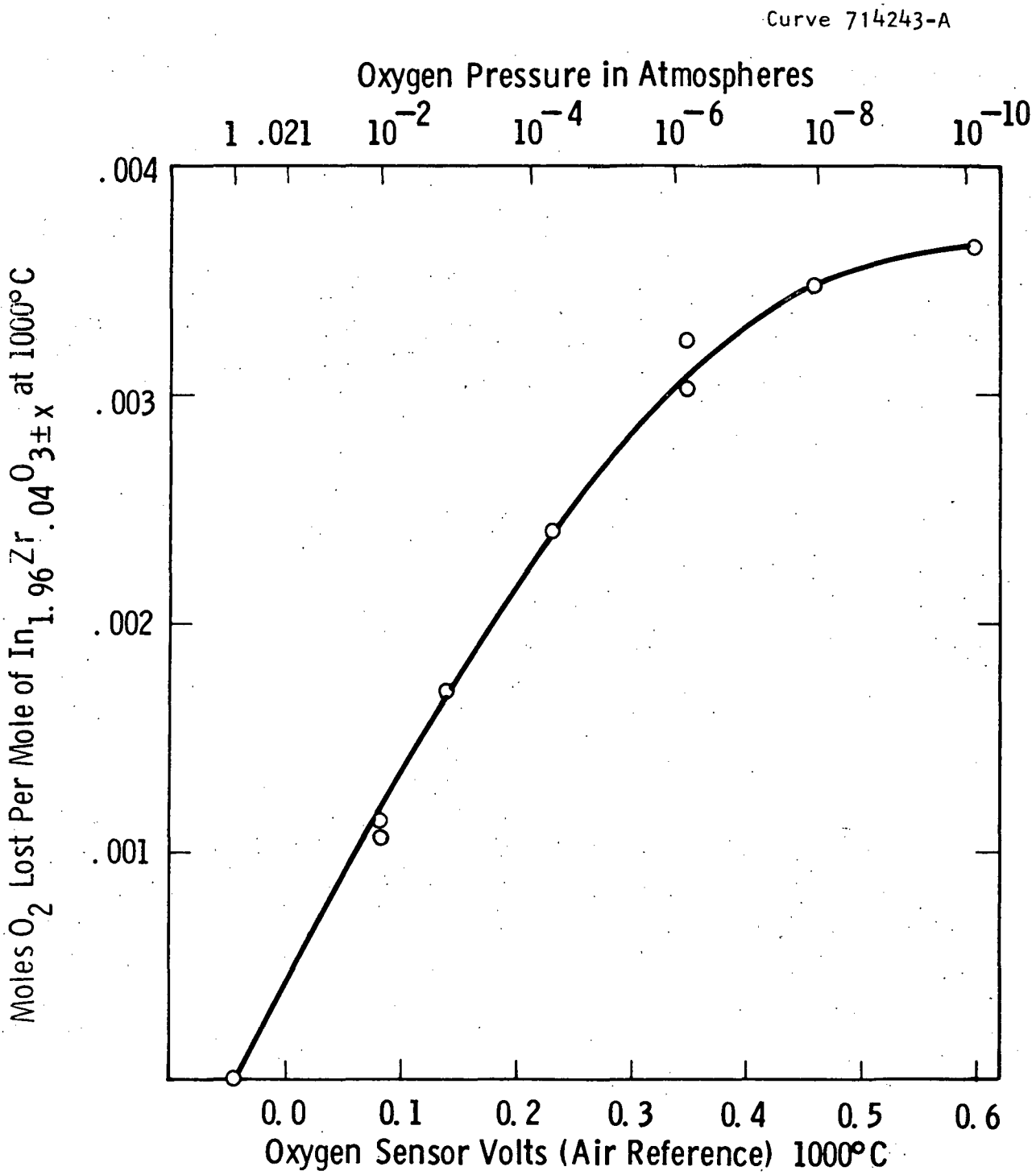

Fig. 5.30 – Oxygen loss from $In_{1.96}Zr_{.04}O_{3\pm x}$ vs oxygen partial pressure

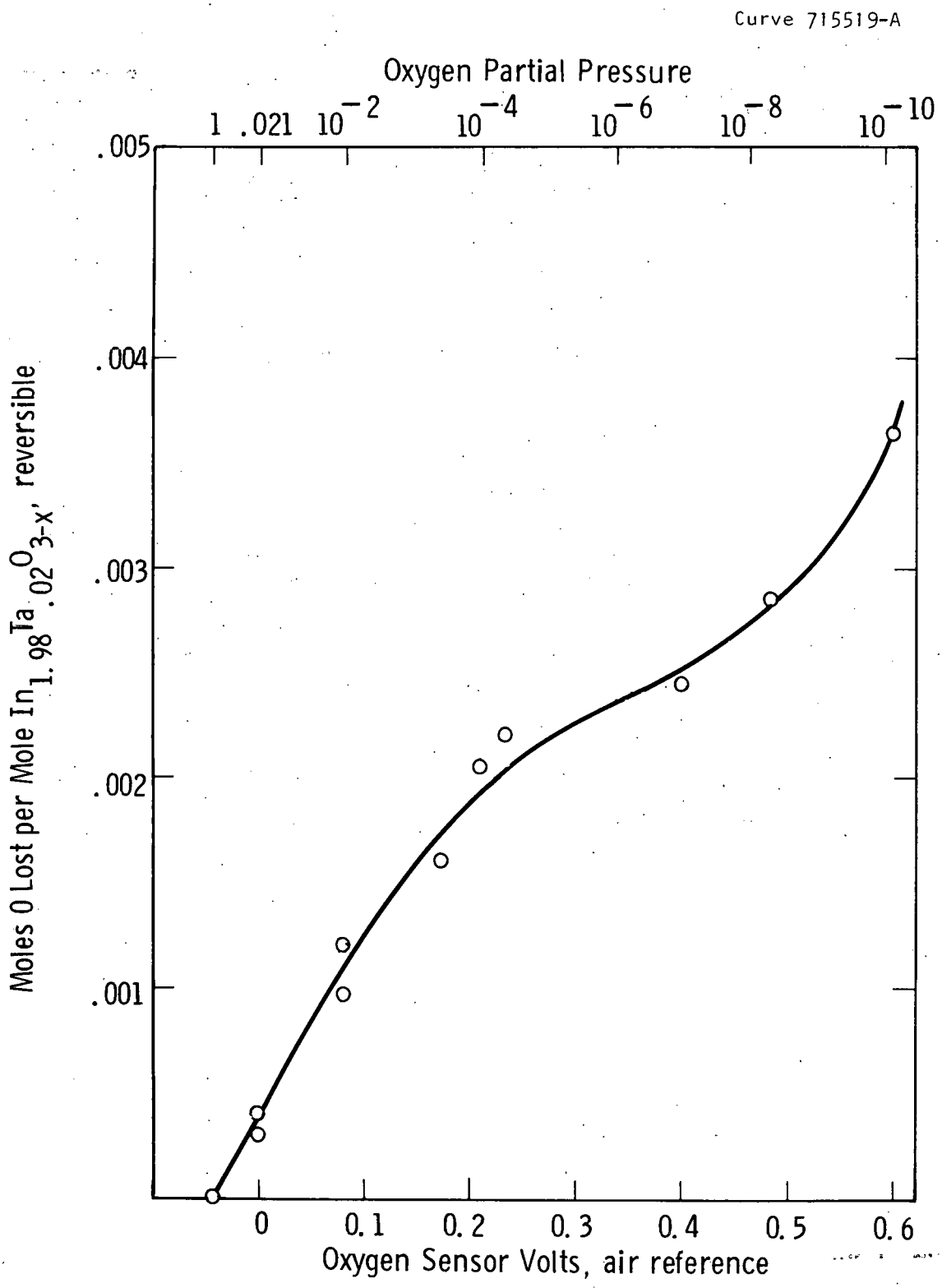

Fig. 5.31 — Oxygen loss from $In_{1.98}Ta_{.02}O_{3\pm x}$ vs oxygen partial pressure

Electrical conductivity studies by others[7] suggest that the major effect of doping indium oxide with higher valence ions of tin, zirconium, etc., is to produce electronic charge carriers. Our current work suggests that the number of electronic charge carriers increases as the oxygen pressure is decreased. This effect is discussed in Section 5.2.4.4.

Overall, the data suggest that no large improvement in oxygen permeation of indium oxide is likely, due to simple doping by different chemical species, other than tin.

5.2.4.2 Oxygen Loss from Lanthanum Chromite Interconnection

To assist in obtaining a better understanding of the lanthanum chromite/air electrode interface interaction, a study was conducted on the oxygen loss from lanthanum chromite at elevated temperatures.

In its pure form, lanthanum chromite has a very low diffusion coefficient for oxygen. It apparently also has a low oxygen vacancy content, which changes less than one part in ten thousand for samples pretreated at 1700°C and then heated at 1000°C over a pressure range from 0.21 to 10^{-16} atm of oxygen, as indicated by our high temperature microweighing experiments.

If we add magnesium (or other alkaline earth ion) to increase the electrical conductivity of lanthanum chromite, a different behavior occurs. Near operating temperatures of the fuel cell (1000°C), the oxygen content of the doped lanthanum chromite changes, from essentially the theoretical maximum in air to a small deficit at low oxygen partial pressures. According to H. Anderson,[8] and in agreement with our earlier assumptions,[1] the maximum loss from the magnesium-doped compositions approximates one mole of oxygen per two moles Mg^{2+} in solid

solution. Fig. 5.32 is an example of the oxygen deficiency as a function of oxygen partial pressure at 1000°C, as analyzed by the high temperature microweighing technique described in a previous report.[1] The oxygen loss decreases as the magnesium doping decreases. In practice this suggests that insufficient access of oxygen to the lanthanum chromite interface with indium oxide can result in a deficit of oxygen, which implies the presence of oxygen vacancies. These vacancies act as diffusion carriers to transfer oxygen from the interface to the fuel electrode. If the effective (thermodynamic) oxygen partial pressure at the interface is too low, volatile indium suboxide can form, damaging intimate electrical contact between the lanthanum chromite and indium oxide layers and resulting in increased fuel cell stack resistance.

Since the oxygen vacancy content is related both to the oxygen permeability and the electrical conductivity of the lanthanum chromite, we are interested in any factors which affect this property. Two additional factors, which might change the oxygen vacancy content of lanthanum chromite, are: (1) preparation method, and (2) non-stoichiometry in occupation of the A and B sites by the metal ions of lanthanum, chromium, and magnesium in the ABO_3, perovskite structure. Work of Anderson[3] suggests that either a stable or metastable lanthanum chromite with $A \neq B$ may exist. If this can indeed occur, an oxygen loss due to metal ion vacancy "doping", similar in nature to that of magnesium ion doping of lanthanum chromite, may be possible.

Curve 712832-A

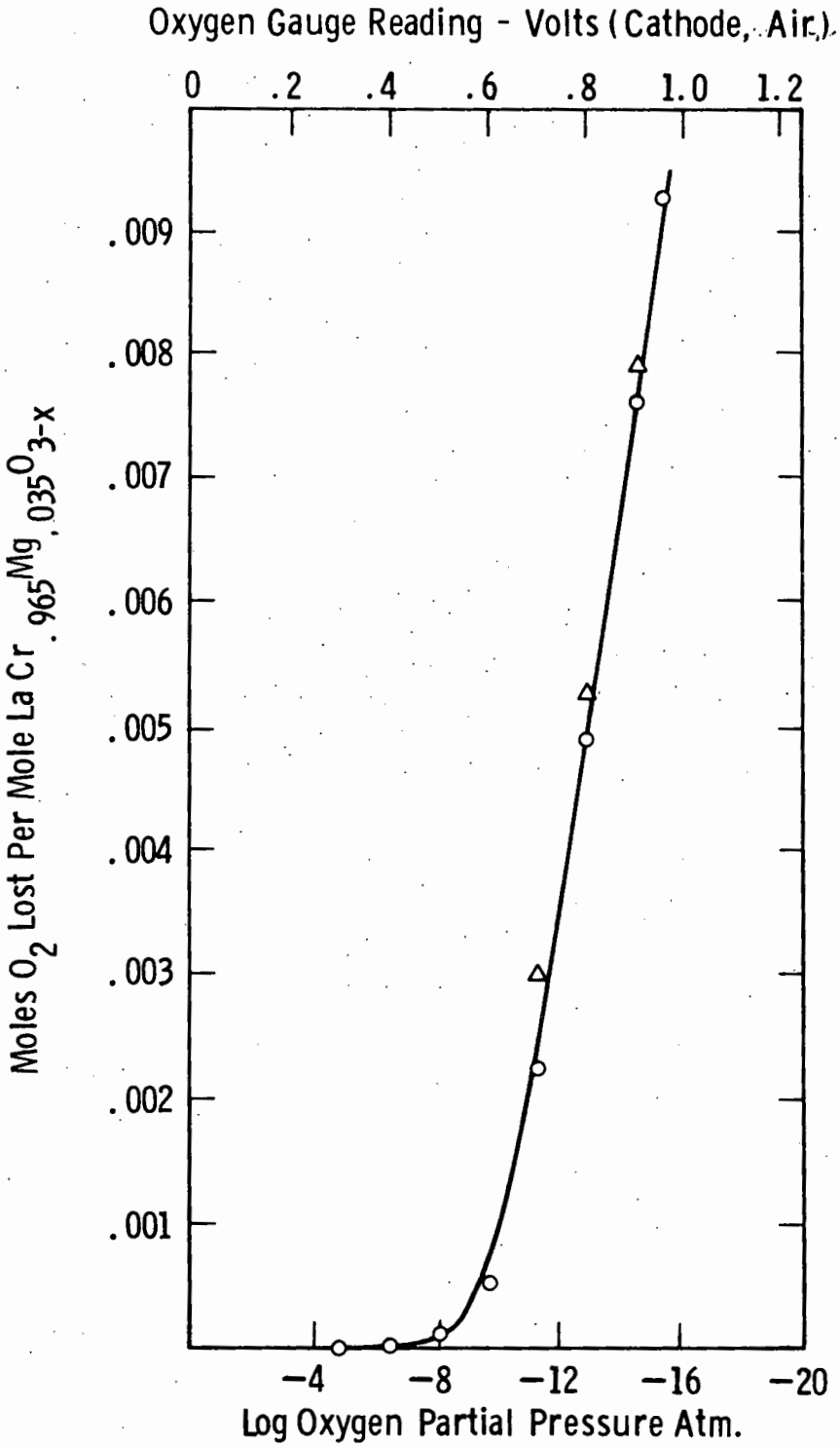

Fig. 5.32 — Oxygen loss from La $Cr_{.965}Mg_{.035}O_3$ interconnection layer stripped from nickel cermet fuel electrode

The analogous reactions for magnesium ion and "chromium vacancy" doping are:

(a) $LaCr^{3+}_{1-2x}Cr^{4+}_{x}Mg^{2+}_{x}O_3 \rightleftharpoons LaCr^{3+}_{1-2x+2y}Cr^{4+}_{x-2y}Mg^{2+}_{x}O_{3-y}\square^{o}_{y} + \frac{y}{2}O_2$

(b) $LaCr^{3+}_{1-4x}Cr^{4+}_{3x}\square^{Cr}_{x}O_3 \rightleftharpoons LaCr^{3+}_{1-4x+2y}Cr^{4+}_{3x-2y}\square^{Cr}_{x}O_{3-y}\square^{o}_{y} + \frac{y}{2}O_2$

Air Atmosphere Fuel Atmosphere

where $\square^{Cr}$ is a chromium vacancy and $\square^{o}$ is an oxygen vacancy in the perovskite crystal lattice.

To examine this possibility, we obtained three samples of lanthanum chromite with different La/Cr ratios. They have the nominal compositions (1) $LaCrO_3$ (stoichiometric), (2) $La_{1.03}CrO_{3.045}$, and (3) $LaCr_{1.03}O_{3.045}$. These were prepared for us by H. Anderson, by chemical interaction and oxidation steps, all occurring below 800°C. Under these conditions metastable solid solutions may occur. To examine this possibility, we examined each material in the high temperature microweighing apparatus in the following forms: (1) as-received powder annealed 63 hours at 1000°C in air, (2) pressed powder, heat treated at 1650°C for 17 hours in nitrogen, then annealed at 1000°C in air for 7 days. The powder samples of treatment (1) all showed a significant oxygen loss at reduced oxygen partial pressures from 1 atmosphere to 10^{-6} atmospheres oxygen. However, after the high temperature treatment (2), all samples showed losses of less than one part of ten thousand of the total oxygen content over the same pressure range. Fig. 5.33 illustrates this behavior for the nominal composition $LaCr_{1.03}O_{3+y}$. A reasonable interpretation of these results is that (1) surface desorption is responsible for most of the oxygen loss from the fine powder sample between 1 to 10^{-7} atm oxygen, and (2) that oxygen loss to form oxygen vacancies at pressures below 10^{-7} atm is largely due to the metastable

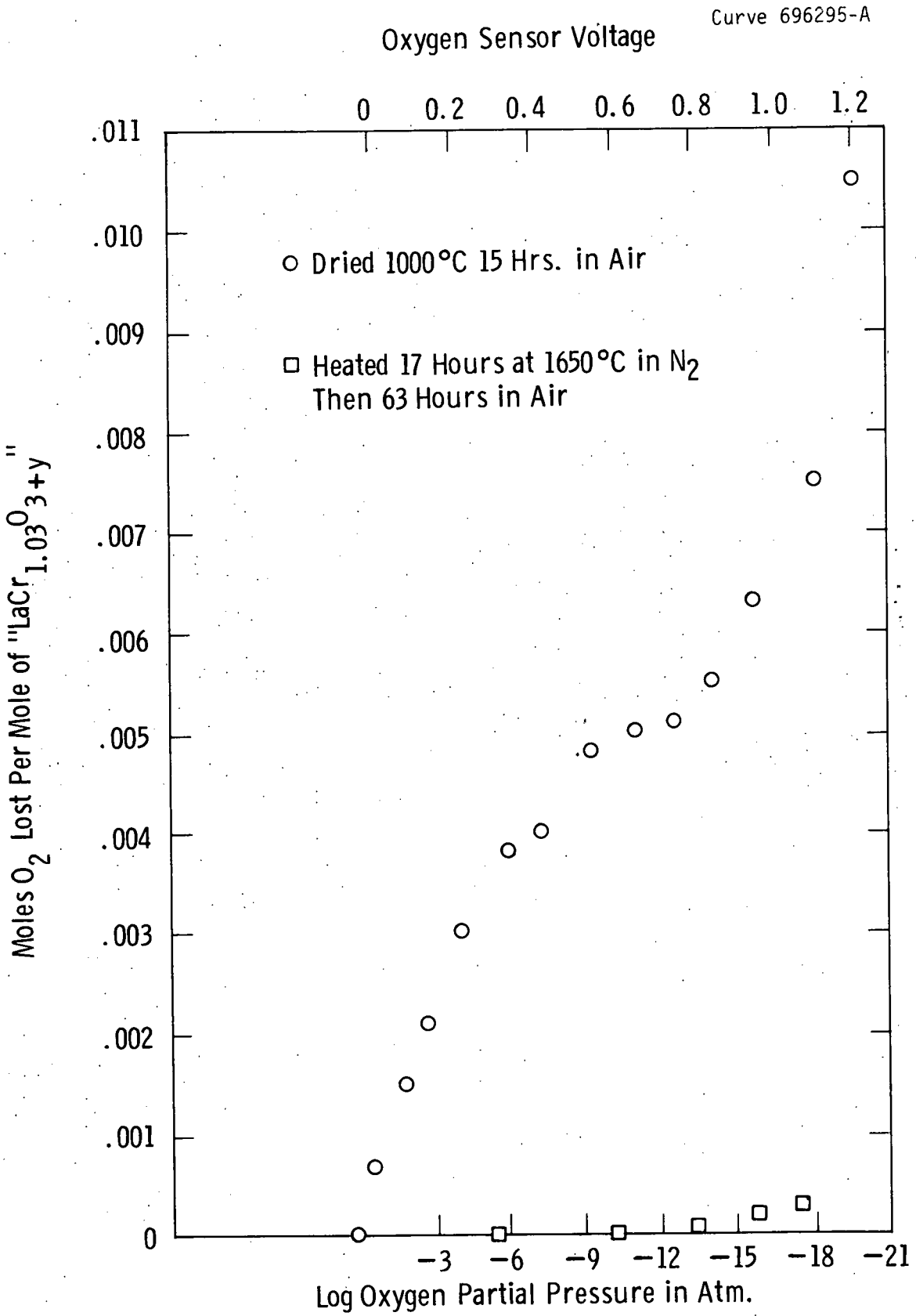

Fig. 5.33 —Effect of heat treatment on oxygen loss from "$LaCr_{1.03}O_{3+y}$" at 1000°C

presence of metal ion vacancies as suggested by the previous equation (b), and (3) cation vacancies are eliminated by appropriate heat treatment, giving us a nearly stoichiometric $LaCrO_3$ composition.

An oxygen loss attributable to surface adsorption was also seen in a similar powder preparation of $LaMg_{.02}Cr_{.75}Al_{.23}O_{3\pm x}$. This is illustrated in Fig. 5.34. High temperature heat treatment again eliminates the oxygen loss (below about 10^{-7} atmospheres) attributable to "surface adsorption". This is shown in Fig. 5.35 and represents the normal behavior of a thermodynamically stable bulk sample of a magnesium-doped lanthanum chromite. At the very high annealing temperature range of 1650 to 1700°C, significant loss of magnesium occurs as a function of time. This is accompanied by a smaller oxygen loss, as also illustrated in Fig. 5.35. At 1000°C magnesium loss is neglible and thus poses no problem for the fuel cell operating at that temperature.

We now compare these data with the analogous oxygen loss behavior of an actual lanthanum chromite interconnection film prepared by the EVD method and stripped from the fuel cell stack. The latter data are shown in Fig. 5.36. This data is consistent with that expected for the thermodynamically stable oxide. Chemical analysis of this film by atomic absorption showed the composition to be $LaCr_{.965}Mg_{.035}O_3$. The film showed the expected orthorhombic crystal symmetry by X-ray diffraction and a high (99.5% of theoretical) density.

Weight change measurements in a controlled atmosphere high temperature microweighing system are shown in Fig. 5.36. The data indicate that the oxide loses only a slight amount of oxygen up to 10^{-8} atmospheres oxygen partial pressure. This increases to about 0.32% of the total oxygen content at 10^{-16} atmospheres oxygen (using a water/hydrogen mixture), measured by a zirconia electrolyte oxygen gauge next to the sample at 1000°C.

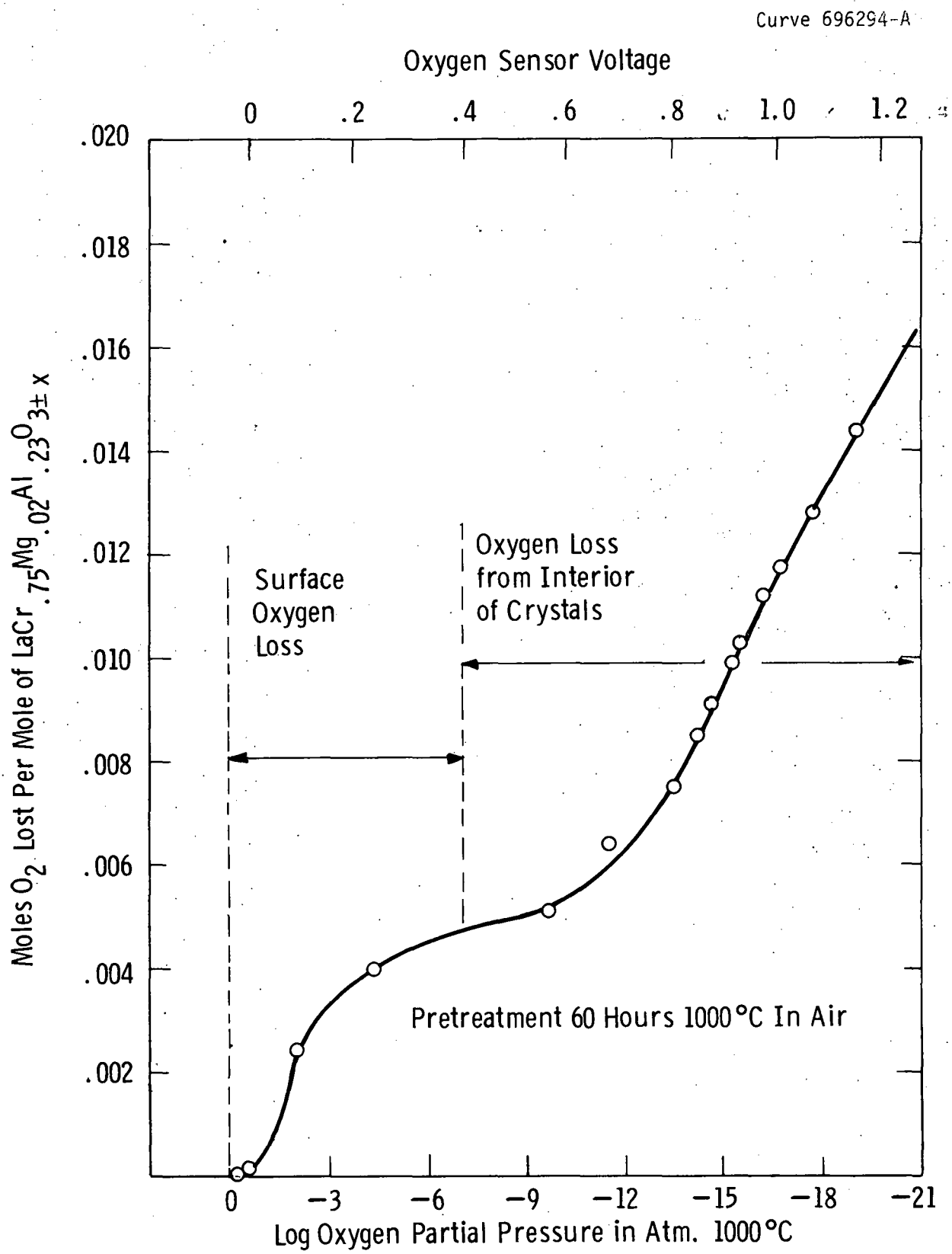

Fig. 5.34—Oxygen loss from $LaMg_{.02}Cr_{.75}Al_{.23}O_{3\pm x}$ powder at different oxygen partial pressures at 1000°C

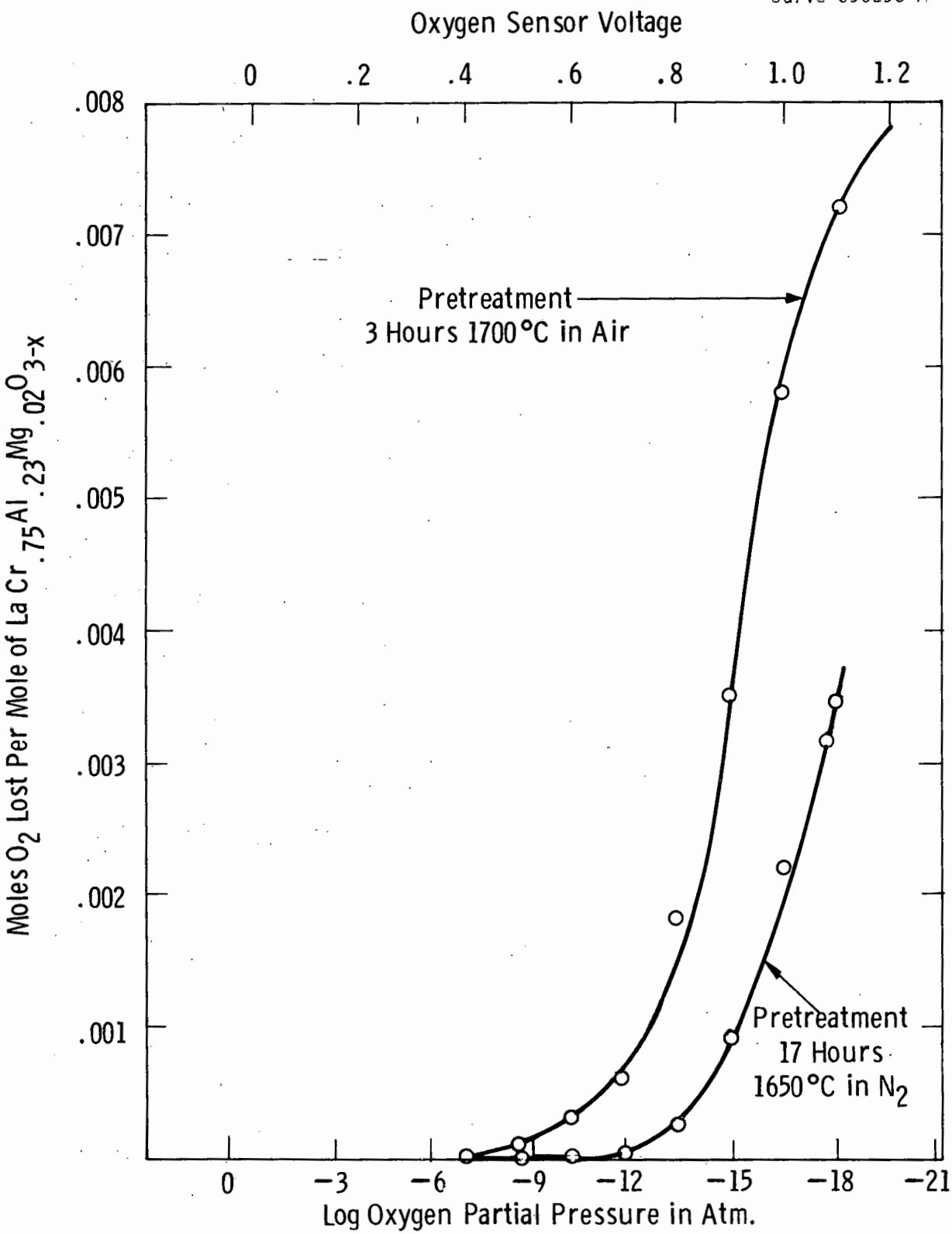

Fig. 5.35 — Effect of heat treatment on oxygen loss from "$La\,Cr_{.75}Al_{.23}Mg_{.02}O_{3\pm x}$" at different oxygen partial pressures and 1000°C

Assuming that in air one positive hole charge carrier is present for each Mg^{2+}, these data suggest that at 10^{-16} atmospheres oxygen pressure, 55% of the positive hole charge carriers are lost to provide charge compensation for the oxygen ions removed from the magnesium-doped lanthanum chromite. This would be expected to reduce the conductivity, as would positive hole trapping and charge scattering effects, resulting from additional crystal structure imperfections. Conductivity measurements show factors of six to ten drop in electrical conductivity between air and water/hydrogen atmospheres ($\sim 10^{-16}$ atm O_2).

5.2.4.2.1 Summary

In summary, these oxygen loss data, along with those based on direct chemical analysis and pycnometric density techniques, indicate that films can be produced by the EVD technique which are thermodynamically stable, stoichiometric and very dense. Electrical conductivity measurements of the films show values within the useful range of the fuel cell stack. The only troublesome feature is related to the small oxygen deficit and accompanying small permeability for oxygen in fuel atmospheres. This can cause indium oxide to flake off those areas of the interconnection where air (oxygen) access is poor.

5.2.4.3 Atmosphere Equilibration Phenomena at 1000°C in a Bulk Lanthanum Chromite Resistivity Specimen

In previous work (July 1977 through January 1978) on thin sputtered films of $La_{0.95}Mg_{0.05}Al_{0.75}Cr_{0.25}O_3$, it was found that the equilibrium values of resistance in either air or hydrogen-water atmospheres were reached within an hour at 1000°C. It was decided to examine the resistance behavior of a bulk specimen of this same composition in air and hydrogen-water atmospheres, to see whether or not the oxygen permeation behavior would be greatly different.

The specimen employed was a 2mm x 2mm x 14mm bar, cut from a much larger sample of hot-pressed $La_{0.95}Mg_{0.05}Al_{0.75}Cr_{0.25}O_3$, prepared by a homogeneous chemical reaction. (Similar material has been employed in the microbalance oxygen weight change studies that have been reported.) Platinum electrodes, 4 microns thick, were deposited on the bar by RF sputtering. A two-terminal resistance technique was employed, since the correction for leads was, at most, 1-1/2 percent of the specimen resistance. The specimen was held at 1000°C in either air or hydrogen-water ($pO_2 = 5 \times 10^{-16}$ atm) and, periodically, the temperature was varied over a wide range below 1000°C, in order to determine its resistance-temperature dependence.

The results shown in Fig. 5.37 were at first found puzzling. Equilibration with hydrogen-water appeared to occur quite rapidly (even overnight at 600°C was sufficient), indicated by the attainment of a stable, temperature-reversible resistivity curve having a high activation energy. This would be similar to the resistivity behavior obtained with thin film specimens in a hydrogen-water atmosphere.

In air, however, the "reversible" curve very slowly shifted to lower values, depending on the amount of annealing time at 1000°C. Initially the resistivity in air at 1000°C was 5.6 ohm-cm. After 110 hours of annealing it had decreased to only 3.5 ohm-cm. This is an order of magnitude higher than that obtained for thin sputtered films of this same material.

The results shown in Fig. 5.37 are understandable if one assumes that only a thin outer layer of the specimen has equilibrated with the air atmosphere for the times considered here. The specimen would then consist of the low resistivity outer layer in parallel with the higher resistivity core. At temperatures below 400°C the core contribution would be negligible; consequently the apparent resistivity

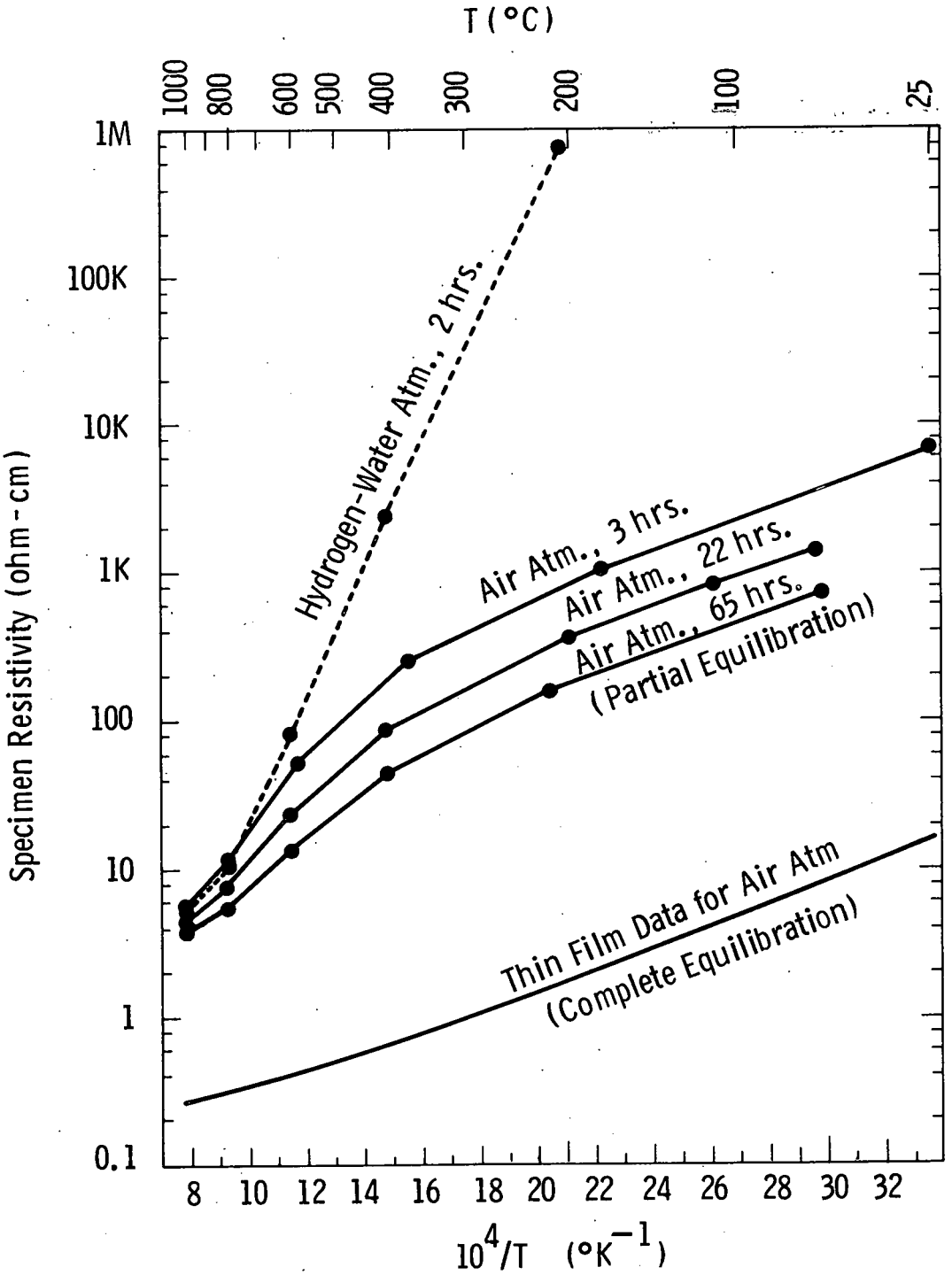

Fig. 5.36 – Resistivity vs temperature for a hot-pressed specimen of $La_{0.95}\ Mg_{0.05}\ Al_{0.75}\ Cr_{0.25}\ O_3$ as a function of equilibration time at 1000°C in air and hydrogen-water atmospheres. Previous data for thin film material in an air atmosphere is included for comparison

would exhibit a temperature dependence similar to that of a completely equilibrated specimen but would be considerably higher in absolute value, since only a thin surface layer of the specimen would conduct effectively.

On the basis of this model one can estimate the equilibration layer thicknesses for the various 1000°C equilibration times from the resistivity data at 200°C. Also, from diffusion theory one would predict that

$$(\Delta X)^2 \cong 4\ Dt \qquad (1)$$

where ΔX is the layer thickness, D is the diffusion coefficient for oxygen (1000°C) in the lanthanum chromite, and t is the 1000°C equilibration time; consequently it is possible to obtain estimates of D from the data. Values for thicknesses and diffusion coefficient appear in Table 5.3 below:

TABLE 5.3 RELATIONSHIP BETWEEN OXYGEN DIFFUSION COEFFICIENT AND LAYER THICKNESS IN $La_{0.95}Mg_{0.05}A\ell_{0.75}Cr_{0.25}O_3$

t(hrs)	$\Delta X(\mu m)$	$D(cm^2/sec)$
3	1.0	2.3×10^{-13}
22	2.2	1.5×10^{-13}
65	4.5	2.2×10^{-13}

The approximate constancy of values for D lends support to a diffusion mechanism for surface equilibration. The value of D, $\sim 2 \times 10^{-13}$ cm^2/sec, is surprisingly small; however, the value for oxygen diffusion in NiO at 1000°C is about this same magnitude.[9] It should be noted that a sputtered 3 μm thick film of lanthanum chromite was found in earlier work to equilibrate with air in less than 1 hour.

One might consider this to contradict the results given here; however, the extremely fine grain size in such a film might lead to a higher oxygen diffusion rate, via penetration of and irrigation from the grain boundaries.

5.2.4.4 High Temperature Resistivity of $In_{1.96}Sn_{0.04}O_{3\pm X}$ as a Function of Oxygen Partial Pressure

Due to the finite oxygen diffusivity within the lanthanum chromite interconnection material there is the real possibility that a low oxygen partial pressure condition may exist at the air electrode-interconnection interface. It was, therefore, deemed important to obtain information on the high temperature resistivity of air electrode material (tin-doped indium oxide) as a function of oxygen partial pressure.

5.2.4.4.1 Specimen Preparation and Measurement

Homogenized powder, corresponding to the composition $In_{1.96}Sn_{0.04}O_3$, was ground, reacted at 1500°C, reground, and finally sintered into disks at 1500°C for 6 hours. From this material a bar specimen was cut (27 mm x 4 mm x 3 mm), four electrode bands (platinum, 4 μm thickness) were sputtered onto its surface, and suitable platinum wire leads were attached to these bands, completing a four-terminal specimen. This test sample was mounted in the measurement furnace where the desired oxygen partial pressures were achieved by the use of flowing mixtures of oxygen-inert gas or hydrogen-water-inert gas. The specimen resistance was determined by a standard four-terminal method.

5.2.4.4.2 Results and Discussion

Times for equilibration of the specimen with the atmospheres varied from minutes (100°C, $P_{O_2} \geq 10^{-2}$ atm) to hours (900°C, $P_{O_2} \leq 10^{-2}$ atm),

as judged by the time required for the specimen resistance to become constant. Reversibility, indicated by the repeatability in resistance when the sequence of atmospheres employed was reversed, was very good at 1000°C. The results are presented in Fig. 5.38. Due to the porous character of the specimen, the resistivity was about one order of magnitude higher than that of a dense vapor deposited film (see previous contract Final Report).[1]

The resistivity decreased with decreasing oxygen partial pressure, as would be expected for an n-type oxide semiconductor. It was found that the data for specimen resistivity, ρ, could be fitted by an equation of the form

$$\rho = \rho_1 P_{O_2}^{1/n} + \rho_2 \qquad (1)$$

where ρ_1, ρ_2, and n were constants. The values found for n were 7.0 at 900°C and 6.7 at 1000°C. The form of Eq. (1) is in agreement with theoretical work by DeWit[10] for undoped In_2O_3. He predicts the first term with n = 6 as a consequence of the non-stoichiometric decomposition reaction

$$O^{=} \rightleftharpoons \square^{o} + 2e + \frac{1}{2} O_2 \qquad (2)$$

where $O^{=}$ is an oxygen ion, $\square^{o}$ is an oxygen ion vacancy, and e is an electron. In addition he suggests that a significant grain boundary resistance is present in polycrystalline specimens; this would lead to the second term, ρ_2, in Eq. (1).

This approximate agreement with Eq. (2) for the decomposition reaction is surprising. As discussed elsewhere in this report, one would expect to find the SnO_2 incorporated into the In_2O_3 lattice, either via

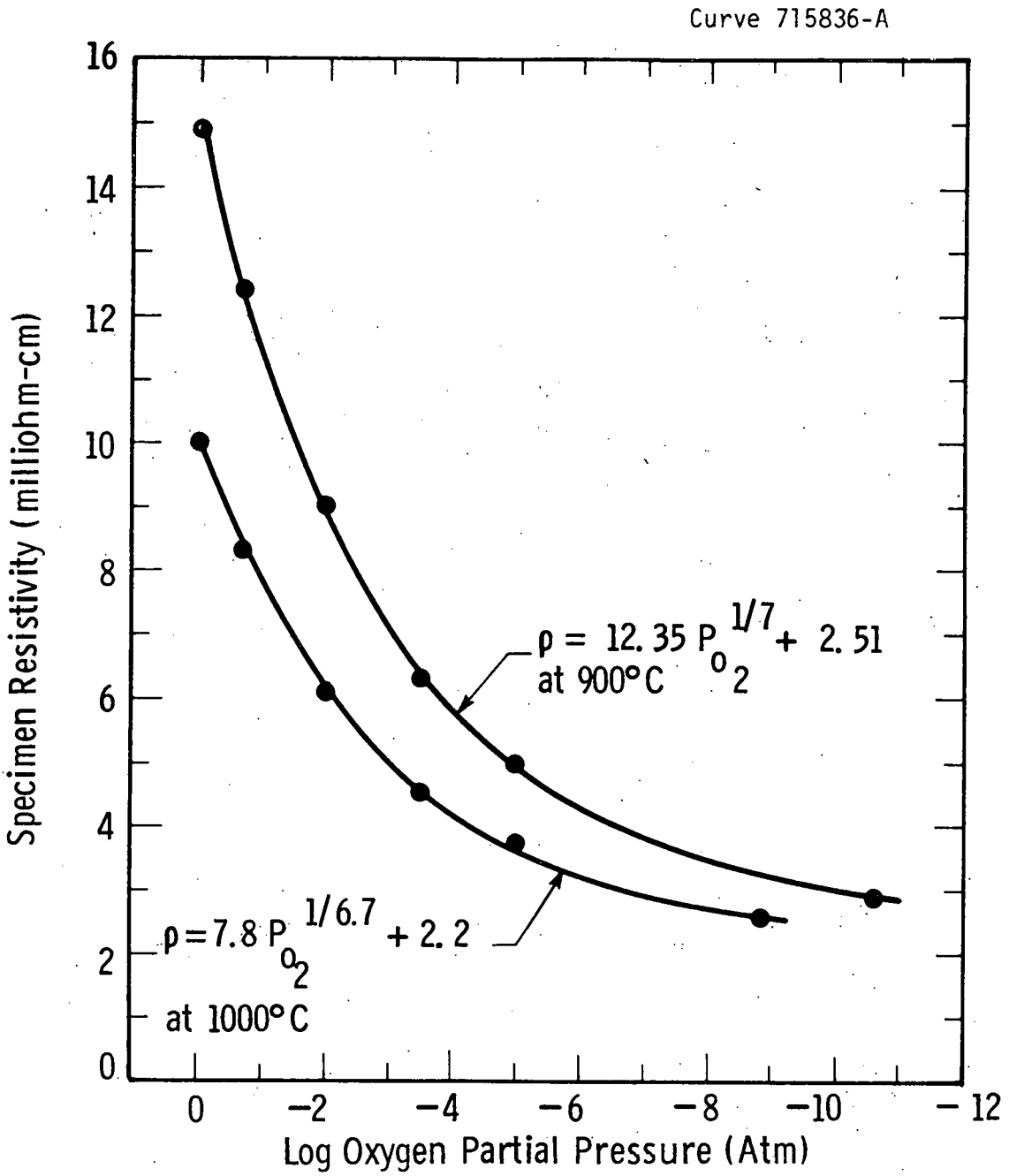

Fig. 5.37 — High temperature resistivity of a bulk specimen of $In_{1.96}Sn_{0.04}O_{3\pm X}$ vs. oxygen partial pressure. A semi-empirical equation having the form $\rho = \rho_1 P_{O_2}^{1/n} + \rho_2$ has been fitted to the data

interstitial oxygen ions or via cation vacancies. In the former case the decomposition reaction would be

$$O_I^{=} \rightleftharpoons \frac{1}{2} O_2 + 2e \qquad (3)$$

where $O_I^{=}$ is an oxygen ion interstitial, while in the latter case the reaction would be

$$O^{=} + \frac{2}{3} \square_{cat.} \rightleftharpoons \frac{1}{2} O_2 + 2e \qquad (4)$$

where $\square_{cat.}$ is a cation-site vacancy. In either case, application of the mass action law leads to $\rho \propto P_{O_2}^{1/4}$ at the higher oxygen partial pressures, in strong disagreement with the data; however, the expressions for ρ do give an asymptotic value ρ_2 at low oxygen pressure without the necessity of assuming a grain boundary resistance. Further work would obviously be required before one could specify the precise decomposition mechanism.

5.2.4.5 Alternate Air Electrode Materials

The initial intent of this work was to provide an intermediate oxygen permeable oxide layer between the indium oxide and the lanthanum chromite interconnection. However, further exploratory investigations of other cathode materials were triggered by the surprisingly-good performance of a copper oxide bonded air electrode of $La_{0.9}Sr_{0.1}MnO_3$, as described in Section 5.2.5.4. This is a cathode material, similar to one used successfully by Rohr[4], and known to be useful for long term operation and thermal cycling. From a materials cost standpoint it would be desirable to substitute calcium and, perhaps, cerium for all, or part, of the lanthanum. $Ca_{0.5}La_{0.5}MnO_3$ is one of the compositions being considered. Its good features are (1) excellent thermal expansion

match with the lanthanum chromite and zirconia electrolyte (see Fig. 5.38), (2) adequate electrical conductivity, which is nearly temperature independent above 300°C (see Fig. 5.39), and (3) relatively low-cost materials.

Subsequent studies will investigate this material along with modifications in its composition. Also, electrodes will be formed by bonding with a lower melting oxide (1000-1350°C) additive.

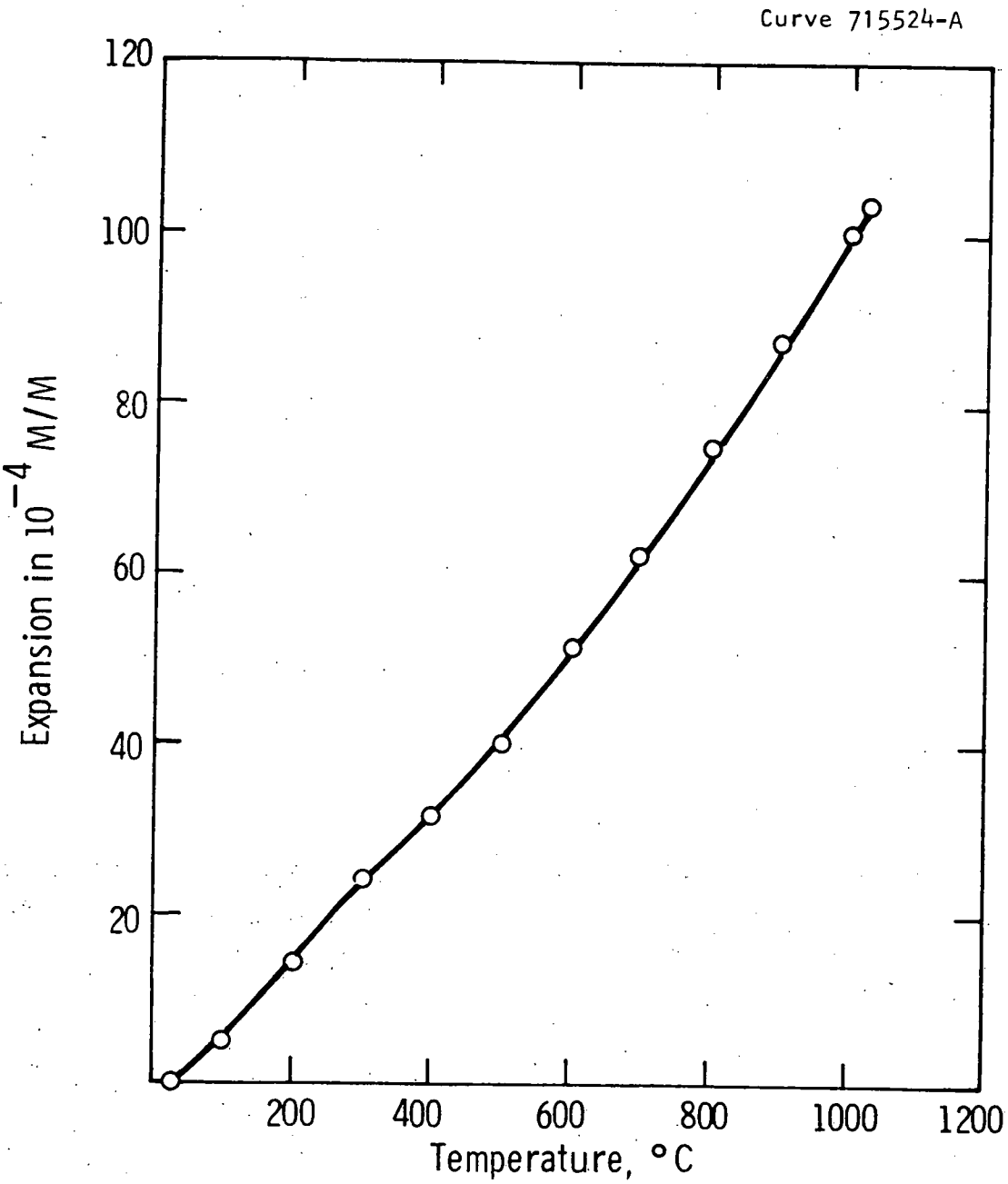

Fig. 5.38—Thermal expansion of $Ca_{.5}La_{.5}MnO_3$ in air

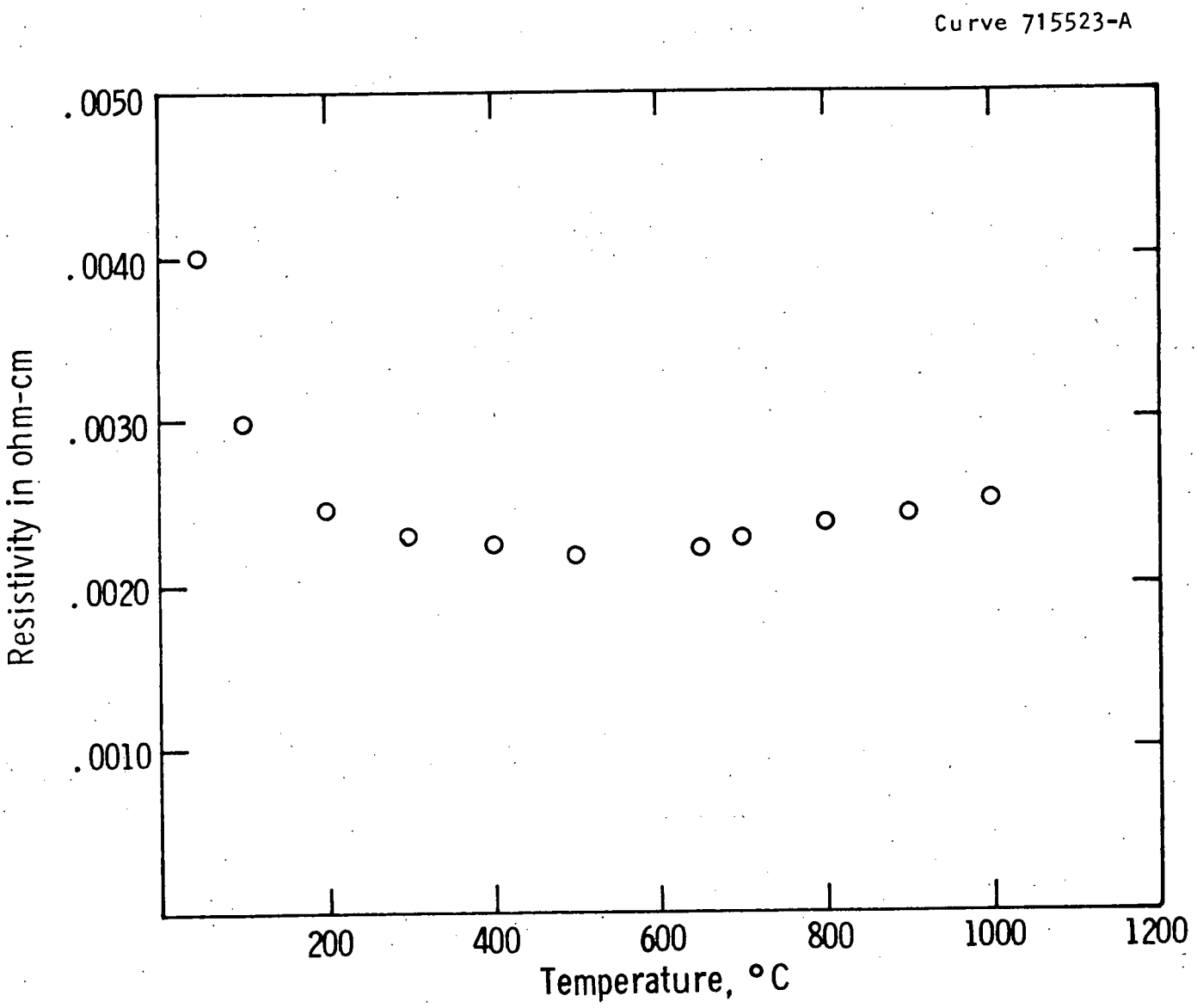

Fig. 5.39 – Resistivity vs temp of $La_{.5}Ca_{.5}MnO_3$

5.2.5 Subtask D. Single Cell Life Test

Work in this area was deferred so that effort could be concentrated on obtaining small and 20 cell fuel cell stacks, from which the single cell data would be derived.

5.2.5 Subtask E. Small Stack Life Test

A 7-cell stack (stack #2) was prepared from the end section of a 25-cell stack, as seen with respect to its location in the EVD reactor during the electrolyte and IC deposition (4 cells were lost because of cutting and mounting procedures). The performance of stack #2 was compared with that of the first stack, tested under the previous contract in February 1978. The first stack was produced from a six inch long section which represents the front portion of a stack having both an interconnection and electrolyte deposition by the EVD process.

5.2.5.1 Seven-Cell Stack Performance (Stack #2)

The first and last cell of the stack were equipped with current and potential leads and the stack was heated slowly to the operating temperature of 990°C with forming gas (to protect the fuel electrode from oxidation, until the gold-washer seals were tight). Hydrogen/3% water was used as the fuel and air was the oxidant. Fig. 5.39 shows the initial stack performance.

5.2.5.2 Five-Cell Stack Performance (Stack #2)

The stack was cooled slowly to room temperature for instrumentation of individual cells. This was done after end sealing in order to avoid damaging the mechanically unstable compression seal. This seal becomes stronger after the gold washers are compressed and conform to the tube circumference. Stack #2 performance of five cells is shown in Fig. 5.40 and is compared with that of stack #1. Cells 1 and 7 in stack #2 were used as potential-monitored cells, to determine inlet and outlet fuel potential.

5.2.5.2.1 Discussion of Stack #2 Performance

Overpotential losses during stack operation were investigated, using the current interruption technique. The results are plotted in

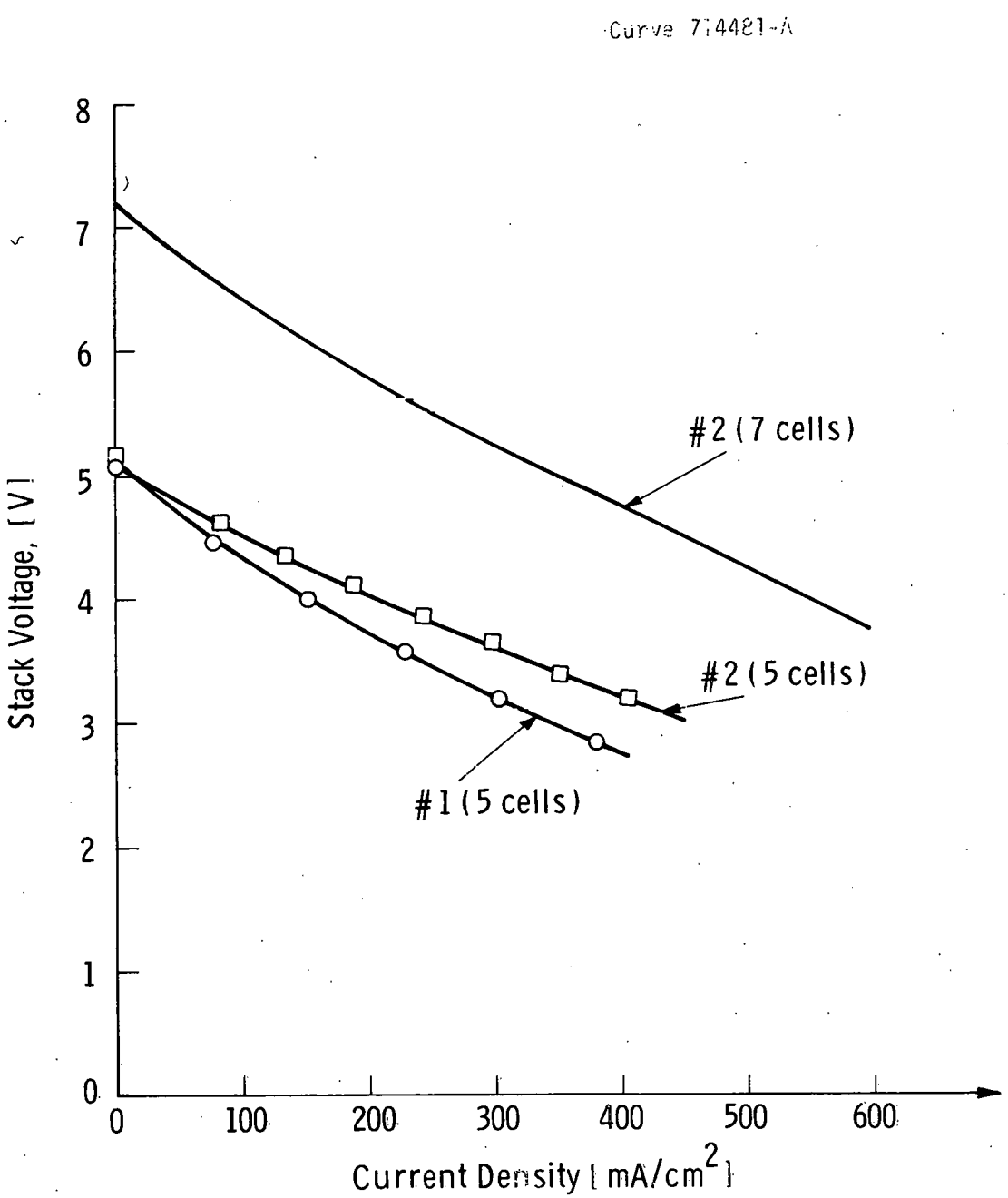

Fig. 5.40 – Performance of cell stacks at 990°C in air using H_2/3% H_2O as fuel (less than 5% fuel consumption)

Fig. 5.40 and, again, compared with results obtained from stack #1. The comparison shows that both stacks behave similarly with respect to slow (concentration) polarization. Stack #2 shows some improvement (5 to 10%) over stack #1.

However, considerable improvement is seen with respect to the reduction of ohmic resistance of stack #2, which is only 50 percent of the internal resistance of stack #1. The calculated IR characteristic shows that a further reduction by 50 percent should be achieved with present materials. This IR curve was calculated for the following conditions:

- Temperature - 1000°C
- Stack circumference - 4.15 cm
- IC active band width - 0.25 cm
- IC thickness - 40 μm
- IC resistivity - 31 Ω-cm (see Section 5.2.4.3 under the assumption of insufficient equilibration with air)
- Active cell band width - 0.43 cm
- Electrolyte thickness - 20 μm
- Electrolyte resistivity - 10 Ω-cm
- Fuel electrode ρ/δ - 0.1 Ω
- Air electrode ρ/δ - 0.4 Ω
- Equalized conductor length for fuel and air electrode (center of electrode to center of interconnection) - 0.55 cm

Using these data one calculates average resistances for five interconnected cell components as follows:

Fuel electrodes	0.066 Ω
Air electrodes	0.265 Ω
Electrolyte	0.056 Ω
Interconnections	0.598 Ω
TOTAL	0.985 Ω

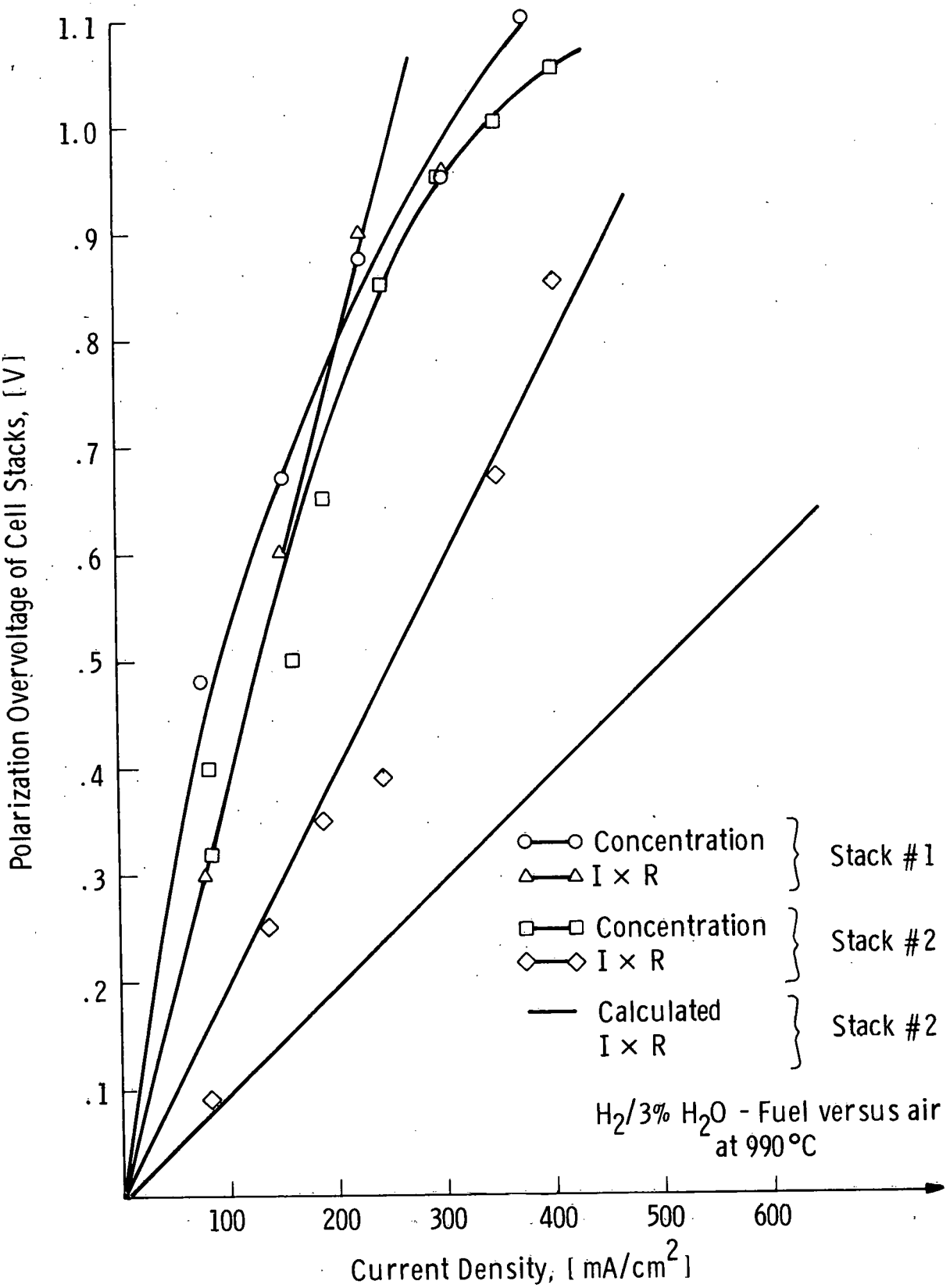

Fig. 5.41 — Polarization losses in #1 and #2 stacks of 5 cells

The reduction of internal resistance of stack #2 is due to improvements in deposition conditions for IC materials. Also, better conducting air and fuel electrodes have been fabricated. The approximate calculation shows, also, that resistance-related improvements in performance can best be achieved by reducing air electrode and IC resistance. While air electrode conductance can be improved moderately, it is believed that of the interconnection can be improved by almost one order of magnitude, after proper doping levels have been obtained.

The calculations do not take into consideration the resistance that is introduced by the porous layer between electrolyte and air electrode collector, due to the absence of measured data. It is assumed, however, that this resistance could add as much as 0.1 Ω to the total stack resistance.

Slow, but steady, deterioration of stack performance was observed from the beginning of the test. The deterioration was not caused by leaks, as open stack voltage was near 99 percent of the theoretical value. It had been observed that, during the first temperature cycle, indium oxide flakes had fallen off the interconnection region, as seen in the photo of stack #2 in Fig. 5.42. This effect had been noted also in stack #1, yet not to the degree as in stack #2. Stack #2 had a thicker In_2O_3 layer than stack #1 and, when it lifted off the IC, it flaked in much larger patches. During testing it became obvious that the stack would not meet the life performance goal after 1000 hours of operation and therefore, it was removed from the life test apparatus. The stack has been disassembled for analysis (which has not been concluded at the time of this writing). The flaking of In_2O_3 - current collector over the IC will lead to additional lateral resistance losses in the collector and introduce contact resistance between the air electrode collector and the IC. None of these losses have been considered in the

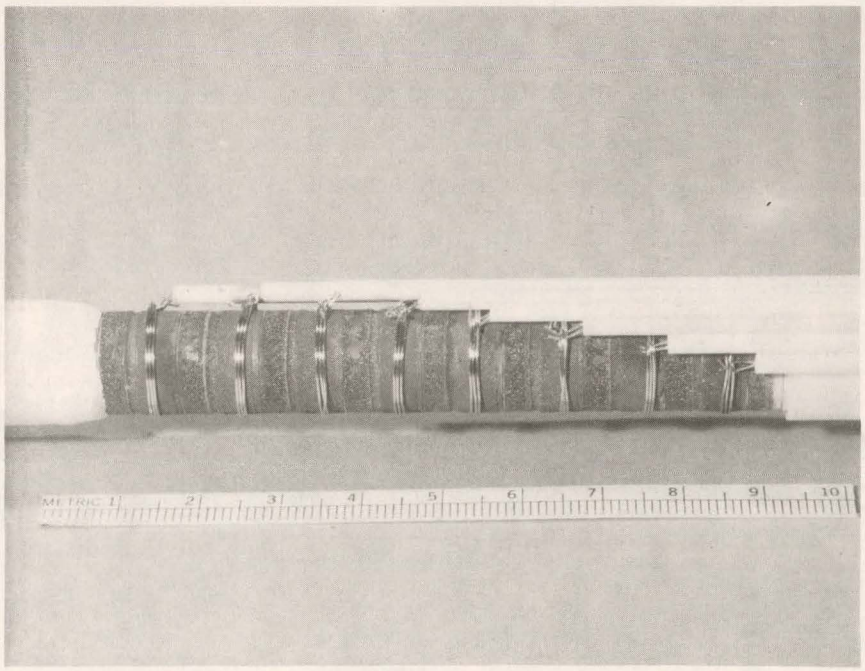

Fig. 5.42 Five Cell Stack Test of Seven Cell Module (Stack #2), (showing flaking in the dark crystalline IC bands)

cell resistance calculations, because of the inability of making valid assumptions. These facts can explain the considerable discrepancy between measured and calculated ohmic resistance of the cell stack. After removal from the life test apparatus, the cell stack was leak tested. It exhibited similar gas tightness, as before mounting and elevated temperature operation.

5.2.5.3 Five-Cell Stack Performance (Stack #3)

Stack #3 was prepared with the specific goal of reducing the IC resistance losses, using the latest improved deposition techniques for lanthanum chromite. The air and fuel electrode performance of stack #3 can be assumed to be similar to that of stack #2, because of identical materials and fabrication techniques. The improvement in stack performance can, therefore, be attributed to the higher conductivity of the IC layer, see Fig. 5.43, curve A. The stack, initially, exceeded the performance goal of this program (0.66 V at 400 mA/cm^2), demonstrating the correctness of our assumption that the reduction of internal resistance, especially that of the IC layer, will improve stack performance considerably. Similar to stack #2, the stack performance deteriorated, due to In_2O_3 - flaking from the IC area.

5.2.5.4 Fourteen-Cell Stack Performance (Stack #4)

Durable air electrode-IC contact should lead to steady stack performance. In order to test materials, that can be applied to IC's, we choose strontium-doped lanthanum manganite sintered powder layers. Since the resistivity of this material is close to 5×10^{-3} Ω cm (when dense), we used it also as air electrode current collector. Curve B in Fig. 5.43 represents the stack characteristic. The stack performance was steady (for seven days; four thermal cycles) and demonstrated the possibility of using other oxides in contact with the IC. However,

Curve 715854-A

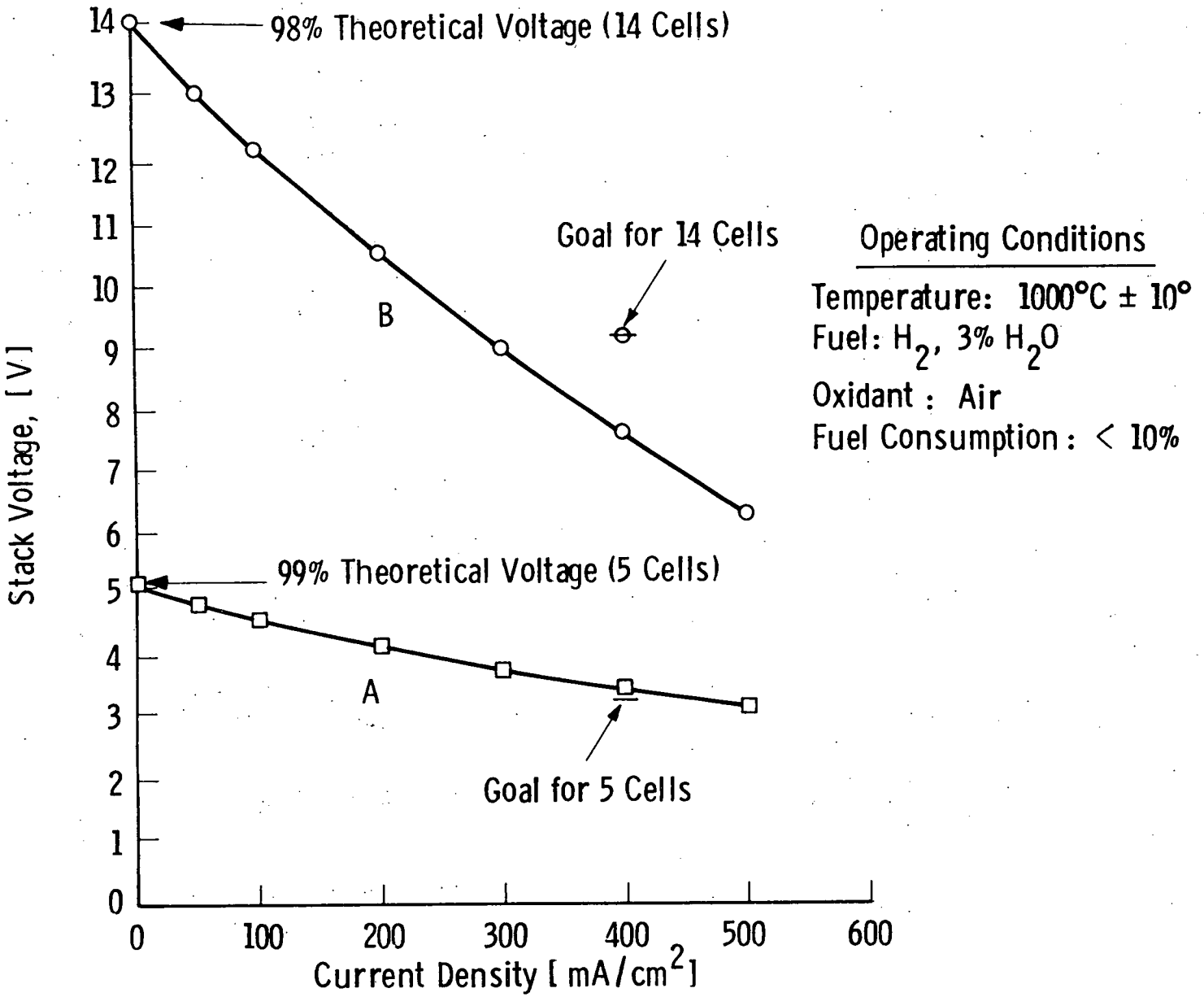

Fig. 5.43 — State-of-the-art performance of cell stacks
A - In_2O_3 - air electrode B - La MnO_3 - air electrode

performance goals could not be achieved, due to the higher resistance in the air electrode current collector (porous $La_{0.9}Sr_{0.1}MnO_3$).

5.2.5.5 Conclusions of Stack Performance

It has been shown that performance goals of 0.66 V at 400 mA/cm^2 can be obtained, yet IC contacting problems to In_2O_3 prevent steady stack performance. Steady, yet insufficient performance can be obtained with doped lanthanum manganite/IC contacts. The present goal of our work, therefore, is the combination of both materials to meet stack target performance. Stacks will be fabricated, that will connect the IC material with the In_2O_3 air electrode current collector, via a porous layer of lanthanum manganite, sandwiched between these two layers. The short excursion into testing doped La MnO_3 as air electrode current collector, suggests future work in trying to replace In_2O_3 altogether, by less expensive and less attack-susceptible oxides.

5.3 TASK 3. STACK PERFORMANCE EVALUATION

This task is concerned with the testing of cell stacks under a variety of conditions to which they might be exposed in the operation of an envisioned power plant. The current-voltage characteristics of the stacks will be measured under three conditions: normal air and fuel conditions, rich and lean air and fuel conditions (including the water component of fuel) and interrupted current conditions. These measurements will aid in determining the magnitude and type of voltage losses associated with the individual stack components, and their contribution to the operational characteristics of the stack. Because of their diagnostic value, the tests will also be used for the cells in Task 1, (Subtask E), Task 2 (Subtask D) and Task 2 (Subtask E).

In order to interpret the measurements it would be very helpful to have an elementary theory for the current-voltage characteristic (V-I curve) which correctly predicts the qualitative features of our experimental stack data. An attempt to construct such a theory is given below, with results which are interesting and perhaps surprising.

5.3.1 V-I Characteristic Theory for a HTSOE Fuel Cell with H_2-H_2O Fuel

Ideally the terminal potential, V, of a fuel cell would have the form

$$V = E_o - IR_o \qquad (1)$$

where E_o is the theoretical (thermodynamic) open circuit potential of the cell, I is the current being drawn and R_o is the ohmic internal resistance. In practice, the form is found to be rather

$$V = V_o - IR_o - \eta(I) \qquad (2)$$

where the open circuit potential, V_o, is somewhat less* than the theoretical value, E_o, and an additional voltage loss term, $\eta(I)$, is included to describe the effects of various electrochemical polarizations occurring at the electrodes.

---

*Some reasons for this are discussed in Section 5.3.3.

A major assumption of our treatment is that the overpotential term, $\eta(I)$, arises only from simple concentration polarization losses in the electrodes when the fuel is hydrogen-water. Justification for this assumption will not be given here; a pertinent reference is the work of Etsell and Flengas.[11] Other assumptions are made:

1) excess fuel and air are used so that depletion gradients in the supply system are negligible.*
2) the ohmic resistance term, R_o, includes the electronic resistance of the air electrode, fuel electrode, and interconnection, plus the ionic resistance of the solid electrolyte.
3) lumped parameters are used in the equations.

*This assumption is easily satisfied in experimental tests; however, it does not hold when one is dealing with a fuel cell stack having nearly complete hydrogen combustion, as would occur in a working power plant. A straightforward extension of the theory presented here enables one to deal with this case.

The schematic in Fig. 5.42 shows the pertinent component gas fluxes and partial pressures. At the air electrode the concentration overpotential, η_{air}, is given by the Nernst equation*

$$\eta_{air} = \left[\frac{RT}{4F}\right] \ln \left(P_{O_2}/P_{O_2}'\right) \tag{3}$$

where R is the gas content, T the absolute temperature, and F is the Faraday constant

At the fuel electrode an analogous expression holds for the overpotential:

$$\eta_{fuel} = \left[\frac{RT}{4F}\right] \ln \left(P_{O_{2(fuel)}}'/P_{O_{2(fuel)}}\right) \tag{4}$$

However, it is more useful to write the oxygen partial pressures here in terms of fuel component partial pressures. Since the reaction $H_2 + 1/2\ O_2 \rightleftharpoons H_2O$ implies that

$$P_{O_{2(fuel)}} = \frac{1}{K^2}\left[P_{H_2O}/P_{H_2}\right]^2 \tag{5}$$

where K is the equilibrium constant, the fuel electrode concentration overpotential can be written as

$$\eta_{fuel} = \left[\frac{RT}{2F}\right] \ln \left(P_{H_2}/P_{H_2}'\right) + \left[\frac{RT}{2F}\right] \ln \left(P_{H_2O}'/P_{H_2O}\right) \tag{6}$$

The forms of this equation suggests labelling of the two terms as follows:

$$\eta_{fuel} \equiv \eta_{hydrogen} + \eta_{water} \equiv \tag{7}$$

and thus the total concentration overpotential, η, becomes

$$\eta = \eta_{air} + \eta_{hydrogen} + \eta_{water} \tag{8}$$

---

*In each of the overpotential equations presented here, the ratio of partial pressures will be chosen so that the overpotential is positive for normal cell operation.

Curve 6451A33

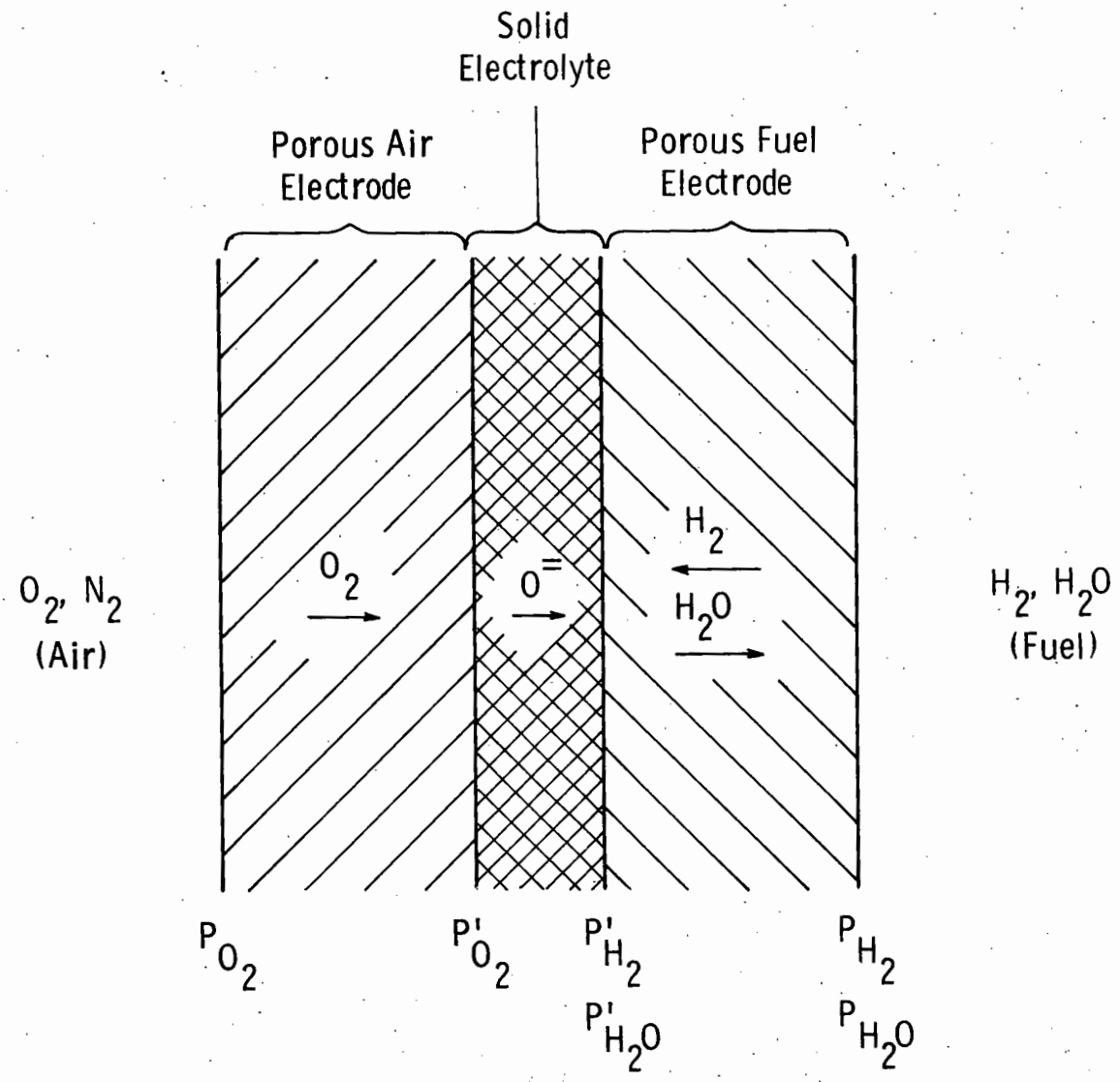

Fig. 5.44- Schematic of the mass transport flows in an idealized high temperature solid electrolyte fuel cell, operating with hydrogen-water fuel. The unprimed variables are air or fuel component partial pressures as supplied to the cell; the primed variables are partial pressures at the solid electrolyte-porous electrode interfaces.

It will be shown that, typically, the air and hydrogen concentration overpotentials predominate at high currents, while the water concentration overpotential predominates at low and medium currents.

The final step in obtaining a working equation for the V-I characteristic requires that we link the partial pressures at the electrolyte interfaces (P_{O_2}', P_{H_2}', P_{H_2O}' in Fig. 5.42 with the cell current, I, being drawn. First, it can be shown that the gas fluxes through our electrodes are controlled by pore diffusion rather than viscous or molecular flow. This implies that for each component gas, an approximately linear relation

$$\text{flux} \propto \text{partial pressure difference} \tag{9}$$

will be valid. Second, each component gas flux is directly or indirectly linked to charge transfer at the electrodes, e.g., $1/2\ O_2 + 2e \rightleftharpoons O^=$ and $O^= + H_2 \rightleftharpoons H_2O + 2e$; this implies for each component gas

$$\text{flux} \propto \text{cell current} \tag{10}$$

and hence

$$\text{cell current} \propto \text{partial pressure difference}$$

Explicitly, one has

$$I = S_{O_2}(P_{O_2} - P_{O_2}') = S_{H_2}(P_{H_2} - P_{H_2}') = S_{H_2O}(P_{H_2O}' - P_{H_2O}) \tag{11}$$

where the S's are proportionality constants having the dimensions, mA/atm. They are essentially component gas diffusion conductances for the electrodes, expressed in terms of charge flow rather than mass or volume flow.*

*An exact treatment of the S's requires an analysis of component counter-diffusion (H_2-H_2O, O_2-N_2) within the electrode pores and will not be discussed here.

Finally, by substituting (11) in (3), (4) and (6) one has

$$\eta_{air} = \left[\frac{RT}{4F}\right] \ln\left[\frac{S_{O_2} P_{O_2}}{S_{O_2} P_{O_2} - I}\right] \tag{12}$$

$$\eta_{hyrogen} = \left[\frac{RT}{2F}\right] \ln\left[\frac{S_{H_2} P_{H_2}}{S_{H_2} P_{H_2} - I}\right] \tag{13}$$

$$\eta_{water} = \left[\frac{RT}{2F}\right] \ln\left[\frac{S_{H_2O} P_{H_2O} + I}{S_{H_2O} P_{H_2O}}\right] \tag{14}$$

and from Equations (2) and (8),

$$V = V_o - IR_o - \eta_{air} - \eta_{hydrogen} - \eta_{water} \tag{15}$$

These last four equations summarize our theory of the V-I characteristic for hydrogen-water fuel.

5.3.1.1 Qualitative Behavior of the V-I Characteristic

Interesting non-linear behavior in the V-I characteristic arises from the electrode overpotentials η_{air}, $\eta_{hydrogen}$, η_{water},

described by Equations (12), (13), and (14). Their important features are listed in the following:

5.3.1.2 Air and Hydrogen Overpotentials

These overpotentials have 3 characteristics:

1) they produce curvature in the V-I characteristic which is concave downward.
2) they have limiting currents which correspond to O_2 or H_2 starvation at the electrode-electrolyte interfaces.
3) for typical fuel cell parameters they are nearly linear at low-to-moderate currents and become rapidly non-linear (and large) at high currents.

5.3.1.3 Water Overpotential

This overpotential has 3 characteristics:

1) it produces a curvature in the V-I characteristic which is concave upward.
2) no limiting current occurs; H_2O pressure at the electrode-electrolyte interface can become large.
3) for typical fuel cell test parameters, this overvoltage is significantly large and non-linear at low currents; it increases relatively slowly at high currents.

An example of the V-I characteristic and the contributions of the various overpotentials are shown in Fig. 5.45. These curves were calculated from Equations (12) through (15) for a hypothetical fuel cell with the parameters listed. Since the usual range for operation and/or life testing with this cell would be below a maximum current of approximately 1000-1200 mA, the relative importance of the water concentration polarization compared to that of air or hydrogen is evident.

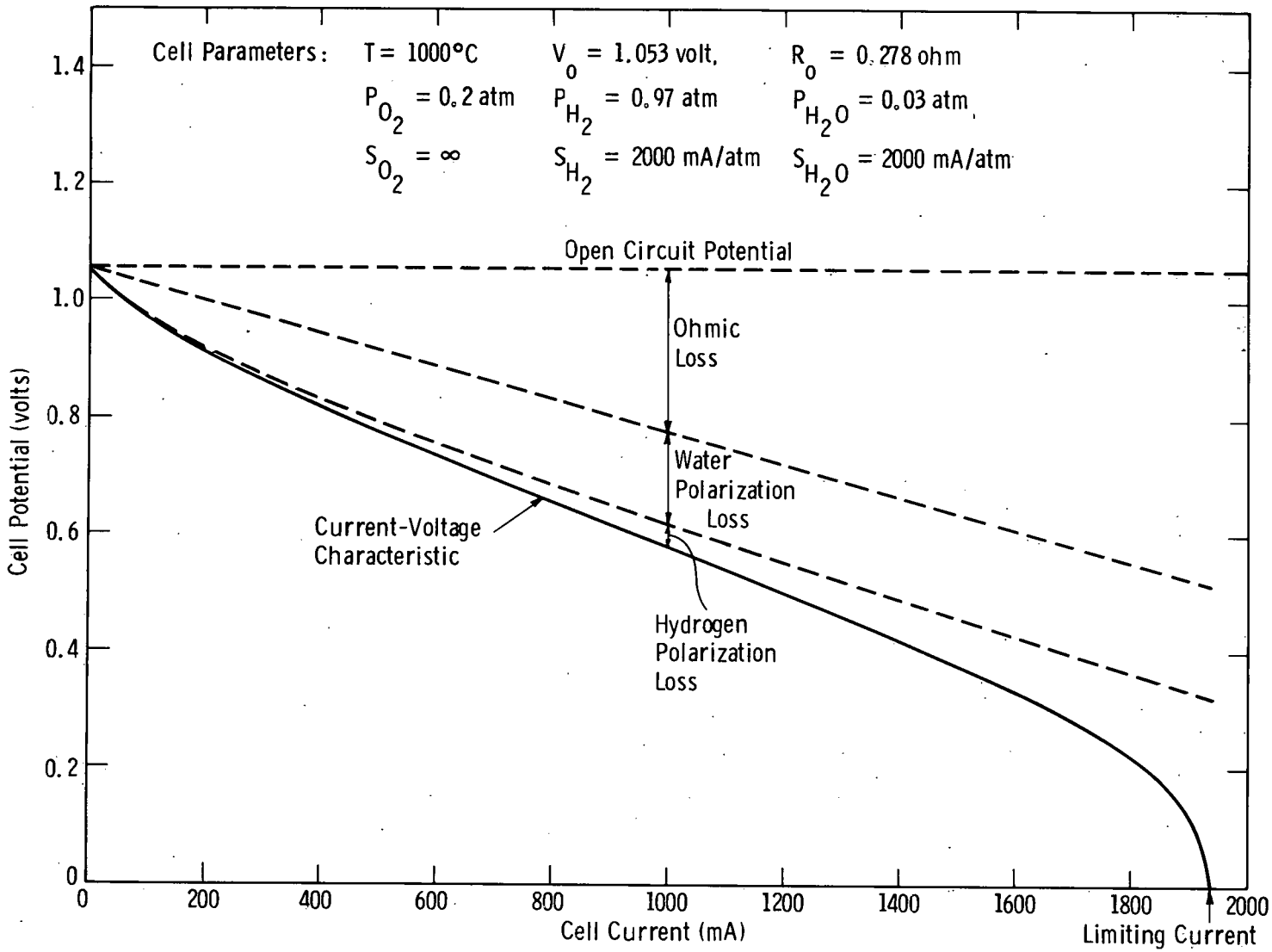

Fig. 5.45 — Theoretical behavior of the current-voltage characteristic for a cell, showing the ohmic and concentration polarization voltage losses. For this example the air electrode concentration polarization is assumed negligible; when present it is very similar to the hydrogen concentration polarization in behavior.

5.3.2 Comparison of Theory with Early Stack Data

An important simplification in the equations can be made for the case where the cell current is well below (<one-half) the limiting air or hydrogen polarization currents. This is often the case for the usual stack tests. Equations (12) and (13) for the air and hydrogen overpotentials are then almost linear with current and can be written

$$\eta_{air} \simeq \left[\frac{RT}{4FS_{O_2}P_{O_2}}\right] I \equiv R_{air} I \tag{16}$$

$$\eta_{hydrogen} \simeq \left[\frac{RT}{2FS_{H_2}P_{H_2}}\right] I \equiv R_{hydrogen} I \tag{17}$$

i.e., as far as the DC current-voltage characteristic is concerned, the air and hydrogen polarizations behave like ohmic resistances, R_{air} and $R_{hydrogen}$, defined above. This allows us to write the V-I characteristic equation for low-to-moderate currents as

$$V = V_o - IR_1 - \left[\frac{RT}{2F}\right] \ln\left[\frac{S_{H_2O}P_{H_2O} + I}{S_{H_2O}P_{H_2O}}\right] \tag{18}$$

where

$$R_1 = R_o + R_{air} + R_{hydrogen} \tag{19}$$

so that one now has only one non-linear term, the water overpotential.

Consider, now, the data for our first operating five-cell stack, presented in the previous Final Report of our initial contract.[1] After 2 hours of operation the DC current-voltage characteristic for the stack was experimentally determined (approximately two dozen data points were taken). In addition, interrupted-current measurements were taken to

determine the ohmic resistance of the stack, R_o. A least squares fit of Equation (18) to the data was carried out with the results shown in Fig. 5.46. It is seen that by the proper choice of parameters V_o, R_1, and S_{H_2O}, a good fit of the V-I characteristic was achieved. In addition, the value of R_1 required, 1.55 ohms, was just slightly larger than the experimentally determined value of ohmic resistance, R_o, which was 1.46 ohms. This is consistent with relatively-small air and hydrogen overpotentials (small values for R_{air} and $R_{hydrogen}$) which were postulated earlier.

It is interesting at this point to estimate from the theory what the voltage losses were in our experimental stack for a load current of 1000 mA:

Open circuit voltage	5.13 volts
Ohmic loss	-1.46
Air + hydrogen polarization	-0.09
Water polarization	-0.75
Output voltage	2.83 volts

One should remember that the principal reason for the large water polarization is the small water content (3%) of the fuel. For fuels with higher water content, both the open circuit voltage and the water polarization will be significantly smaller. Nevertheless, an understanding of water polarization is essential for interpreting cell behavior and may be useful as a tool in cell testing.

5.3.2.1 Diagnostic Technique Suggested by The Theory

A standard diagnostic technique employed in fuel cell work is the current interruption method[12] which enables one to determine the total overpotential, η, from both electrodes.* To determine the separate

*More precisely, it enables one to determine the total overpotential due to slow electrochemical processes, such as concentration polarization.

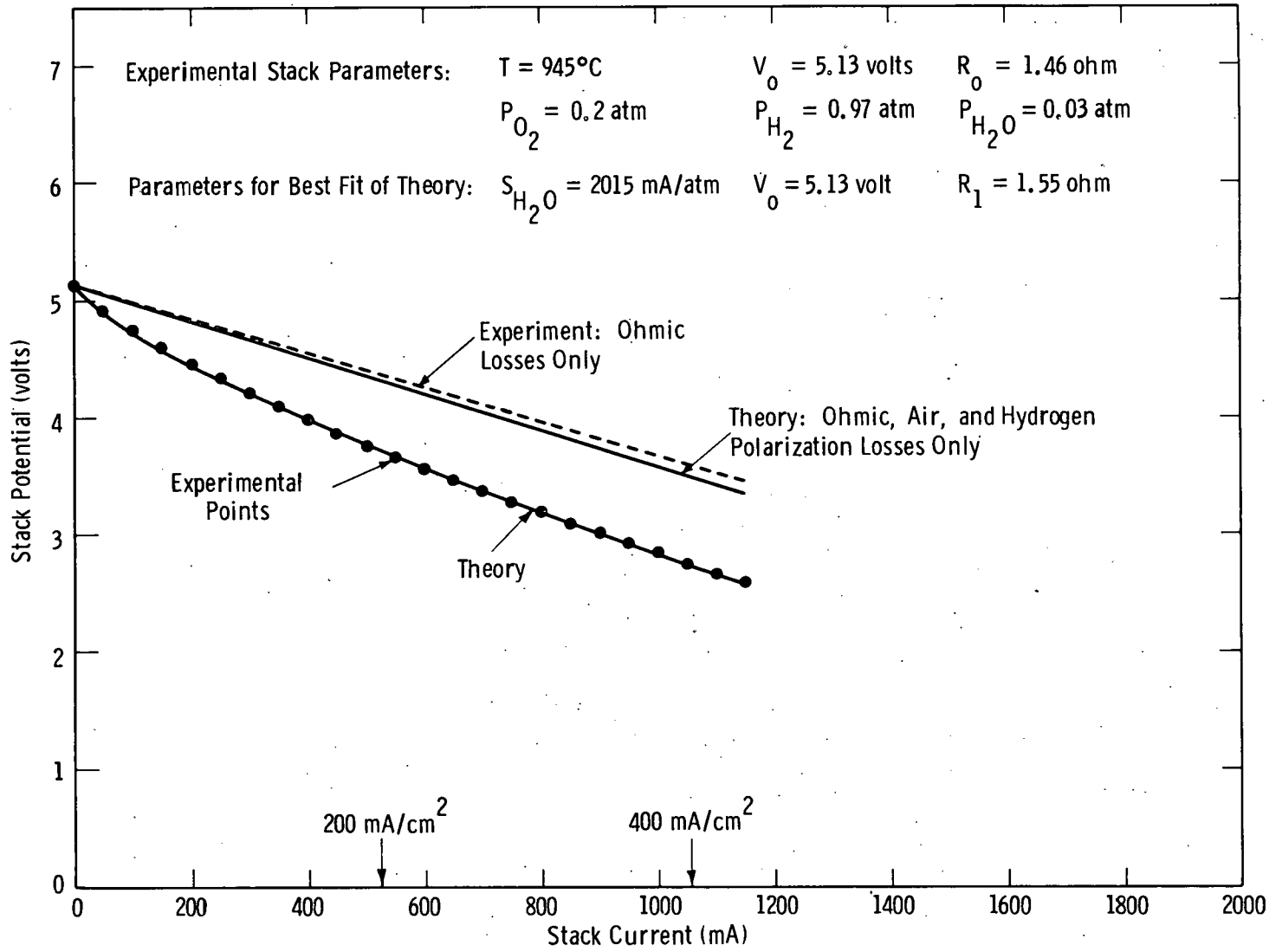

Fig. 5.46 — Comparison of experiment (points, dashed line) and theory (solid lines) for the current-voltage characteristic of a stack with hydrogen-water fuel. The lower theoretical curve includes the water polarization loss discussed in the text.

fuel and air electrode contributions, η_{fuel} and η_{air}, requires a suitable reference electrode. For a single thin film cell this is difficult; for a multi-cell stack it becomes experimentally impractical.

One promising application of the theory is in a technique for determining the overpotential components η_{air}, $\eta_{hydrogen}$, η_{water} for single or multi-cell units with no additional electrodes. According to Equations (12), (13), and (14), each overpotential component depends on a different fuel or air component partial pressure, provided the current is held constant. Therefore, measurement of the total overpotential at constant current for two (or more) values of a fuel or air component partial pressure should enable one to determine the corresponding overpotential and its pore conductance coefficient, S.

Suppose, for example, that one fixes the current at I and measures two values* of P_{O_2}; then, according to Equations (8) and (16)

$$\Delta\eta = \Delta\eta_{air} \simeq \left[\frac{RTI}{4FS_{O_2}}\right] \Delta\,(1/P_{O_2}) \tag{20}$$

so that the air overpotential is

$$\eta_{air} \simeq \frac{1}{P_{O_2}} \frac{\Delta\eta}{\Delta(1/P_{O_2})} \tag{21}$$

and the pore coefficient is

$$S_{O_2} \simeq \left[\frac{RTI}{4F}\right] \frac{\Delta(1/P_{O_2})}{\Delta\eta} \tag{22}$$

The partial pressure may be changed by substituting an inert gas having a similar diffusion coefficient. For example, to determine

---

*Note that the changes in P_{O_2} may be large provided one does not approach low pressures where $P_{O_2} \sim I/S_{O_2}$; in that case, one would have to use the exact non-linear Equation (12) instead of the approximate linear Equation (16).

η_{air}, one might employ 20% O_2 + 80% N_2 and 40% O_2 + 60% N_2 as the mixtures; for determining $\eta_{hydrogen}$ one might use 97% H_2 + 3% H_2O and 48% H_2 + 49% He + 3% H_2O; and for η_{water} one could use 10% H_2O + 90% H_2 and 5% H_2O + 5% N_2 + 90% H_2. In each case only one active fuel or air component should be varied.

An interesting alternative to the use of interrupted current measurements for obtaining the change in total overpotential, $\Delta\eta$, is now related. From Equation (2) one has

$$\Delta\eta = \Delta V_o - \Delta V \tag{23}$$

Therefore if one measures both the change in open circuit potential, ΔV_o, and the change in cell potential, ΔV, under constant current corresponding to a change in the partial pressure of a fuel or air component, then $\Delta\eta$ is obtained entirely by DC measurements.

Other diagnostic techniques based on the theory are possible and may be discussed in future reports. First, however, the theory should be tested by obtaining the complete V-I characteristic for a cell, measured for several different fuel and air compositions.

5.3.3 Effect of Inter-Cell Electrical Leakage on The Open Circuit Potential

The Previous Annual Report[1] described that, during the preparation of the fuel electrode, nickel oxide can diffuse into the stabilized zirconia of the porous support tube and increase its electronic conductivity. This would provide a current leakage path between adjacent cells and, consequently, reduce the open circuit potential below the theoretical value.

To determine whether these effects actually occurred, a section of porous support tube containing only fuel electrodes was tested. The

specimen was placed in a hydrogen-water atmosphere and the leakage resistances (through the support tube) between two sets of adjacent fuel electrodes were measured over a temperature range of 400 to 1000°C. A wide range of applied potentials were employed (20 to 1000 mV) but the resistances measured were independent of the potential, and were nearly identical for the two sets of electrodes. A plot of this resistance as a function of temperature is presented in Fig. 5.47. Activation energies for the conduction process were high, about 1.2 to 1.8 eV, and of the magnitude expected for electronic conduction in these oxides. At 1000°C the leakage resistance was about 45 ohms.

The effect of a leakage resistance of this magnitude on a cell comparable to those of the experimental five cell stack can be estimated. One would expect the open circuit potential, V_o, to be approximately 27 mV lower than the theoretical value, E_o. From the actual stack data one finds that V_o was about 38 mV lower than E_o. Considering the uncertainties in the electrode gap spacings and the diffusion of the nickel oxide which produced the leakage resistance, it is felt that this was reasonable agreement.

One concludes (1) that the fuel electrode preparation treatment introduces a moderate amount of electronic conductivity into the zirconia of the porous support tube, and (2) this provides a current leakage path between adjacent cells which results in a 3 to 4% reduction of the open circuit potential below the theoretical value.

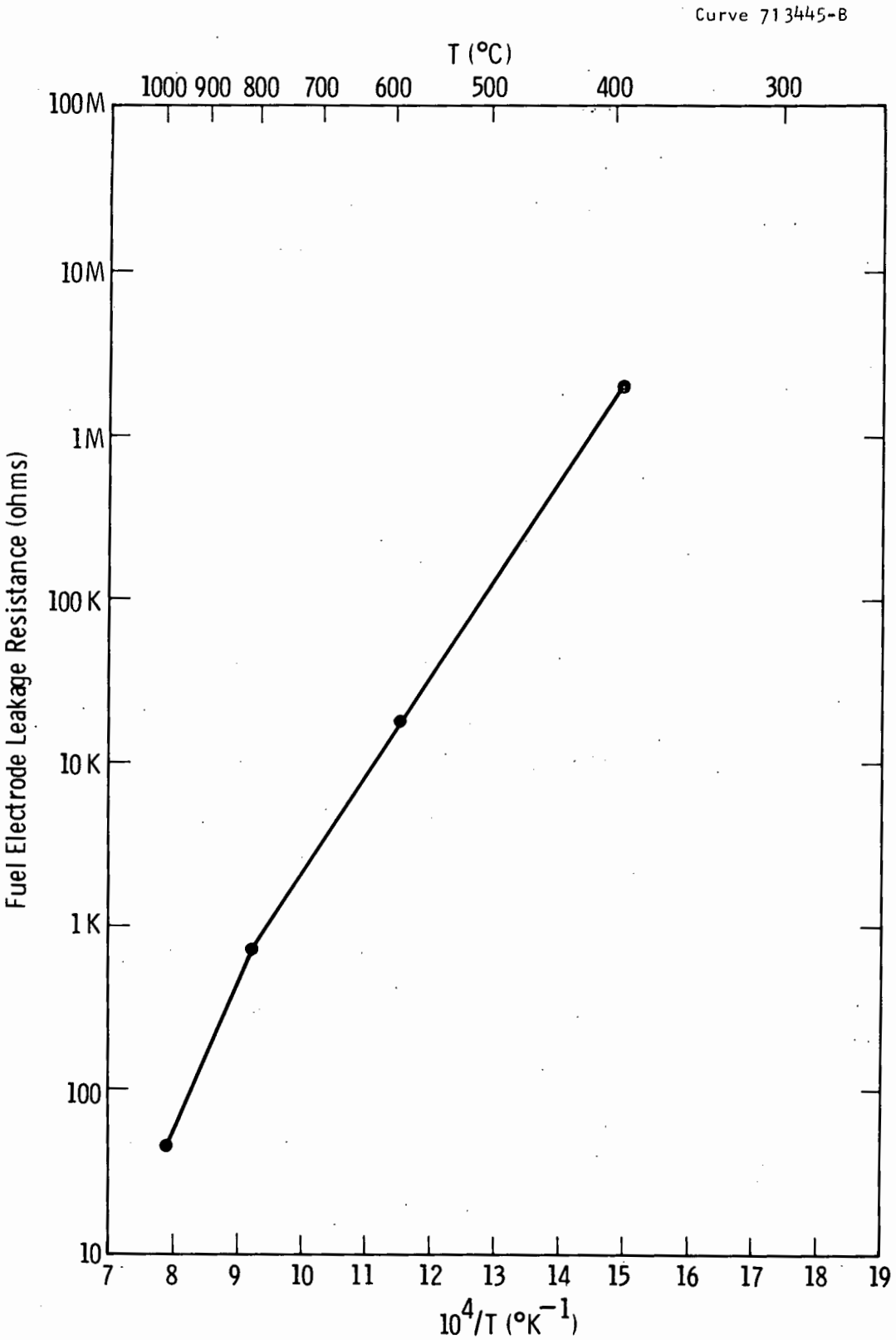

Fig. 5.47 — Leakage resistance between adjacent nickel fuel electrodes vs temperature. A hydrogen-water atmosphere was used

5.3.4 Subtask A. Power Output

Power output evaluation is awaiting the construction of fuel cell stacks with suitable electrical resistances, which should be achieved by reducing the interconnection, air electrode and the interconnection/air electrode interfacial resistance.

5.3.5 Subtask B. Effect of Air and Fuel Condition

Work on this subtask is, necessarily, delayed, pending the fabrication of suitable 20 cell stacks in which air and fuel conditions can be varied and the results obtained and analyzed.

6.0 FUTURE WORK

The following work plans are projected for the fifth quarter of the continuation contract, conforming to the projected task-time schedule of the present program, as outlined in the Contract Management Plan.

6.1 TASK 1. DEVELOPMENT AND REFINEMENT OF FABRICATION PROCESSES

The goal of this task is to develop reliable techniques of component fabrication that will lead to reproducible stack performance.

6.1.1 Subtask A. Interconnection Fabrication by Electrochemical Vapor Deposition

Uniform IC films are now produced over 0.3 m long tube lengths. The task of alumina-doping of lanthanum chromite can now be resumed, to attain more precise IC compositions. These doping attempts will not interfere with continuous processing of stacks for testing, which will be a parallel effort. Tubes with interconnection material deposited by RF sputtering will also be prepared and used for small (2-5) cell stack assemblies. Here, precise interconnection compositions should be attained and evaluated.

6.1.2 Subtask B. Fuel Electrode Stack Process

A faster sinter process has allowed an increase in nickel content to 60 v/o in the fuel electrode (40 v/o ZrO_2). The fuel electrode process has been refined for 20 cell stacks and further improvement is not necessary at this time. These features will be incorporated in fuel electrodes fabricated in future 20 cell stack test samples.

6.1.3 Subtask C. Air Electrode Stack Process

The aim here is to improve the air (oxygen) permeability through the air electrode current collector structure, toward attaining an optimum porosity/conductivity ratio in 20 cell stack lengths. Air electrodes of indium oxide and alternate electrode materials, $Ca_{1-x}La_xMnO_3$ in particular, will be bonded together and to the interconnection, by heating the air electrode oxide powder with admixtures of a lower melting oxides.

6.1.4 Subtask D. Porous Support Tube

Process refinement of extruded porous, calcia-stabilized zirconia $[(ZrO_2)_{.85}(CaO)_{.15}]$ tubes of 0.3 m length will continue with emphasis on techniques that will improve uniformity of porosity and shrinkage over the entire tube length of 0.3 m. A new furnace that was designed and constructed in the last quarter is being used and will be further modified, if necessary, to fire uniform tubes of desired physical properties.

6.1.5 Subtask E. Cell Stack

The aim of this subtask is to produce a reference 10 watt stack. Findings of Subtasks A through D are being used toward that objective.

6.2 TASK 2. LIFE TESTING OF CELL COMPONENTS AND STACK

The goal of this task is life prediction of cell stacks, using state-of-the-art components and material. The five-station test system is completely operational.

6.2.1 Subtask A. Interconnection Testing in a Dual Atmosphere

Dual atmosphere tests of the fuel electrode-interconnection-air electrode combination will be tried on actual, fabricated specimens, as they become available. The multi-surface electrode technique, mentioned in this report, will be employed.

6.2.2 Subtask B. Fuel Electrode-Interconnection Interaction

The testing of the fuel electrode-interconnection combination specimen resistance will continue. The effect on electrical resistance of various hydrogen-water atmospheres will be examined, since this might be a sensitive test for interface resistance, arising from a composition variation of IC material adjacent to the fuel electrode.

6.2.3 Subtask C. Air Electrode-Interconnection Interaction

As fuel cell stacks are prepared and tested, the performance will be related, in part to an evaluation of polarization behavior of the air electrode and interconnection, and an indication, if any, of abnormal interfacial resistance will be explored, to determine its cause and to eliminate, or reduce, its effect.

6.2.4 Subtask D. Single Cell Life Test

In addition to the single cell life test, required for milestone ▽2▽ , an additional single cell will be examined for its response to wide variations in the fuel and air mixtures. Results will be compared with predictions of the V-I characteristic theory, discussed in Section 5.3.1 of this report. Response to time-varying load currents (step-function, ramp-function, sinusoidal) may also be investigated.

6.2.5 Subtask E. Small Stack Life Test

Fabrication of 20 cell fuel cell stack assemblies will continue. Evaluation of small stacks for performance characteristics, toward attaining milestone ▽3▽ , will be performed on the life test apparatus. Also, interconnections prepared by RF sputtering will be evaluated here, if they can be successfully incorporated into finished cell stacks, to serve as a comparison test in which the precise IC composition will be incorporated (by RF sputtering) into the fuel cell makeup.

6.3 Task 3. Stack Performance Evaluation

For this task, a minimum of five and, possibly, as many as ten stacks will be tested under many conceivable conditions to which they might be exposed in the operation of an envisioned power plant.

6.3.1 Subtask A. Power Output

Cell stacks will be tested with respect to power output at varying cell efficiencies. Polarization contributions of each stack component will be assessed, as they relate to overall stack performance.

6.3.2 Subtask B. The Effect of Fuel and Air Conditions

The performance of the stack, using rich and lean coal-gas fuels, in combination with oxygen-rich and -lean air, will be established. Tests, ranging from 5% fuel-containing gas mixtures to 5% O_2-containing air, will provide guidelines for predicting maximum attainable current densities under such conditions. Initial work in this area, on H_2/3% H_2O fuel, will begin the fifth quarter.

6.4 TASK 4. REPRODUCIBILITY OF 10 WATT STACKS

This task is aimed at demonstrating the reproducibility of the state-of-the-art techniques with respect to materials, their fabrication, and stack performance. The goal of this task is to raise the confidence level of the technology. Toward this objective, a number of fuel cell stacks of 20 cells each will be fabricated. The stacks will be tested with simulated coal gas and will be expected to deliver about 10 watts of power output each (Milestone 4).

6.4.1 Subtask A. Stack Comparison Testing

Reproducibility of properties and compositions of the fuel cell components will initiate the work in this area in the fifth quarter. Later in the program the stacks will be compared with respect to uniformity of cell performance and total stack output, under similar operating conditions.

8.0 REFERENCES

1. Final Report, Task E-4, C-1197-9, Thin Film Battery/Fuel Cell Power Generating System, DOE Contract EY-76-C-03-1197, March 31,1978.
2. Kellogg, H. H., Trans. Met. Soc. AIME, 236, 602-15 (1966).
3. Anderson, H. V., Murphy, R., and Humphrey, K., in "The Rare Earths in Modern Science and Technology," Editor, Gregory J. McCarthy and J. J. Rhyne, Plenum Press, New York (1978).
4. Rohr, F. J., Proceedings of the Workshop on High-temperature Solid Oxide Fuel Cells, Brookhaven National Laboratory, May 5-6, 1977.
5. Baukal, W., et.al., Journal of Power Sources, 1(1976/77)2 Elsevier Sequoia S.A. Lausanne.
6. Reference 1, Subtask D.
7. Groth, R., Phys. Stat. Sol., 14, 69 (1966).
8. Anderson, H., personal communication.
9. O'Keefe, M. and Morse, W. J., J. Phys. Chem., 65, 1438 (1961).
10. Dewit, J.H.W., J. Solid State Chem., 8, 142, (1973); 13, 192 (1975).
11. Etsell, T. H., and Flengas, S. N., J. Electrochem. Soc., 118, 1890 (1971).
12. Sverdrup, E. F., et. al., "Hydrocarbon Fuel Cell Technology," Academic Press Inc., New York, 1965, p. 311.

8.0 APPENDIX A

PAST PROGRAM SUMMARY

Highlights of progress on the past contract program (DOE EY-76-C-03-1197), conducted during April 1, 1976 - March 31, 1978, are presented for the various tasks and subtasks, as specified in detail in the Design Plan of that program.

A.1 TASK 1. MATERIALS IDENTIFICATION AND SELECTION

A.1.1 Subtasks A and B. Interconnection Search and Identification

Work on the interconnection material identified a modified rare earth chromite as a very promising interconnection material. Specifically, modified lanthanum chromite, exemplified by the composition $La_{.95}Mg_{.05}Cr_{.75}Al_{.25}O_3$, was selected from among several systems studied, as having the most suitable properties for a cell interconnection material. No other oxide system investigated with comparable conductivity could be modified to produce the good thermal expansion match, low volatility, and negligible chemical interaction with other cell components that are available with this material.

As a result, this system received special effort in the second year of the program, to optimize its properties and to establish fabrication procedures for obtaining thin layer interconnection films. Films were successfully produced by electrochemical vapor deposition, initially onto fuel electrode substrates, and then as part of the fuel cell stack fabrication.

Additional work in this area was aimed at minimizing ionic transfer of oxygen ions through the interconnection layer, during cell operation.

A.1.2 Subtask C. Development of Other Stack Components

Selection of the other stack components was fixed during the first year of effort and further work on them was primarily aimed at refining their fabrication into useful thin films. These materials are:

- support tube -- porous, calcia-stabilized zirconia (15 mol % calcia)
- fuel electrode -- nickel cermet (nickel deposited in a porous, stabilized zirconia skeleton)
- solid electrolyte -- yttria-stabilized zirconia (from 8 to 12 mole % yttria)
- composite oxide air electrode -- tin-doped indium oxide (1 to 5 wt % SnO_2) current collector, with praesodymium oxide impregnation of the zirconia skeleton.

A.2 TASK 2. FABRICATION TECHNIQUES

Techniques for producing films of the various active components proceeded to the level where they were used to produce fuel cells and fuel cell stacks. Concurrently, an extrusion process was developed to produce, in-house, the porous support tubes.

4.2.1 Subtask A. Interconnection

RF sputtering was used to produce films for basic property evaluations, whereas an electrochemical vapor deposition (EVD) technique was developed that produced modified rare earth chromite compositions that are both leak-tight and conducting, as thin films ($\sim$40 μm). This EVD technique was subsequently used in fabricating the fuel cell stack that was tested on the program.

A.2.2 Subtask B. Electrolyte

The solid electrolyte, yttria-stabilized zirconia, was readily-prepared as a thin film by the EVD process. This process was reconfirmed on this program and was used to produce solid electrolyte films for the combination testing of components and fuel cell stacks.

A.2.3 Subtask C. Air and Fuel Electrode

Coating of zirconia support tubes with fuel electrode slurry compositions, along with firing and subsequent nickel reduction in hydrogen, was reconfirmed as a viable process for producing the nickel-cermet, porous fuel electrode. This process was used in the preparation of the fuel cell stacks.

The CVD process was developed to a sufficient level to enable preparation of uniform films of tin-doped indium oxide, air electrode current collector. This process was used in the preparation of the fuel cell stack that was tested in this program.

A.2.4 Subtask D. Porous Support Tube

Extrudable mixtures, prepared by combining selective size fractions of refractory starting powders and calcining at 1780°C, produced tubes that met the specifications of open porosity (>25 volume percent), tensile strength (>5000 psi) and thermal expansion ($\sim$10 x 10^{-6} m/m°C at 1000°C). Surface pores of the tubes were 10-11 μm in diameter with some variation in pore sizes, caused by agglomerates of water swelling starch plasticizers, used in the batch material preparation for extrusion.

A.3 TASK 3. COMPONENT TESTING

Equipment was built and used to test the fuel cell components and the fuel cell stack evaluated in this program.

A.3.1 Subtask A. Interconnection

Testing of interconnection films for composition and properties was ongoing throughout the program for gas tightness, resistivity, thermal expansion, doping level and oxygen vacancy concentration.

A.3.2 Subtask B. Combinations

A crossed-electrode testing concept and specimen was evolved and equipment was assembled, to enable combinations of fuel cell components to be tested in various atmospheres.

A.3.3 Subtask C. Useful Life Testing

A 5 cell fuel cell stack was fabricated and evaluated on the program. Three series connected cells of this stack met the program goals -- displaying 80% voltage efficiency at 200 mA/cm^2 for 700 hours with less than 10 percent voltage degradation at 950° to 980°C in a hydrogen - 3% water vapor fuel atmosphere.

A.4 TASK 4. ALTERNATE ELECTROLYTES AND BATTERY DESIGNS

Work scheduled in this area involved:

1) keeping abreast of developments in the field, with regard to alternate electrolytes, and evaluating, in an initial manner, any that show promise to the Westinghouse thin film fuel cell.
2) modifying cell and cell stack design, if the test results indicated problems, particularly, with respect to mechanical over-stressing of cell or cell stack component(s).

No alternate useful electrolytes were developed in the solid electrolyte field during the 2 years of the completed program. Test data on the fuel cell stack was so favorable that no major design changes have been contemplated.

9.0 APPENDIX B

OPERATION, DESIGN CONCEPT AND SOME APPLICATIONS OF THE HIGH TEMPERATURE, SOLID OXIDE ELECTROLYTE FUEL CELL

B.1 INTRODUCTION

Fuel cells are electrochemical generators of direct current electricity. Unlike conventional generators, based on heat cycles, they have no Carnot efficiency limitations, and can, theoretically, yield high energy efficiencies. Of all fuel-cell power systems, that system, based on a stabilized-zirconia solid electrolyte, offers the highest achievable efficiency. A battery design study, conducted prior to this program, indicated that power densities of 23 kW/ft^2 of fuel cell module could be achievable with the state-of-the-art materials and fabrication processes defined at that time, when the stacks would be operated at 80% electrical efficiency. The high-temperature solid oxide electrolyte (HTSOE) fuel cell would operate at 1000°C, without the need of expensive catalysts, on a carbon monoxide-hydrogen gas mixture, provided by the gasification of coal. The fuel generator would operate at 1000°C for several reasons: a) the resistivity of the solid electrolyte is sufficiently low at this temperature to permit high levels of electrical efficiency at high current densities, and b) the heat released in the fuel oxidation could be efficiently transferred, in one concept, to the endothermic coal gasification reaction. The simplified coal gasification reaction is

$$C_{(g)} + CO_{2(g)} \rightarrow 2\ CO_{(g)}$$

This reaction is endothermic, i.e., heat is absorbed by the reaction as written.

Therefore, the by-product heat emanating from the high-temperature, solid oxide fuel cell generator, could be used for the coal gasification reaction. At ∿900°C (and above) this reaction proceeds toward 100% CO formation.

Actually, since the exhaust gas contains a small amount of water vapor, carried over from the coal, the gasification reaction produces a fuel mixture of CO and H_2O which then constitutes the fuel mixture for the fuel cell generator. Since abundant coal is the basic fuel, an economically competitive power plant, based on this fuel-cell type, would contribute to natural-resource conservation.

In another concept, clean pipeline coal gas could be supplied to the high-temperature, solid oxide electrolyte fuel cell and the by product, hot exhaust gas (CO_2) from the fuel cell generator would be used to produce steam in an off-gas, waste heat boiler. This steam would then be used to support either an industrial process, adjoining the fuel cell site, or for additional power generation, via a steam turbine, or both, to enhance the overall system efficiency.

Apart from the efficiency advantage and the use of a non-critical fuel, the HTSOE fuel cell is attractive from other standpoints.

- Air pollution from the fuel cell power system would be minimal. (Carbon dioxide and water vapor are the only species emitted.)
- Since the heat rejected by the fuel cell would be employed to gasify coal or produce steam, thermal pollution of the environment, due to waste heat, would be minimized.
- The fuel cell generating process would not require cooling water, consequently, siting of plants would not be dependent on plentiful water supplies.

The commercial feasibility of this new power system greatly depends on the useful life of the generator. At the onset of this continuation program, the useful life of the thin-film fuel cell stack

had achieved ~700 hours at temperature, but with the promise of much longer life indicated by the stable nature and makeup the individual component layers of the fuel cell itself. The ERDA-directed, NASA-managed, Energy Conversion Alternatives Study, conducted in 1975-76 at the Westinghouse Research Laboratories, indicated that, for fuel-cell power systems to be competitive from an electricity-cost standpoint, the useful life of the fuel cell module must exceed 30,000 hours.

B.2 TECHNICAL BACKGROUND

Solid electrolyte fuel cells generate electrical energy from fuel and air. In this section a fuel cell power system is described, including: (1) how solid-electrolyte cells produce electrical energy, (2) how individual cells can be combined to form high-performance batteries, and (3) how batteries can be combined with auxiliary equipment into several plant concepts. Also reviewed are the major technical problems that must be resolved to allow demonstration of a long-lived, high-performance fuel-cell battery.

B.2.1 How Solid Electrolyte Fuel Cells Generate Electricity

As shown in Fig. B.1, a solid electrolyte fuel cell consists of four basic components: an air electrode, a solid electrolyte, a fuel electrode, and a porous support tube. A fifth component, the interconnection between adjacent cells, is not shown.

The porous tube of stabilized zirconia, which serves as a mechanical support for the fuel cell, has an approximate wall thickness of 1000 μm. In contrast, the individual component layers lie in the thickness range of 20 to 50 μm.

Exposed to the air flow is the air electrode. One kind is a composition of oxides, such as $(In_2O_3)_{0.98}(SnO_2)_{0.02}$ current collector, fabricated in a porous structure that is readily permeated by oxygen from air which flows over it. Here, praesodymium oxide is discontinuously deposited onto a porous zirconia matrix that underlies the current

6442A92

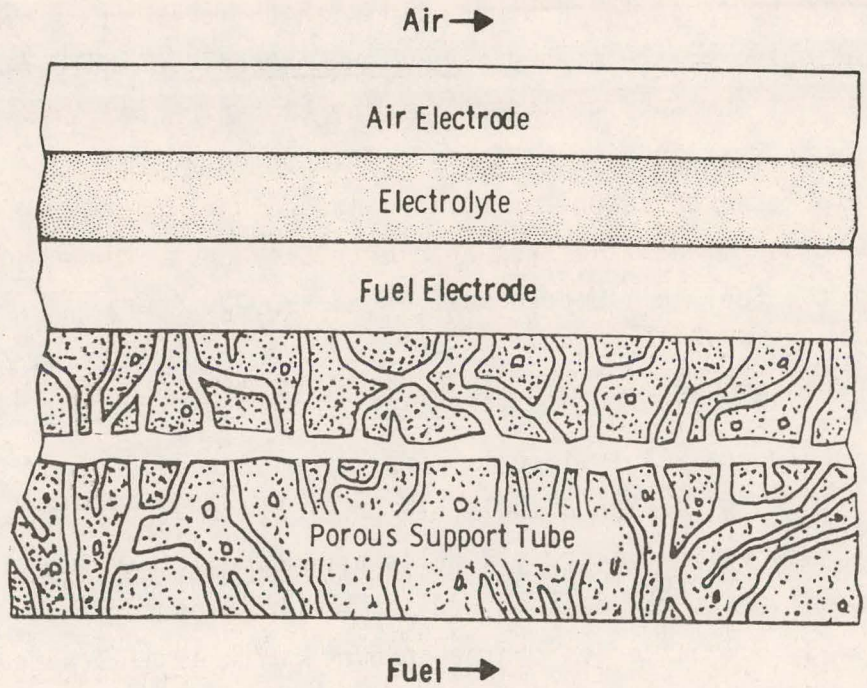

Fig. B.1 Schematic Cross-Section of a Thin-Film Fuel Cell

collector and represents the active part of the air electrode. This active PrO_2 effects the necessary $O_{2(g)}$ to $2O^{=}$ transition. Oxygen molecules from the air accept electrons at active PrO_2 sites, leaving the electrode positively charged, and forming oxygen ions, $O^{=}$, as shown in Fig. B.2. Each O_2 molecule removes four electrons and forms two $O^{=}$ ions, as the cell operates

Oxygen ions can enter the second component of the cell, a dense zirconia ceramic, such as yttria-stabilized zirconia. This is the solid electrolyte of the cell. At the operating temperature of 1000°C, oxygen ions pass through this layer, due to the oxygen concentration gradient across the ceramic. (If an $O^{=}$ enters at the air electrode-electrolyte interface, an $O^{=}$ emerges at the electrolyte-fuel electrode interface, thus preserving the electrical neutrality of the material.) The gases on either side of the cell will not penetrate through this impervious

Dwg. 6442A93

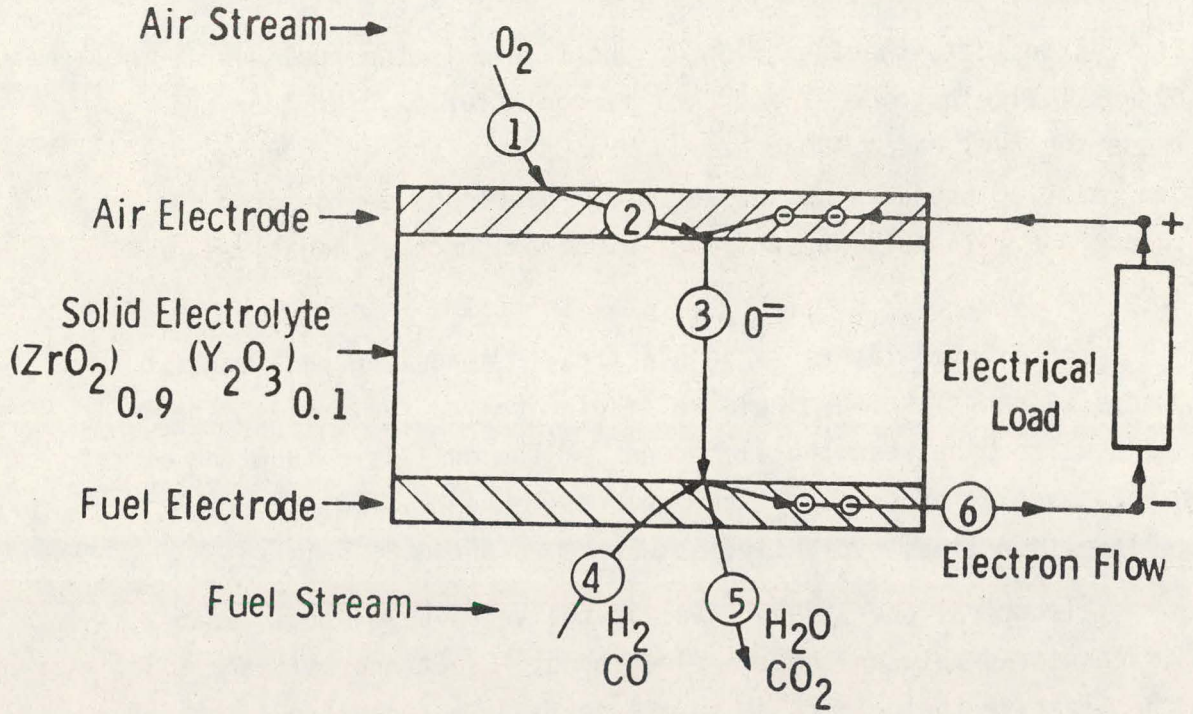

1 Oxygen molecule diffuses through air to electrode
2 Oxygen atom picks up two electrons from air electrode to form oxygen ion in electrolyte
3 $O^=$ oxygen ion transport through electrolyte
4 Fuel diffuses to reaction site and reacts with $O^=$ ion releasing electrons to fuel electrode
5 Reaction product leaves reaction site
6 Electrons from fuel electrode flow through external load to air electrode

Fig. B.2 Schematic Diagram of a Solid Electrolyte Fuel Cell, Indicating How Oxidation of the Fuel Generates Electric Current to the External Load

electrolyte layer, so that the reaction can only take place when current is drawn from the cell stack. Since the ceramic electrolyte has no electronic conductivity, no electrical short circuit can occur in the cell.

Exposed to the fuel flow in the figure is the fuel electrode. The porous fuel electrode is a nickel-zirconia cermet. At the fuel electrode the fuel gases, CO and/or H_2 react with the emerging $O^=$ ions to form reaction products CO_2 and/or H_2O. Electrons emerge from the fuel electrode. In this way the fuel electrode becomes negatively charged.

These three layers -- an electrolyte sandwiched between two electrodes -- constitute a single solid-electrolyte fuel cell. The voltage developed between the electrodes of the cell is a function of the oxygen partial pressure in the fuel gas. When current is drawn, the cell voltage lies, typically, between 0.95 and 0.65 volt.

Electrical energy and power is delivered by the cell when a load is connected between the two electrodes. Electrons will then flow from the negative fuel electrode to the positive air electrode through the load circuit. Current can be drawn from a cell, as long as air and fuel gases are supplied and the combustion products removed. Current densities of 300 mA/cm^2 have been obtained from solid-electrolyte cells, while still maintaining cell efficiency at 80 percent. The output voltage produced at such currents is a function of the ohmic losses and concentration polarization losses in the electrodes.

B.2.2 Fabrication of Fuel-Cell Stacks

To obtain the voltages required for a practical system, cells must be connected in series. The technique, illustrated in Fig. B.3, provides a potentially low-cost method of making a series-connected stack of cells. This modular stack design is aimed at minimizing ohmic losses at relatively high current densities. It is necessary to provide an electrolyte surface area of approximately 5 ft^2/Kw, based upon state-of-the-art single cell performance.

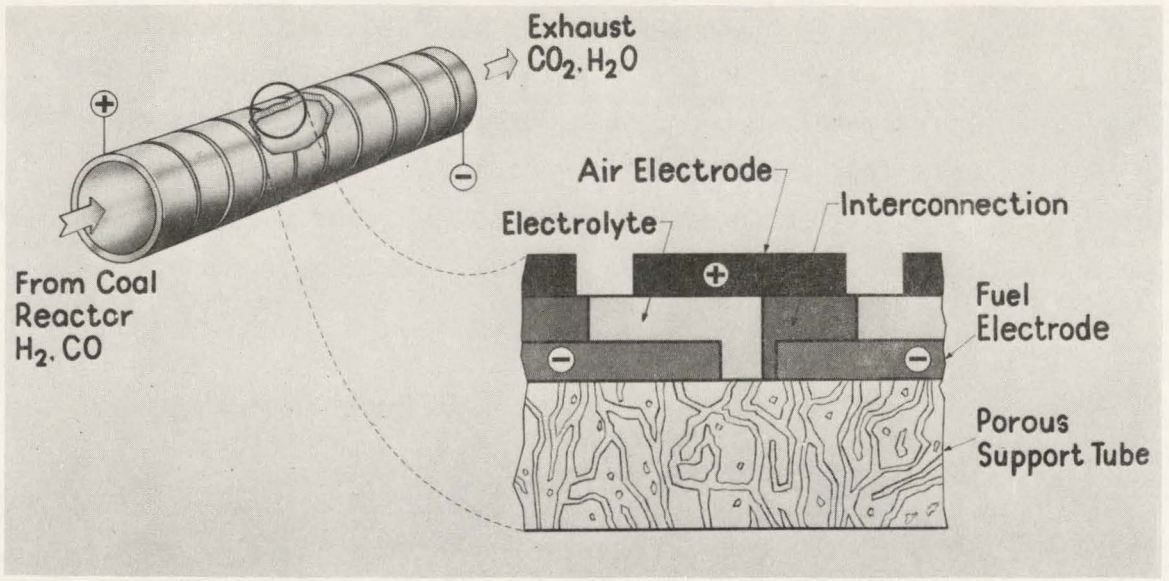

Fig. B.3 Cross-Section of the Westinghouse Thin Film, High-Temperature, Solid Electrolyte Fuel-Cell Stack

A group of cells, each about 0.5 cm wide around a porous tube of about 1.3 cm O.D., are series-connected to form a stack. As schematically shown in the cross-section of Fig. B.3, all cells on the tube are series-connected by joining the air electrode of one cell to the fuel electrode of an adjoining cell, through an electronically conducting interconnection. The interconnection must be fabricated as a gas-tight film, just as in the case of the electrolyte. Particular attention must be paid to the junction between the electrolyte and interconnection films to ensure gas impermeability in this region as well.

As indicated in the figure, a solid-electrolyte fuel cell stack consists of five components: an air electrode, a solid-electrolyte, a fuel electrode, and a cell interconnection, all approximately 50 μm, and a porous support tube with an approximate wall thickness of 1000 μm.

A design study at Westinghouse indicated that, in order to maximize the power generated per unit length of battery, the unit cell length must be approximately 0.5 cm. Fig. B.4 shows that the unit cell length is the sum of four characteristic lengths: ℓ_c, the active cell length; ℓ_i, the active interconnection length; and ℓ_a and ℓ_f, the gap lengths between adjacent air electrodes and fuel electrodes, respectively.

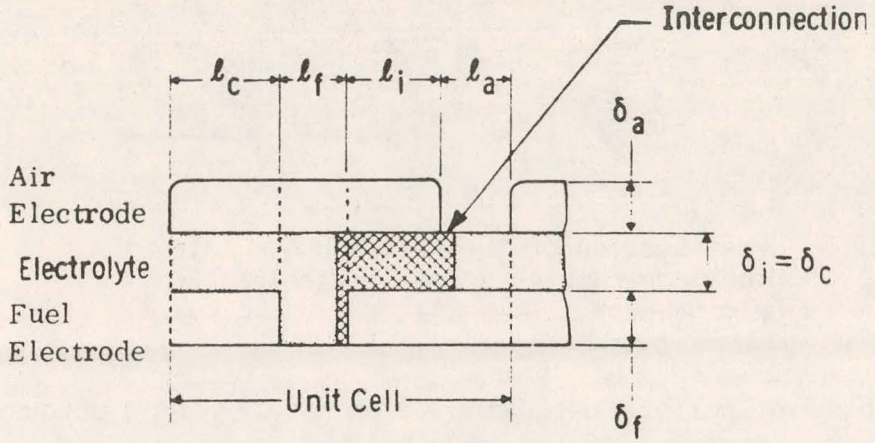

Fig. B.4 Schematic of a Unit Cell Design in the Thin-Film Fuel Cell

The optimum active-cell and active-interconnection lengths, for the achievement of maximum power output, have been found to be dependent on the values of: (a) the resistivity and thickness products of the electrolyte and interconnection; (b) the resistivity to thickness ratios of air and fuel electrodes; and (c) the gap lengths, ℓ_a and ℓ_f. Precise fabrication processes, which will result in component films of the desired length and thickness in the appropriate location on the substrate, are, therefore, considered to be necessary for the fabrication of high-performance batteries.

B.2.3 High Temperature, Coal-Burning Fuel Cell Power Generating System

In a coal-burning fuel-cell, central station power system, one possible application of the HTSOE fuel cell, means must be provided to:

- produce CO and H_2 fuel gas mixture from the coal,
- clean and circulate the fuel gas mixture to the fuel cells,
- transfer heat generated in the operation of the fuel cells either to the endothermic coal gasification reaction or to producing steam which can be used in an industrial process or in a steam turbine to produce electricity.

To produce a practical energy system, individual cells must be assembled in such a way as to generate large voltages and sizable quantities of power.

Therefore, coal-burning, solid-electrolyte fuel cell system would include a coal gasifier, gas cleaning and circulating equipment, a fuel cell generator, a heat exchanger and a DC and AC inverter. Coal or coal char is fed to the coal gasifier, along with a portion of the hot CO_2 and H_2O combustion products and waste heat from the fuel cell generator (Fig. B.5). Here, coal reacts with the combustion products to form a CO and H_2 fuel gas mixture. These gases are fed to the fuel cell generator, after treatment to remove particulate material and sulfur compounds. In the generator, the fuel gases are electrochemically oxidized to CO_2 and H_2O.

The fuel cell generator would operate at $\sim$1000°C for the following reasons: (a) the resistivity of the solid electrolyte is sufficiently low ($\sim$20 Ω cm) to permit high levels of electrical efficiency at high current densities, (b) the heat released in the fuel oxidation can be efficiently transferred to the endothermic coal gasification reaction.

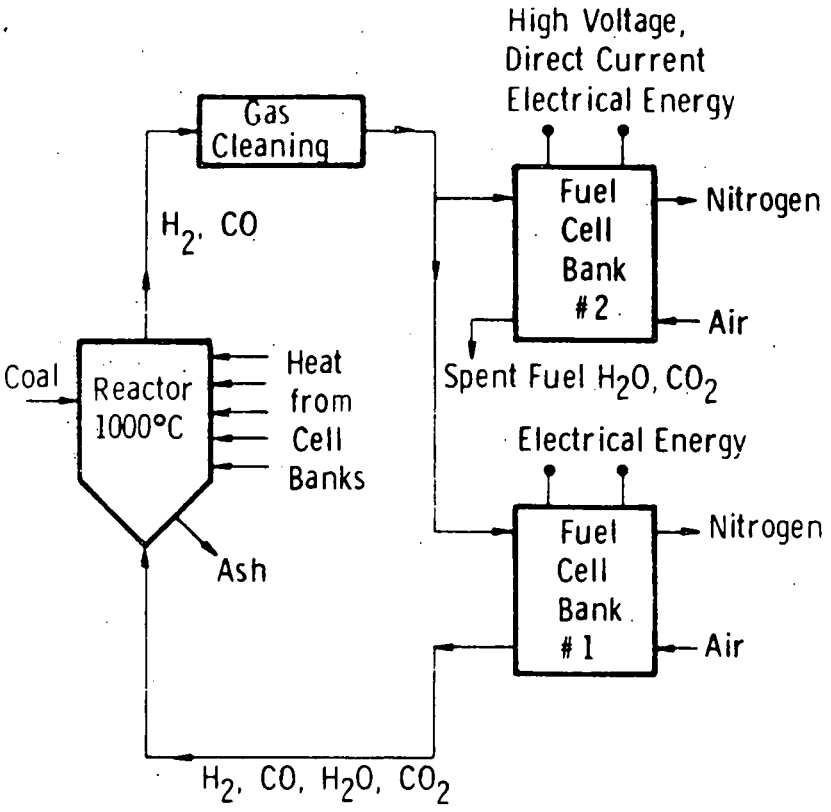

Fig. B.5 Coal Burning Solid-Electrolyte Fuel Cell Power Generating System

A battery design study has indicated that power densities of 7 kW/ft^3 of fuel cell module are achievable with state-of-the-art materials and fabrication processes, when the stacks are operated at 80 percent electrical efficiency.

The air necessary for the operation of the generator is brought in separately. The N_2 of the air and the unreacted O_2 emerge from the generator, exchange heat with the incoming air, and exhaust to the surroundings. Suitable AC power is available to tie into a utility grid network. Here, 500 MWe, and greater, would be the size of a central station generating plant.

B.2.3.1 The Fuel Cell-Heat Exchanger System

Figure B.6 indicates the components of a possible HTSOE fuel cell generator-heat exchanger system. Here the fuel cell generator would be composed of a high-temperature heat exchanger component that is integrated with the cell stacks (as in Fig. B.5). The system would allow the final heating of fuel and air in a ceramic heat exchanger to the operating temperature of the cell stacks. Ceramic heat exchangers are necessary because of the unavailability of metallic alloys that are stable at 1000°C for extended periods of time.

B.2.4 High-Temperature, Industrial Co-Generation Systems

Another potential application for the HTSOE fuel cell, previously cited, would be in an industrial cogeneration plant. Such a plant would have an output of ∿50 MWe and would be capable of delivering steam from an off-gas, waste heat boiler to an industrial process, or for power generation (by a steam turbine), or both.

B.2.5 Fuel Cell Industrial Cogeneration

For the cogeneration scheme the fuel cell auxiliary systems components and their flow diagram interrelationships are given in Fig. B.7. The coal gas supply system (not shown) would deliver clean, pipeline coal gas to the cogeneration system. Salient features of this system would include the following.

1. Coal gas would arrive from some central gasification facility, would be distributed to the industrial site at an intermediate Btu value, and would be delivered at 1 bar, with no more than 100 ppmv H_2S, with provision for additional desulfurization, if needed.
2. Products of combustion from this gas would contain less than 0.1 lb. $SO_2/10^6$ Btu to meet any SO_2 control level now in existence, or proposed.

Dwg. 7690A02

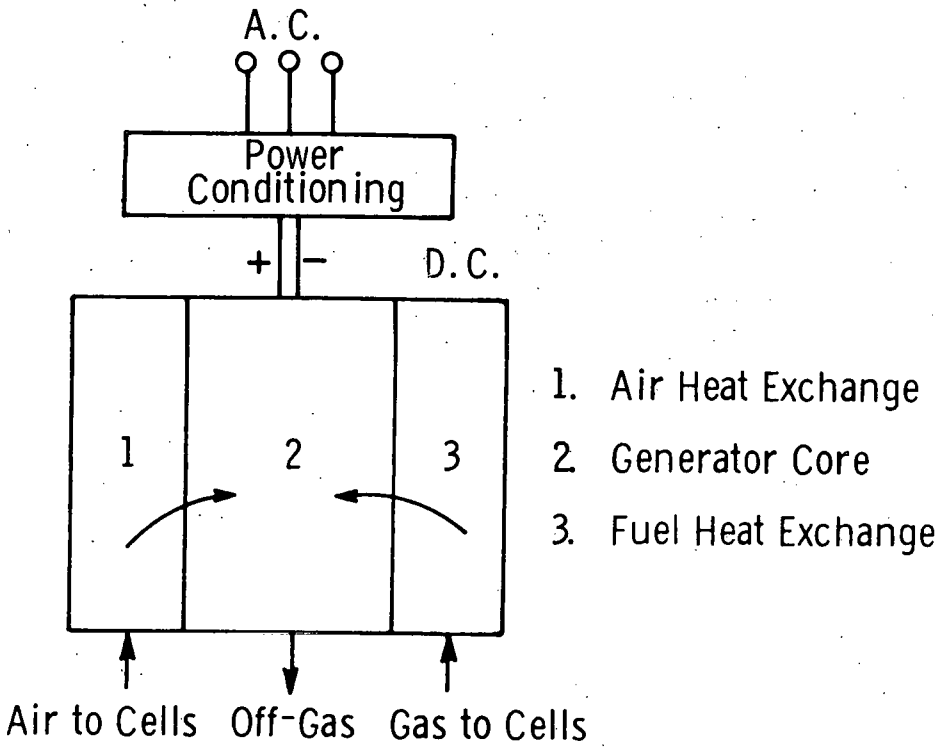

FIG. B-6 — Heat exchange — generator — power conditioning scheme

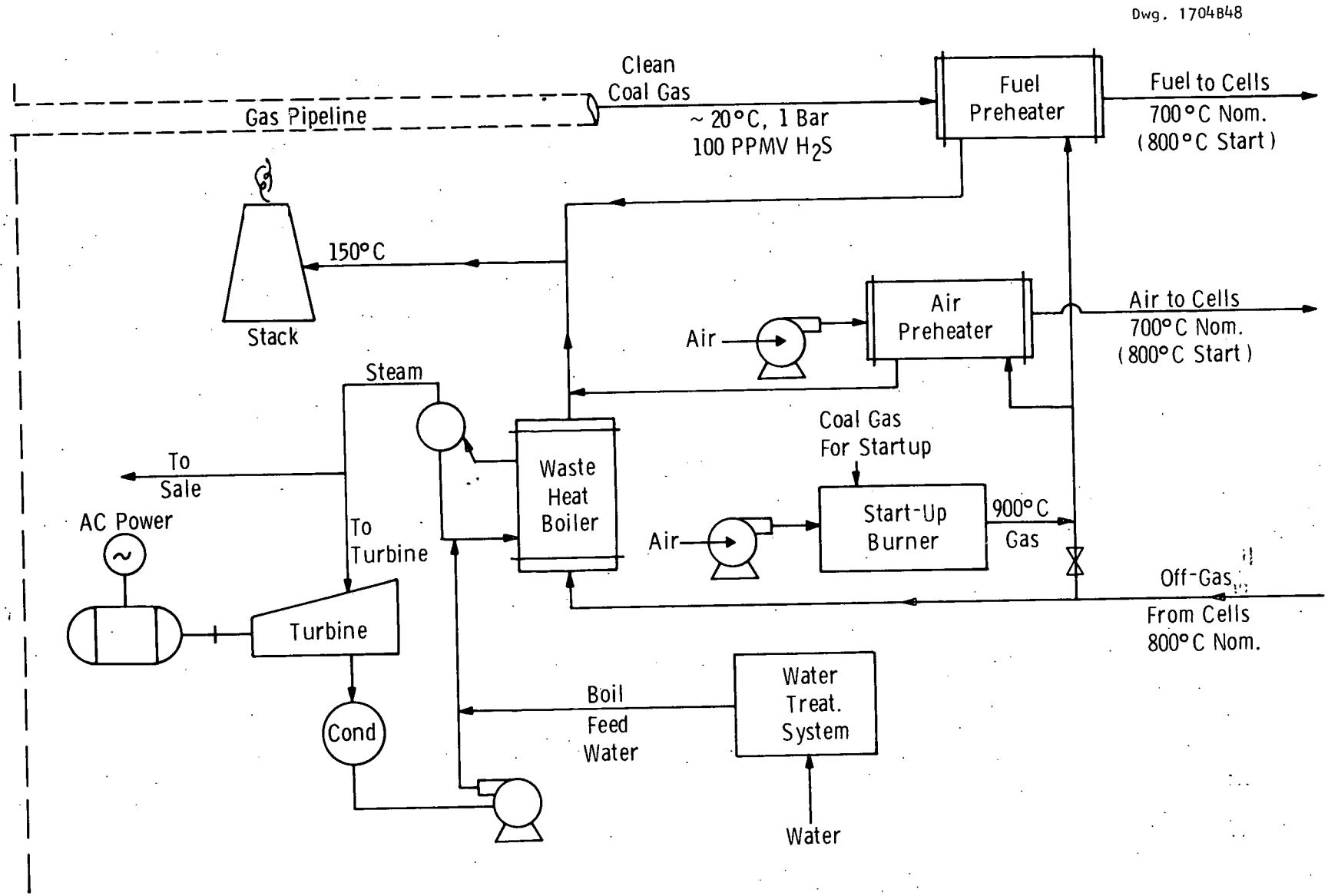

FIG. B-7 — HTSOE fuel cell auxiliary systems

3. Fuel and air preheaters would use 800°C gas from the fuel cell outlet combustors.
4. Start-up heat would be supplied at 900°C for a limited period of time, to provide start-up fuel and air at 800°C to the fuel cells. These conditions represent the maximum temperatures that would be achieved in the heat exchanger (only during the last few hours of cell start-up heating).
5. Preheater materials and design would consider the presence of H_2S in the fuel gas to avoid carbon deposition from a reverse Boudouard reaction.
6. Steam from the off-gas waste heat boiler would be used by an industrial process, adjacent to the fuel cell site, or for power generation, or both.

10.0 APPENDIX C

TOLERANCE OF THE FUEL ELECTRODE TO SULFUR

Nickel or cobalt fuel electrodes in the high temperature solid state fuel cell will sulfidize at sufficiently high partial pressures of sulfur-containing gases. The concentration at which this damaging reaction will occur depends on some operating parameters of the fuel cell, in particular temperature, fuel composition, no-load voltage, and electrode polarization. The effect of the first three can be estimated from thermodynamic calculations. Earlier calculations of this type at Westinghouse are revised and extended here to include more recent data on the Ni/NiS_x phase boundary, to cover a broader range of fuel composition, and to examine the effect of operating at different temperatures. These parameters all have an important bearing on requirements for the engineering design of the fuel cell and the fuel pretreatment and purification system.

Nickel is being used as the fuel electrode in current work in preference to cobalt because it is a cheaper metal and can operate in leaner fuel mixtures without oxidation. However, cobalt will tolerate higher sulfur content of the fuel gases.

The basic results of the calculations are that a greater tolerance for sulfur-containing gas in the fuel is shown at (1) high temperatures, (2) higher hydrogen/water, as compared to carbon monoxide/carbon dioxide content of the fuel, and (3) at no load fuel cell voltages, either greater or less than a region near 0.7-0.75 volt. Figures C1, C2, C3, C4, C5, C6 illustrate this behavior.

Figure C1 shows the effect of the no-load fuel cell voltage on the sulfur concentration in the fuel at which the nickel electrode will just begin to sulfidize (i.e., the concentration of total sulfur-containing

Curve 712838-A

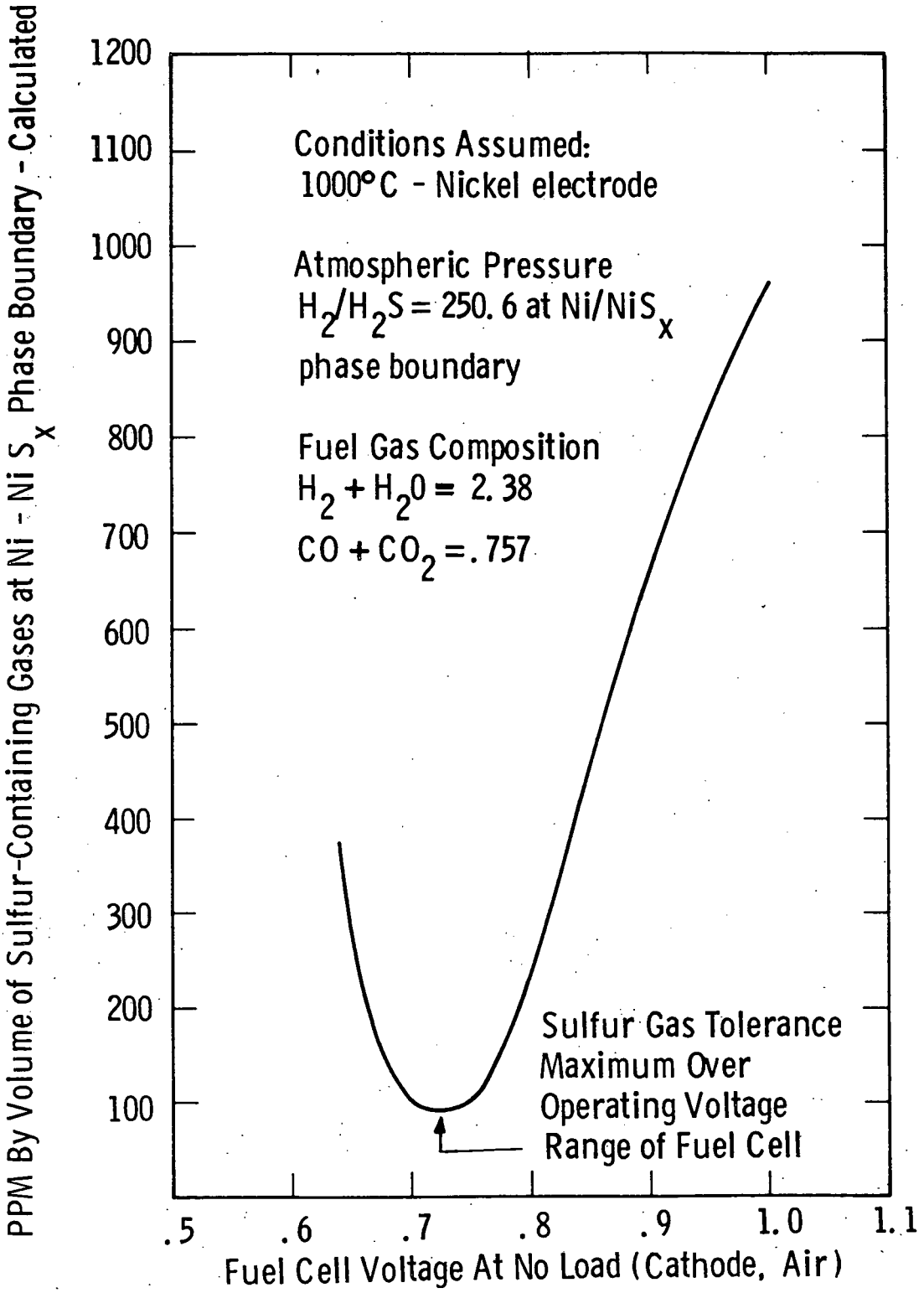

Fig. C.1— Concentration of sulfur-containing gases at which a nickel fuel electrode begins to form $Ni\ S_x$ vs fuel cell voltage at 1000°C

Curve 712835-A

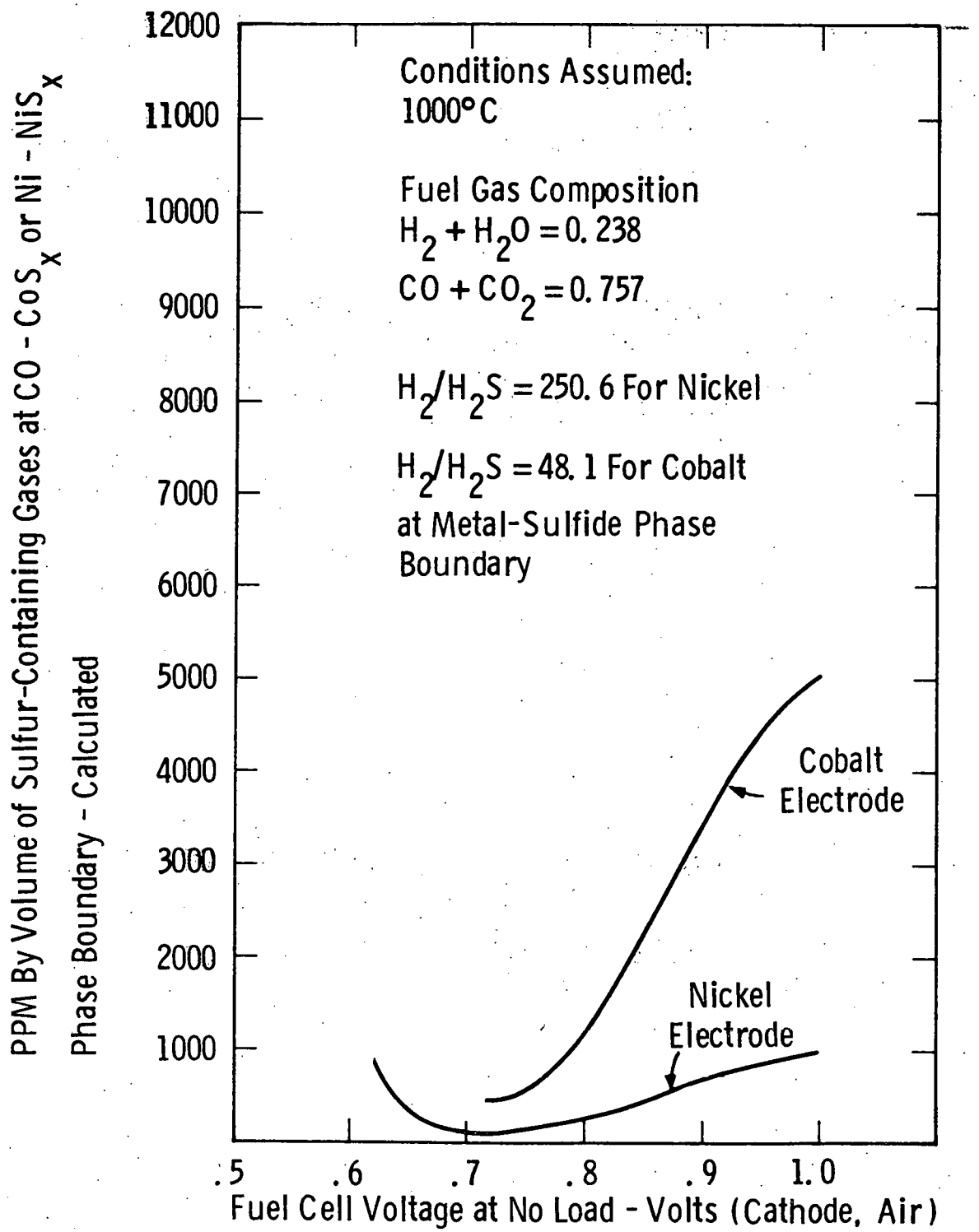

Fig.C.2— Concentration of sulfur-containing gases at which the fuel electrode will begin to sulfide vs the fuel cell voltage

Curve 712836-A

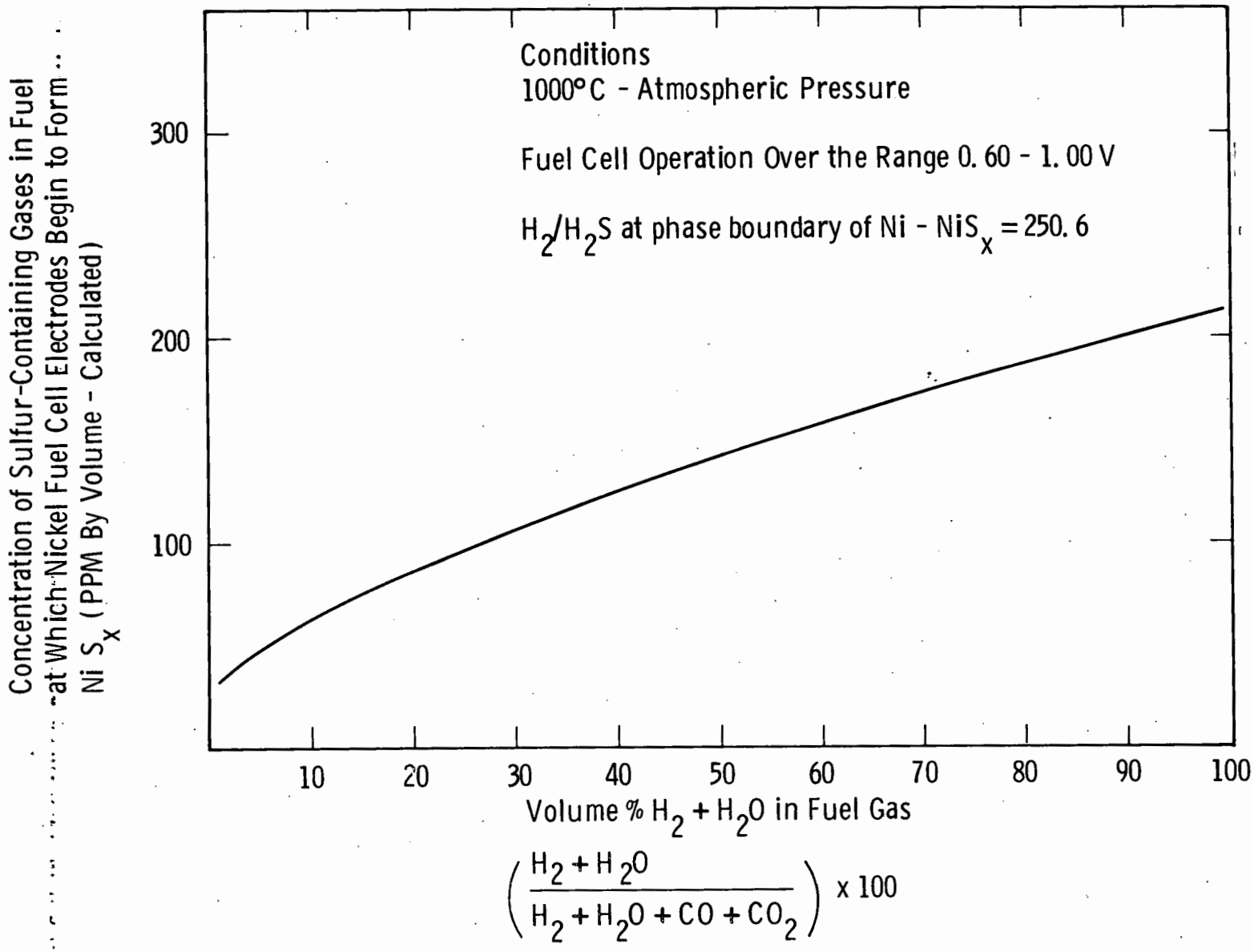

Fig. C.3— Tolerance of nickel electrodes to sulfidation as a function of fuel gas composition

Curve 712834-A

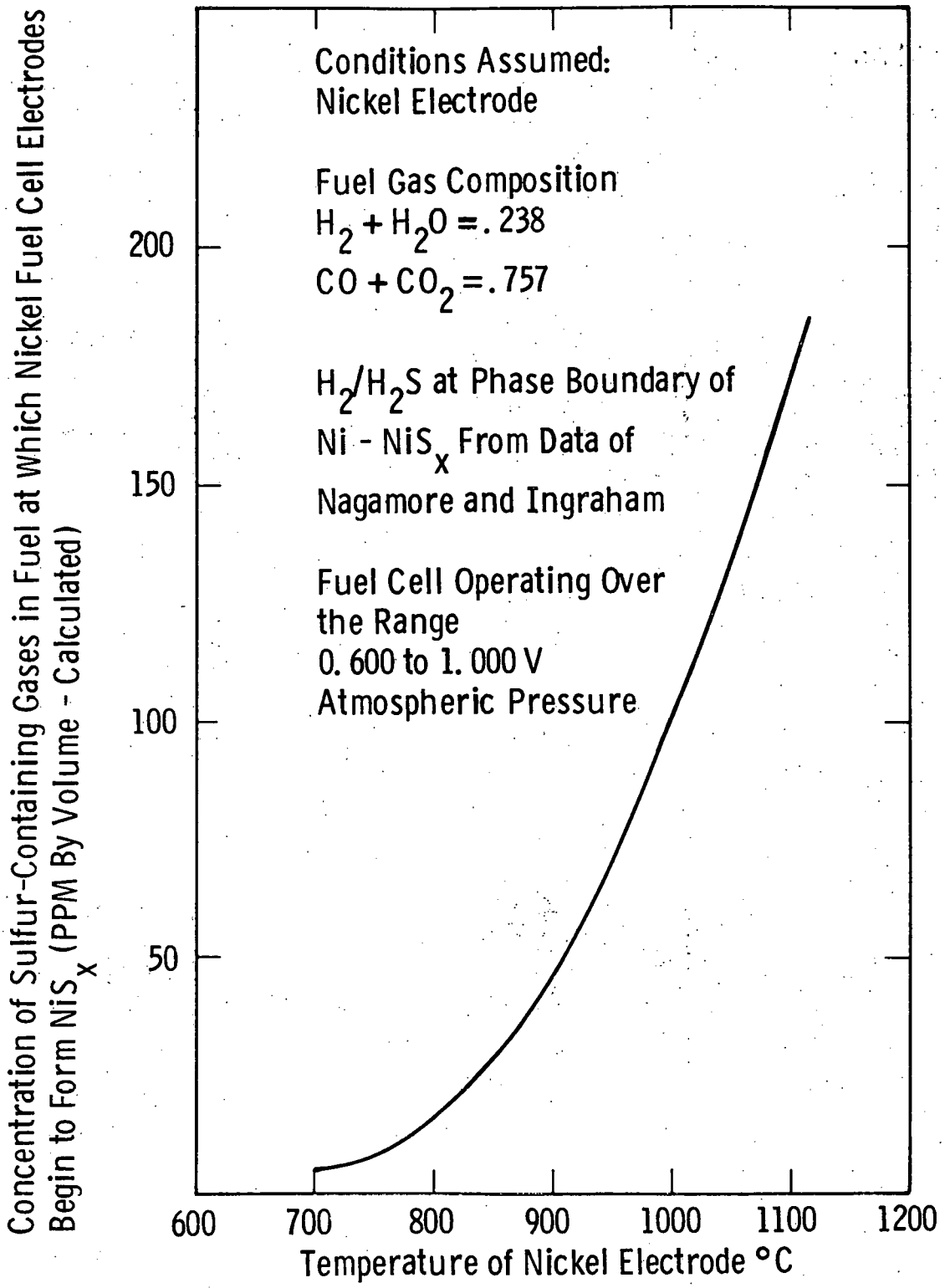

Fig. C.4—Tolerance of nickel electrodes to sulfidation as a function of temperature

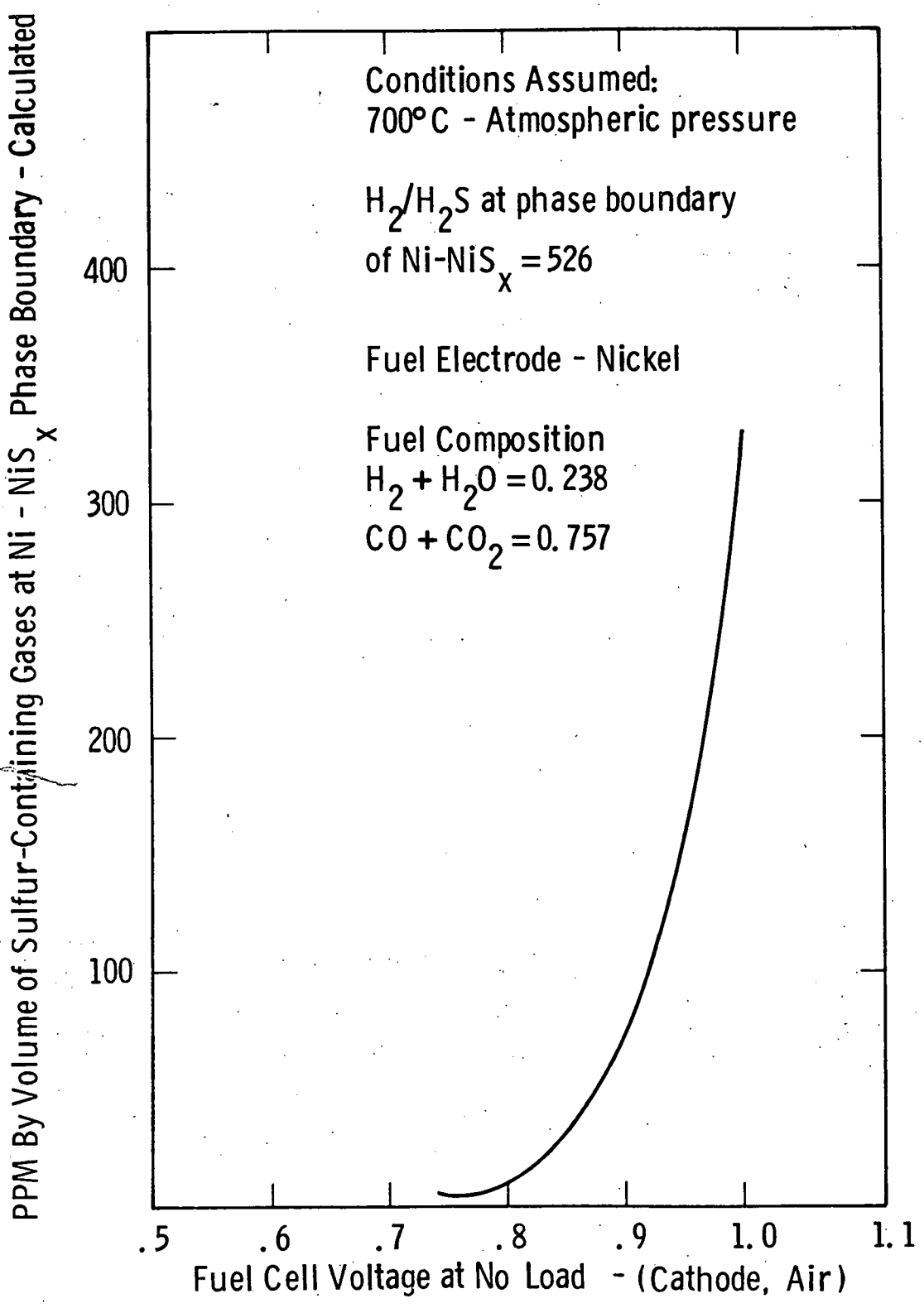

Fig. C. 5— Concentration of sulfur-containing gases at which a nickel fuel electrode begins to form NiS_x vs fuel cell voltage at 700°C

Curve 712833-A

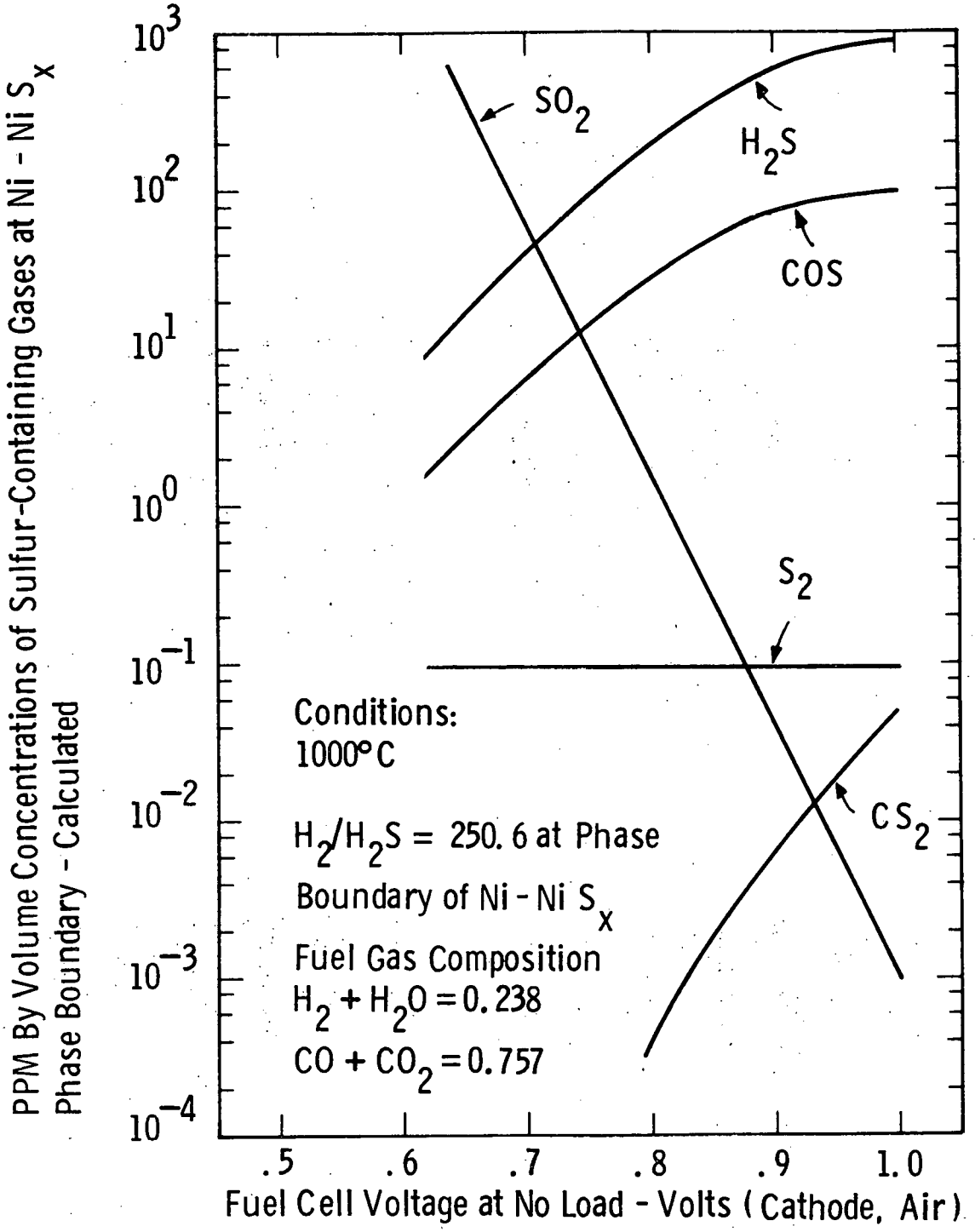

Fig. C.6— Concentrations of sulfur-containing gases at Ni - Ni S_x phase boundary vs fuel cell voltage - calculated

gases in equilibrium with both nickel and nickel sulfide at the phase change boundary). These data are for 1000°C, which is near the highest operating temperature of the present fuel cell and for an arbitrary chosen fuel composition. A minimum in the curve, of about 90 ppm of sulfur-containing gases, is seen between about 0.70-0.75 volts. For normal operation of between about 0.6 and 1.0 volts then, this is the critical region where the least tolerance for sulfur content in the fuel gas occurs. If we allow for a 30% safety factor, these data suggest that 60 ppm or less would be a useful operating level for sulfur-gas content under these conditions. To increase this tolerance it would be necessary to operate at higher temperatures or higher hydrogen/water contents, as will be illustrated in the subsequent discussion.

Figure C2 compares cobalt to nickel for the same operating parameters. It is seen that cobalt has more than five times the sulfur tolerance of nickel at the minimum point of the curve, which would make it particularly useful, where high sulfur content of the fuel cannot be avoided, and at lower temperatures, where the sulfur tolerance of the fuel electrode is drastically reduced.

Figure C3 shows the effect of changing the volume per cent of H_2/H_2O in a hypothetical fuel gas containing only H_2O, H_2, CO and CO_2. It is seen that the tolerance minimum for fuel cell operation varies by about a factor of seven for the entire composition range, with the H_2/H_2O rich fuels having a greater sulfur tolerance than the corresponding CO/CO_2-rich fuels.

Figure C4 illustrates the effect of temperature on the minimum tolerance of nickel for (total) sulfur-containing gases for the same fuel composition as previously illustrated for nickel at 1000°C (see Figure C1). A drastic reduction from a value of about 170 ppm at the Ni/NiS_x phase boundary at 1100°C to about 5 ppm at 700°C is seen. Thus, if any cell or stack of the fuel cell assembly were to operate at a temperature as low as 700°C, the fuel feed to the whole fuel cell system

would require a very low sulfur content. This suggests strongly that the operating temperature be kept high to reduce potential problems of electrode damage by sulfidation and the cost of removing sulfur from the fuel gas.

Figure C5 illustrates specifically the sulfur tolerance at 700°C for a system analogous to that previously illustrated (Figure C1) for nickel at 1000°C. (700°C is probably the minimum temperature at which we could usefully consider operating the present solid state zirconia-electrolyte fuel cell.) The minimum is seen not only to have shifted to a much lower ppm value, but also to have broadened and shifted to a somewhat higher voltage. For example, at 0.8 volt the value for the Ni/NiS_x boundary is about 8 ppm, only 3 ppm above the minimum. Thus, even raising our voltage operating range to 0.8-1.0 volt would not help much if we chose this relatively low operating temperature for any of the stacks or cells.

Finally, we show in Figure C6 the relative importance of the major gaseous sulfur-containing species in the fuel for the same conditions as illustrated for nickel (see Figure C1) at 1000°C. It is seen that CS_2 and S_2 are relatively unimportant over the entire voltage range of the fuel cell. H_2S followed by COS are the important species at the higher voltages (e.g., 0.8 volt and above) while SO_2 is the most important sulfur-containing gas species below 0.7 volt.

The data shown here illustrate the general magnitude of sulfur-containing gas concentrations which can cause sulfidation of the fuel electrode over varying operating parameters of the fuel cell stack. The general results are summarized* as follows:

1) Nickel or cobalt fuel electrodes should show a minimum tolerance for sulfur-containing gases at a fuel cell (no load) voltage between 0.7-0.75 volts depending on the temperature.
2) Fuel gases higher in H_2/H_2O as compared to CO/CO_2 show a higher sulfur gas tolerance.

*These data consider only possible sulfidation effects and not chemisorption on the electrode surface.

3) Fuel electrodes (nickel or cobalt) show a much higher sulfur gas tolerance at 1000°C as compared with 700°C.
4) Cobalt electrodes show a considerably higher sulfur gas tolerance than nickel electrodes.
5) The major sulfur gas species in a fuel gas of the fuel cell are expected, thermodynamically, to be SO_2 at voltages below 0.7 volt and H_2S and, to a lesser extent, COS at voltages above 0.8 volt (no load voltage).
6) As a typical example, for a fuel gas composition $H_2 + H_2O$ = 25 volume % and $CO + CO_2$ = 75 volume %, sulfidation of nickel will occur at about 90 ppm total sulfur-containing gas at atmospheric pressure and 1000°C and at about 5 ppm at 700°C at the minimum tolerance, which occurs in the no load fuel cell voltage range of about 0.7-0.8 volt.

11.0 PERMANENT RECORD BOOK ENTRIES

Figuring Books, containing information described in this report are:

208043, pp 93-147, 103-127
208371, pp 1-156
207773, pp 51-94
204414, pp 32-34, 36-66, 67-102
208337, pp 1-182
207917, pp 15, 23, 24-36, 3-114
207905, pp 131-147
208777, pp 1-30
208023, pp 3-114

12.0 ACKNOWLEDGEMENTS

The following personnel made important contributions to results contained in this report:

Dr. R. W. Liebermann - Preparation and operation of the computer program used to make the thermodynamic calculations of reactions of nickel and cobalt with sulfur-containing gases.

Dr. B. Lancaster - Sulfur tolerance estimation.

D. F. Bradley - EVD fabrication, life test setup.

J. J. Duffala - Porous support tube development.

G. M. Halgas - Porous support tube development.

C. W. Hughes - SEM and EDAX analyses.

R. C. Kuznicki - X-ray diffraction measurements.

R. J. McKeever - Density measurements on lanthanum chromite films.

J. N. Robinson - Fuel electrode development.

M. G. Stratis - Oxygen loss measurements on interconnection oxide films and doped indium oxide.

A. L. Wolfe and G. Gidick - Analytical determination of magnesium and aluminum in lanthanum chromite interconnection films.

G. G. Sweeney - DIMA Analysis of IC layers.